

Computational Spectroscopy of Molecular Dynamics Phenomena in Condensed Phase

Dissertation

zur Erlangung des

Doktorgrades der Naturwissenschaften (Dr. rer. nat.)

der

Naturwissenschaftlichen Fakultät II
Chemie, Physik und Mathematik
der Martin-Luther-Universität
Halle-Wittenberg

vorgelegt

von Frau Svetlana Pylaeva

geb. am 06 Februar 1987 in Syktyvkar, Russland

First Reviewer

Prof. Dr. Daniel Sebastiani
Martin Luther University Halle-Wittenberg
Institute for Physical Chemistry
Von-Dankelmann-Platz 4
06120 Halle (Saale)
Germany

Second Reviewer

Prof. Dr. Michael Vogel
Technische Universität Darmstadt
Institut für Festkörperphysik
Gebäude S2|04 bis S2|07
Hochschulstraße 6-8
64289 Darmstadt
Germany

Day of public defense: 17.06.2019

This dissertation has been created under the supervision of Prof. Dr. Daniel Sebastiani at the Institute for Physical Chemistry of the Martin Luther University Halle-Wittenberg.

I, Svetlana Pylaeva, hereby confirm that this thesis is entirely my own work and has been written without any help of others. Sources, mentioned in the References section, have been used in preparation of the thesis and are cited correctly.

Svetlana Pylaeva

Acknowledgements

I would like to express my deepest gratitude to my scientific supervisor Professor Daniel Sebastiani for his support and motivation of my research, and especially the freedom to conduct exploratory work. I would also like to thank Professor Peter Tolstoy and Dr. Hossam Elgabarty for fruitful discussions and collaboration. Many thanks to my collaborators and members of the Sebastiani research group in Halle.

My very special thanks to my family and friends. My parents and my husband Andrei who supported me through the years as well as through life's peaks and valleys. To my old friends, that I've known for a lifetime, and to my new friends I met during my time in Halle, Leipzig and in KAUST.

Table of Contents

1	Introduction	8
2	Theoretical Framework	11
2.1	Molecular Dynamics Simulations	11
2.2	Force Field MD	12
2.3	<i>Ab initio</i> MD.....	13
2.4	Enhanced Sampling Methods	15
2.5	Computational Spectroscopy.....	17
2.5.1	IR Spectra.....	17
2.5.2	Nuclear Shielding Tensor.....	18
2.5.3	Hyperfine Coupling Tensor.....	19
3	Overview of Published Papers.....	21
3.1	Solvent Driven Proton Tautomerism in Strong Hydrogen Bonds.....	21
3.2	Influence of Fluctuating Solvent-Solute Hydrogen and Halogen Bonds on FHF ⁻ Anion....	22
3.3	Molecular Mechanism of Overhauser Dynamic Nuclear Polarization in Insulating Solids.	24
3.4	Salt Bridge in Aqueous Solution of Simple Salts.....	25
3.5	Conformational Ensemble of Polyglutamine-14 Chain.....	26
4	Conclusions	28
5	References	30
6	Academic Curriculum Vitae.....	34
7	Publications	36

1 Introduction

Molecular dynamics phenomena cover a large span of timescales: from ultrafast electron motions (atto to femtosecond) to very slow conformational changes of large molecules and molecular aggregates (up to milliseconds). For each category in these phenomena, there are specific spectroscopic techniques that are suited for analyzing the underlying structural and dynamic parameters. Different spectroscopic techniques operate not only on different timescales but are also connected to specific molecular properties: for example, Nuclear Magnetic Resonance phenomenon is only observed for the nuclei with non-zero magnetic moment, whereas IR spectroscopy gives information exclusively about vibrations changing electric dipole moment. Spectral parameters often allow solving an inverse problem: to elucidate molecular structure and its dynamic properties from the spectra within a given model. However, this becomes increasingly difficult as system's complexity grows: large systems with multiple, often competing interactions and drastically reduced kinetics which are relevant for bio-physical research. In principle, there is a way to solve the forward problem: namely, calculation of systems' spectra from its geometric parameters and that can be achieved by computational chemistry techniques. Molecular Dynamics (MD) simulations in particular were used in this thesis to obtain atomistic details of systems motions (geometric parameters) and observe their spectroscopic signatures.

For complex disordered systems MD is a method of choice. Those systems lack periodicity and regularity and are challenging to address by majority of spectroscopic techniques. Interactions that define structure and properties of such systems are usually non-covalent ones.^{1,2} Hydrogen bonding³ plays major role in structure and properties of liquid water, as well as many biomolecules. Different arrangements of hydrogen bonds and their fluxional nature cause large fluctuations in their spectroscopic parameters. For example, Muraktina *et al.*⁴ demonstrated that a wide distribution of hydrogen bond geometries exists in simple HCl-water mixtures with corresponding ¹H NMR chemical shifts of bridging protons covering a large span of values. These computational results were further analyzed by Limbach *et al.*⁵ and, complemented by data from NMR and neutron scattering experiments, yielding correlations describing OHO H-bonds. A number of other experimental correlations between spectroscopic parameters and geometry of the hydrogen bond in a series of hydrogen-bonded complexes have been proposed⁵⁻¹⁰, with a majority being system specific. Additionally, in a vast amount of such correlations, a wide distribution of structures in solution ("solvatomers"^{11,12}) is averaged out into one data point. Width of the distribution can, in some cases, be estimated from inhomogeneous broadening of spectral lines.^{13,14}

Two projects in this thesis deal with an interesting question: Which specific interactions play a role in the creation of an ensemble of solvatomers? Recently, femtosecond IR pump-probe experiments revealed how ultrafast fluctuations in electrical fields of the fluctuating polar solvent molecules drive proton transfer in the Zundel cation¹⁵. However, other authors have argued that specific solvent-solute interactions play major role in proton transfer in strong OHO⁻ hydrogen bonded complexes.^{16,17} The first and the second projects of the thesis deal with picosecond timescale fluctuations of hydrogen bond geometries in complexes with strong and short hydrogen bonds in aprotic environments. Two strongly hydrogen bonded systems have been investigated: OHN complexes of chloroacetic acid with substituted pyridines in dichloromethane, and FHF⁻ anion in dichloromethane, tetrachloromethane, and vacuum. Combined NMR/IR and MD study in the first project focused on establishing proton transfer mechanism in strong hydrogen bonds. In experiments, proton accepting ability of pyridines was gradually changed to induce proton transfer from acid's side to pyridine's side. MD study, on the

other hand, was able to reveal how proton donating and accepting abilities of the complex were changing due to formation of weak specific interactions with solvent molecules in picosecond regime. Those interactions were further found to cause distribution of spectral parameters of the system. The second project further deepened investigation of solvent-solute interactions and their effects on an extreme case of a very strong symmetric hydrogen bond in FHF⁻ anion¹⁸⁻²⁰. In the anion, bridging proton moves in a very shallow potential¹⁸, and is highly susceptible to any changes in electronic shell of fluorine atoms that arise from multiple specific interactions with solvent molecules. Lone pairs of fluorine atom can participate in hydrogen bonding with protons of the dichloromethane molecules, as well as in halogen bonding with chlorine atoms of dichloromethane or tetrachloromethane molecules. Signatures of interplay of those interactions, and their competition on geometric, kinetic, and spectroscopic properties have been investigated in the project.

In the third project a larger system has been studied: a particular radical has been investigated in its relation to Overhauser effect DNP in insulating solids^{21, 22}. The effect so far has been found operative only for α,γ -bis(diphenylene)- β -phenylallyl (BDPA) radical, and persisted to very low temperatures²³. Moreover, strong dependence of Dynamic Nuclear Polarization on matrix composition has been observed^{21, 22, 24}. Due to the nature of the Overhauser Effect²⁵, hyperfine interaction between protons of the radical and the unpaired electron are to fluctuate with a frequency of the electronic spin transition at a given field: which corresponds to hundreds of gigahertz for current experimental setups. To determine atomistic picture of molecular motions of the BDPA, radical MD simulations were performed in vacuum and in glassy ortoterphenyl matrix. Geometric evolution of the system was then complemented by calculations of spin density evolution in picosecond regime.

The last two projects of the thesis dealt with biologically relevant systems, namely investigation of an Arginine – Aspartic acid anion salt bridge in pure water and in aqueous salt solutions; and study of a Polyglutamine-14 peptide with specific chromophores and solubility tail in water. Salt solutions are known to alter proteins' properties in solution²⁶: “salting in” versus “salting out” effects. On a microscopic level the ions are argued to alter hydrogen bonded network of water²⁷⁻²⁹ making it more rigid – kosmotropic ions; or less rigid – chaotropic ions. When charged amino acid groups are present in the solution they can interact with ions, either unspecifically through water; or specifically when ions bind to amino-acids³⁰⁻³³. Salt bridges are interactions between two charged amino acids.^{34, 35} They are elements of proteins' structural stability and are often found on protein surface exposed to solvent. Interactions of the charged amino acids with free ions in solution and their effects on thermodynamic stability of the salt bridge have been investigated in this project. Second biological system was intrinsically disordered protein Polyglutamine. Intrinsically disordered proteins do not have regular secondary structure in their monomer state, but form amyloid fibrils with regular cross- β sheet structure. Polyglutamine peptides have been investigated extensively due to their relatively simple molecular motif and yet relevance for Huntington disease.³⁶⁻³⁹ Interplay between sidechain-backbone and backbone-backbone hydrogen bonding as well as solvent solute interactions in Polyglutamines have been argued to cause different average structures: collapsed disordered structures⁴⁰ for monomers and even for higher weight molecular aggregates⁴¹; structures with α -helical and β -hairpin motifs for monomers⁴² and small aggregates.^{43, 44} MD simulation of an all atom model of Polyglutamine-14 enclosed with Förster Resonance Energy Transfer chromophores and four amino-acid solubility tail was performed in explicit solvent. Such system setup has allowed for an exploration of the energy landscape of the protein as well as, additionally, to estimate influence of the tail and the chromophores on structural and spectroscopic properties of the system.

This work is based on computer simulations performed in classical and *ab initio* MD framework. In classical MD simulations, the potential energy surface is represented as a sum of analytical interaction terms for all particles. Particles in this case are usually atoms represented as classical point charges. This approach allows performing simulations of large systems with up to a million particles for lengthy time frames: usually ranging from nanoseconds (regime-delete regime?), up to milliseconds. The method was shown to give very accurate results for proteins in particular.⁴⁵ However, in special systems, even more accurate treatment is required with chemical reactions being one of such examples. In classical MD covalent bonds in general cannot be broken during the simulation⁴⁶⁻⁴⁸, *ab initio* MD (AIMD) on the other hand allows tackling chemical reactions as it uses potential generated based on electronic structure theory. AIMD simulations are used for smaller systems containing up to a thousand atoms, and on picosecond timescales. All MD methods allow for direct calculations of thermodynamic and spectroscopic properties of the systems under study, given MD trajectories are ergodic. Ergodicity hypothesis requires that all regions of the potential energy surface are sampled: all potential barriers are crossed and all valleys explored. This requirement is hard to fulfill for large systems with many degrees of freedom, which is why a number of methods to enhance conformational sampling have been proposed⁴⁹. The main idea in many of those methods is to give the system an extra boost to help it cross high potential barriers faster and explore conformational landscape more efficiently. Two of those methods have been used in this thesis: Hamiltonian Replica Exchange MD⁵⁰ and Umbrella sampling MD.

2 Theoretical Framework

2.1 Molecular Dynamics Simulations

Molecular Dynamics simulations constitute a family of computational methods that deal with temporal evolution of a system under a given representation of potential energy surface. Newton's equations of motion are solved and the particles' positions are propagated. Treatment of interactions between the particles is what distinguishes MD methods between each other. Analytical functions are used to describe interactions in large systems, such as proteins, interactions based on electronic structure calculations are usually employed when even more accurate treatment of specific effects is required, for example for chemical reactions. Usually a particle takes part in multiple interactions, all their contributions are summed to yield a force and change particle's position, subsequently. Positions of all the particles of a system in time (time step after time step) constitute MD trajectory.

To solve Newton's equations of motion and propagate system in time, MD integrators are used. So-called leap-frog algorithm uses positions at the time t and velocities at the time $t - \frac{\Delta t}{2}$; the system is then propagated using forces calculated at time t according to the equations for every particle:

$$\mathbf{v}\left(t + \frac{\Delta t}{2}\right) = \mathbf{v}\left(t - \frac{\Delta t}{2}\right) + \frac{\Delta t}{m}\mathbf{f}(t) \quad (1)$$

$$\mathbf{r}(t + \Delta t) = \mathbf{r}(t) + \Delta t\mathbf{v}\left(t + \frac{\Delta t}{2}\right) \quad (2)$$

This algorithm produces the same quality trajectories as velocity Verlet algorithm, whose arguable benefit is that positions and velocities are calculated at the same point of time:

$$\mathbf{v}(t + \Delta t) = \mathbf{v}(t) + \frac{\Delta t}{m}[\mathbf{f}(t) + \mathbf{f}(t + \Delta t)] \quad (3)$$

$$\mathbf{r}(t + \Delta t) = \mathbf{r}(t) + \Delta t\mathbf{v}(t) + \frac{\Delta t^2}{2m}\mathbf{f}(t) \quad (4)$$

Simulated systems can only have a finite number of particles. In condensed phase, simulations are often performed under periodic boundary conditions to avoid surface effects: this means that when a particle leaves the simulation cell, it comes back into the simulation cell from the other side, like in Pacman universe. As a consequence, a particle interacts with its own (infinite number of) images, as well as all other particles of the system and their images. Unfortunately, infinite summations are not feasible computationally, and some approximation schemes have to be used. Particle interactions are usually subdivided into short range interactions and long range interactions. Such division is not smooth in the cut-off region, and different procedures are used to address this issue.^{60,61}

The simulation procedure described so far yields an NVE ensemble of particles, in contrast to NVT or NPT ensembles which are more often dealt with in experiments. To keep temperature and pressure constant instead of energy, thermostats⁵¹⁻⁵⁵ and barostats^{51, 56-59} are used. A number of schemes have

been suggested in literature, however, Canonical Sampling through Velocity Rescaling (CSVR) thermostat⁵⁵ and Parrinello–Rahman barostat^{56, 57} are used to obtain results in this thesis.

CSVR⁵⁵ thermostat is based on global rescaling of velocities by a factor α at each simulation step. $\alpha = \sqrt{\frac{K_t}{K}}$, where K_t is drawn stochastically from equilibrium kinetic energy distribution and K refers to kinetic energy. However, direct application of the described rescaling significantly perturbs the velocities of the particles, causing large fluctuations in their values during next simulations steps. The method is shown to perform better when distributed over a number of steps:

$$dK = (\bar{K} - K) \frac{dt}{\tau} + 2 \sqrt{\frac{K\bar{K}}{N_f}} \frac{dW}{\sqrt{\tau}} \quad (5)$$

where τ is a coupling constant, N_f refers to number of degrees of freedom and dW is Wiener noise. Under assumption of ergodicity, this thermostat was shown to reproduce NVT ensemble.⁵⁵

Parrinello-Rahman^{56, 57} pressure coupling scheme introduces volume as an additional dynamical degree of freedom of the system.⁶⁰ A matrix \mathbf{b} consisting of box vectors is to follow equation of motion:

$$\frac{d^2 \mathbf{b}}{dt^2} = V \mathbf{W}^{-1} (\mathbf{b}^T)^{-1} (\mathbf{P} - \mathbf{P}_{ref}) \quad (6)$$

where V is the volume of a box, and an inverse mass parameter matrix \mathbf{W}^{-1} contains coupling parameters, and \mathbf{P} is pressure. It is often expressed through a pressure time constant τ_p , and isothermal compressibilities β , L is the largest box matrix element.

$$(\mathbf{W}^{-1})_{ij} = \frac{4\pi^2 \beta_{ij}}{3\tau_p^2 L} \quad (7)$$

Equations of motion for particles in the system also require modifications to include movements of cell vectors. However, this method is better suited for pre-equilibrated systems, as it can induce large fluctuations in the simulation box size if the starting pressure is far from equilibrium.

$$\frac{d^2 \mathbf{r}_i}{dt^2} = \frac{\mathbf{f}_i}{m_i} - M \frac{d\mathbf{r}_i}{dt}; \quad M = \mathbf{b}^{-1} \left(\mathbf{b} \frac{d\mathbf{b}^T}{dt} + \mathbf{b}^T \frac{d\mathbf{b}}{dt} \right) (\mathbf{b}^T)^{-1} \quad (8)$$

2.2 Force Field MD

Classical MD is often called force field MD. In this method particle interactions are represented as a sum of simple analytical functions. They are usually subdivided into bonded and non-bonded interactions. Bonded interactions consist of harmonic potentials for bonds and angles, and simple periodic functions for dihedrals to include possible periodicities. Non-bonded interactions are represented as Coulomb interactions and van der Waals interactions approximated with Lennard–Jones potential.

$$\begin{aligned}
V(q) = & \sum_{bonds} \frac{1}{2} k_{ij}^b (r_{ij} - r_{ij}^0)^2 + \sum_{angles} \frac{1}{2} k_{ijk}^a (\alpha_{ijk} - \alpha_{ijk}^0)^2 \\
& + \sum_{dihedrals} k_{ijkl}^d (1 + \cos(n\theta_{ijkl} - \theta_{ijkl}^0)) \\
& + \sum_{nonbonded\ pairs} \left(\frac{q_i q_j}{r_{ij}} + 4\epsilon_{ij} \left[\left(\frac{\sigma_{ij}}{r_{ij}} \right)^{12} - \left(\frac{\sigma_{ij}}{r_{ij}} \right)^6 \right] \right)
\end{aligned} \tag{9}$$

Exact forms of the equations are force field dependent.⁶²⁻⁶⁴ Historically, force field simulations have been used for protein simulations and majority of the force fields incorporate parameters for proteins only. However, OPLS⁶⁵ force fields do contain parameters for non-protein simulations as well. Additionally, force field parameters for any system can be fitted from higher level quantum chemical simulations.

Sets of bonded parameters are well conserved among different force fields; however non-bonded parameters can have significant variations. This can be clearly seen for parameters for simple ions: as they do not have any bonded parameters, charges are usually also conserved. The only parameters left, for a given ion type, are the Lennard-Jones parameters: ϵ and σ . A number of different sets of parameters for ions have been proposed in literature⁶⁶⁻⁶⁹ based on different fitting procedures. Results of the simulations were shown to be highly force field dependent for a number of systems.⁷⁰⁻⁷²

2.3 *Ab initio* MD

Ab initio MD method is based upon electronic structure calculations coupled with time propagation in MD framework. Current thesis is based on results obtained from Born–Oppenheimer MD⁶¹: electronic structure is solved on every time step for fixed nuclei coordinates; the system is propagated in a ground electronic state, under assumption that excitation energy is significantly larger than $k_B T$.

$$M_I \ddot{\mathbf{R}}_I(t) = -\nabla_I \min_{\Psi_0} \{ \langle \Psi_0 | \hat{H}_0 | \Psi_0 \rangle \} \tag{10}$$

$$E_0 \Psi_0 = \hat{H}_0 \Psi_0 \tag{11}$$

Electronic structure is solved under Density Functional Theory assumptions⁶¹.

$$\min_{\Psi_0} \{ \langle \Psi_0 | \hat{H}_0 | \Psi_0 \rangle \} = \min_{\{\varphi_i\}} E^{KS}[\{\varphi_i\}] \tag{12}$$

$$E^{KS}[\{\varphi_i\}] = T_s[\{\varphi_i\}] + \int d\mathbf{r} V_{ext}(\mathbf{r}) n(\mathbf{r}) + \frac{1}{2} \int d\mathbf{r} V_H(\mathbf{r}) n(\mathbf{r}) + E_{XC}[n] \tag{13}$$

Where $\{\varphi_i(\mathbf{r})\}$ is a set of orthonormal one-particle functions, the Kohn–Sham orbitals. The associated electron density is obtained from a single Slater determinant, $\{f_i\}$ being the occupation numbers.

$$n(\mathbf{r}) = \sum_i^{occ} f_i |\varphi_i(\mathbf{r})|^2 \quad (14)$$

The first term in the Kohn-Sham energy equation is the kinetic energy of a non-interacting system.

$$T_s[\{\varphi_i\}] = \sum_i^{occ} f_i \left\langle \varphi_i \left| -\frac{1}{2} \nabla^2 \right| \varphi_i \right\rangle \quad (15)$$

Second term is the external potential created by the nuclei: Coulomb interaction between the nuclei and between nuclei and electrons.

$$V_{ext}(\mathbf{r}) = \sum_{I < J} \frac{Z_I Z_J}{|\mathbf{R}_I - \mathbf{R}_J|} - \sum_I \frac{Z_I}{|\mathbf{R}_I - \mathbf{r}|} \quad (16)$$

The third term is the Hartree potential, i.e. classical electrostatic interaction of two electron clouds.

$$V_H(\mathbf{r}) = \int d\mathbf{r}' \frac{n(\mathbf{r}')}{|\mathbf{r} - \mathbf{r}'|} \quad (17)$$

And the last contribution is the exchange-correlation functional. This part contains, in principal, all many-body effects which constitute the difference between exact energy and Kohn-Sham decomposition.

Minimization of E^{KS} with respect to the electron density or KS orbitals with fixed number of electrons is done using Lagrangian method of undetermined multipliers. This leads to KS equations

$$\left\{ -\frac{1}{2} \nabla^2 + V_{ext}(\mathbf{r}) + V_H(\mathbf{r}) + \frac{\delta E_{XC}[n]}{\delta n(\mathbf{r})} \right\} \varphi_i(\mathbf{r}) = \sum_j \Lambda_{ij} \varphi_j(\mathbf{r}) \quad (18)$$

$$H_e^{KS} \varphi_i(\mathbf{r}) = \sum_j \Lambda_{ij} \varphi_j(\mathbf{r}) \quad (19)$$

Canonical form of the Kohn-Sham equations can be obtained upon unitary transformation within the space of the occupied orbitals, where $\{\varepsilon_i\}$ is a set of eigenvalues.

$$H_e^{KS} \varphi_i = \varepsilon_i \varphi_i \quad (20)$$

KS equations are solved self-consistently (iteratively) until requested energy convergence level is achieved. Then nuclei are propagated and the process starts again for the next time step.

2.4 Enhanced Sampling Methods

Enhanced sampling techniques^{49, 73} are used to sample PES more efficiently, giving the system extra push or pull to facilitate faster barrier crossings (rare event sampling). All methods can be subdivided into two categories: methods where the system is driven along a reaction coordinate, Umbrella sampling⁷⁴ for example; and methods that do not require reaction coordinate, such as Replica exchange methods⁷⁵. Pictographic representation of the two mentioned methods is given in Figure 1 and Figure 2. For a simple potential presented in Figure 1 for example, if a simulation starts in the right well and the energy barrier is significantly larger than $k_B T$, then for most of the simulation time, the system will stay in the current well and the total PES sampling will be inefficient. In a case where the system crosses the barrier (rare event), sampling of transitional structures will be poor for a finite simulation. Umbrella sampling technique allows increasing sampling of transient structures along a reaction coordinate: additional potentials are added to the reaction coordinate to keep it fixed while all other degrees of freedom of the system are explored (Figure 1). In some cases reaction coordinate cannot be defined for a system, for example conformational space of an intrinsically disordered protein, replica exchange methods then allow to bias all degrees of freedom simultaneously (Figure 2) in a well-defined manner, allowing the system to cross potential barriers quicker.

Umbrella sampling. Consider a system of particles at temperature T , in which the system samples configurations from a canonical ensemble. If s is a reaction coordinate and q are all microscopic coordinates, then the probability distribution for the reaction coordinate is given with a formula, where $\beta = \frac{1}{k_B T}$:

$$P(s) \propto \int dq e^{U(q)\beta} \delta(s - s(q)) \quad (21)$$

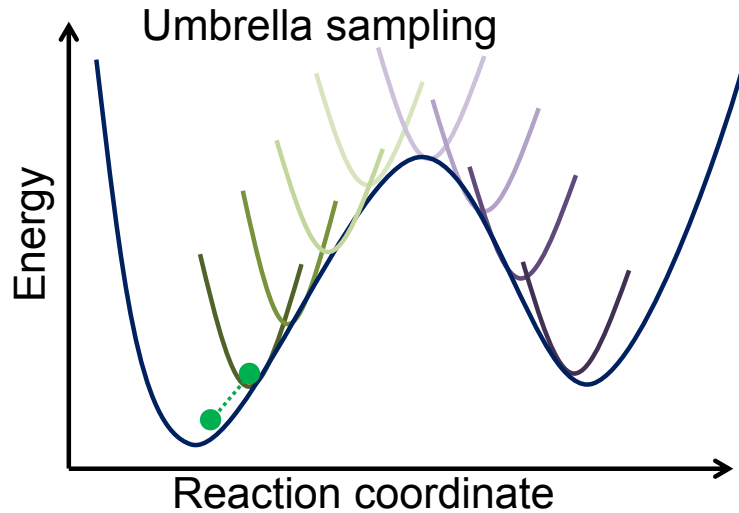


Figure 1. Graphical representation of Umbrella sampling algorithm.

Once additional biasing potential $V(s) = k(s - s_0)^2$ is added to the reaction coordinate, sampled distribution for the reaction coordinate will be:

$$P^*(s) \propto e^{-V(s)/\beta} P(s) \quad (22)$$

It can also be represented as biased free energy landscape, which can be rewritten to get the original free energy landscape:

$$F(s) = F^*(s) - V(s) + C \quad (23)$$

To recover unbiased distribution of any other observable, the relationship between macroscopic probabilities can be utilized as:

$$P^*(q) \propto P(q) e^{-\beta k(s(q)-s_0)^2} \quad (24)$$

Usually, Umbrella sampling MD is done to sample a small area around s_0 ; varying the value of the latter, the whole reaction coordinate can be explored in a number of steps⁷⁶. This results in a number of trajectories with restraints $V_i(s)$ located at different values of the reaction coordinate, which then need to be combined to obtain an overall system behavior, such as free energy landscape $F(s)$, for example. Such task cannot be addressed straight forward due to the differences in offset C_i which depends on $V_i(s)$. Weighted Histogram analysis method is often used for this purpose⁷⁷.

Replica Exchange with Solute Tempering 2. Replica Exchange MD methods, as opposed to the Umbrella sampling, do not require collective variables input. In a Temperature REMD⁷⁵ a number of replicas run simultaneously at different temperatures, and coordinates or thermodynamic parameters are exchanged between them at regular time steps using Monte Carlo procedure (Figure 2). However, the number of replicas scales as a square root of number of degrees of freedom of the system; this naturally limits the method's applicability. It is important to note that the system is heated as a whole, including solvent and its degrees of freedom.

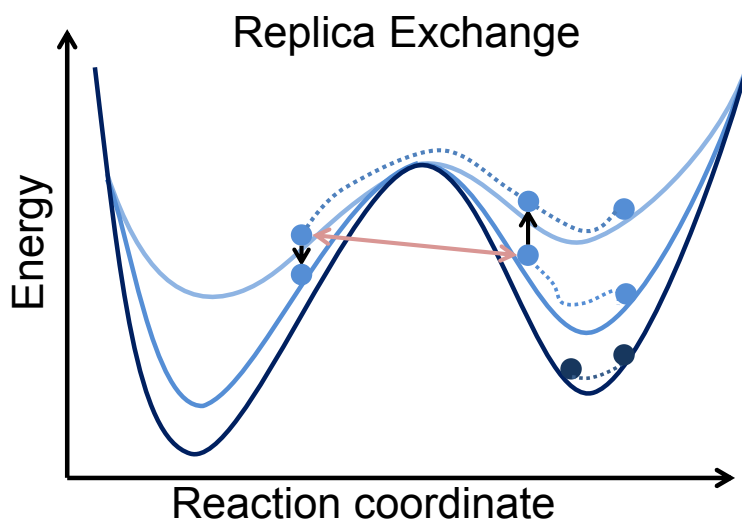


Figure 2. Replica Exchange MD algorithm. Here REX method is only projected to the reaction coordinate for clarity, the method itself is globally affecting PES as a whole.

Hamiltonian REMD^{50, 78} with solute tempering 2 (REST2) was proposed to reduce the number of needed replicas and “to heat” only relevant parts of the system. In REST2 different replicas evolve according to different Hamiltonians. Only potential energies are scaled, while all the replicas run at the same temperature T_0 .

$$E_m(q) = \frac{\beta_m}{\beta_0} E_{pp}(q) + \sqrt{\frac{\beta_m}{\beta_0}} E_{wp}(q) + E_{ww}(q) \quad (25)$$

Here solvent-solute (wp) and solute-solute (pp) interactions are scaled while solvent-solvent (ww) interactions are not scaled. The acceptance criterion for the replicas is:

$$\Delta_{mn} = (\beta_m - \beta_n) \left\{ \left(E_{pp}(q_n) - E_{pp}(q_m) \right) + \frac{\sqrt{\beta_0}}{\sqrt{\beta_m} + \sqrt{\beta_n}} \left(E_{wp}(q_n) - E_{wp}(q_m) \right) \right\} \quad (26)$$

2.5 Computational Spectroscopy

As already mentioned in the introduction, comparison of experimental data with computational can be usually done via spectroscopy. Computed spectroscopic parameters can be directly compared to experimental ones, and once they agree, one gains an atomistic view of the molecular dynamics phenomena of the system under study.

2.5.1 IR Spectra

In quantum chemical calculations IR spectra are often calculated in harmonic approximation⁷⁹. The potential energy is approximated around stationary geometry \mathbf{R}_0 .

$$V(\mathbf{R}) \approx V(\mathbf{R}_0) + \left(\frac{dV}{d\mathbf{R}} \right)^T (\mathbf{R} - \mathbf{R}_0) + \frac{1}{2} (\mathbf{R} - \mathbf{R}_0)^T \left(\frac{d^2V}{d\mathbf{R}^2} \right) (\mathbf{R} - \mathbf{R}_0) \quad (27)$$

As the geometry is stationary, the second term of the equation vanishes, and $V(\mathbf{R}_0)$ can be chosen as zero. Nuclear Schrödinger equation is then solved:

$$\left[- \sum_1^{3N} \left(\frac{1}{2} \frac{\partial^2}{\partial \mathbf{q}_i^2} \right) + \frac{1}{2} \mathbf{q}^T (U(F \cdot G)U^T) \mathbf{q} \right] \Psi_{nuc} = E_{nuc} \Psi_{nuc} \quad (28)$$

Where F is a matrix of force constants, G is a matrix of inverse square roots of masses, U is a unitary transformation into normal coordinate basis; and \mathbf{q} are vibrational normal coordinates and eigenvectors of $(F \cdot G)$ transformation with corresponding eigenvalues ϵ . Vibrational frequencies are related to the eigenvalues as:

$$v_i = \frac{1}{2\pi} \sqrt{\epsilon_i} \quad (29)$$

IR intensities are then calculated as changes in dipole moment along a normal mode. There are other methods that allow calculations of IR spectra in anharmonic approximation from MD trajectories^{80, 81} as well as corresponding normal mode assignment^{82, 83}.

2.5.2 Nuclear Shielding Tensor

When a system is put into homogeneous magnetic field, local magnetic field at any given place is a superposition of external and induced magnetic field^{79, 84}.

$$\mathbf{B}_{loc}(\mathbf{r}) = \mathbf{B}_{ext}(\mathbf{r}) + \mathbf{B}_{ind}(\mathbf{r}) \quad (30)$$

Nuclear magnetic resonance shielding is proportionality constant between applied or external magnetic field and induced magnetic field at any given place. However, only at positions of magnetically active nuclei it can be measured experimentally. According to Bio-Savart-Laplace law current density $\mathbf{j}(\mathbf{r})$ induces magnetic field at position \mathbf{s} .

$$\mathbf{B}_{ind}(\mathbf{s}) = -\sigma(\mathbf{s})\mathbf{B}_{ext} = -\frac{1}{c^2} \int d\mathbf{r} \frac{\mathbf{j}(\mathbf{r}) \times (\mathbf{r} - \mathbf{s})}{|\mathbf{r} - \mathbf{s}|^3} \quad (31)$$

To evaluate $\mathbf{j}(\mathbf{r})$ an electronic structure calculation has to be performed in the presence of the external magnetic field. Kinetic energy term of the Hamiltonian is modified to include vector potential \mathbf{A}_{ext} :

$$\hat{\mathbf{p}} \rightarrow \hat{\mathbf{p}} + \mathbf{A}_{ext} \quad (32)$$

$$\hat{H} = \hat{H}_0 + \mathbf{A}_{ext}\hat{\mathbf{p}} + \frac{1}{2}\mathbf{A}_{ext}^2 \quad (33)$$

Observable magnetic (and electric field) are uniquely determined for the system, unlike the vector potential \mathbf{A}_{ext} . Any gauge function $f(\mathbf{r}, t)$: $\mathbf{A}' = \mathbf{A} + \nabla f$ does not change physical fields. This results in so called gauge origin freedom, also known as gauge origin problem. From a freedom side one can always choose \mathbf{A}_{ext} to be divergenceless (Coulomb gauge) and $rot(\mathbf{A}) = \mathbf{B}_{ext}$.

From a gauge origin problem side, unfortunately, there still exist quite some choices of vector potential. One possible class is shown below; \mathbf{R} is a gauge origin that can be chosen arbitrarily.

$$\mathbf{A}_{ext} = \frac{1}{2}\mathbf{B}_{ext} \times [\mathbf{r} - \mathbf{R}] \quad (34)$$

And the resulting Hamiltonian depends not only on the external magnetic field, but also on the choice of the gauge origin.

$$\hat{H}(\mathbf{B}_{ext}, \mathbf{R}) = \hat{H}(0) + \frac{1}{2}((\mathbf{r} - \mathbf{R}) \times \mathbf{p})\mathbf{B}_{ext} + \frac{1}{8}(\mathbf{B}_{ext} \times (\mathbf{r} - \mathbf{R}))^2 \quad (35)$$

Shielding constants are field independent, thus it is possible to perform a calculation in a low field limit using perturbation theory. Then effective one particle KS Hamiltonians and KS orbitals can be represented as:

$$\hat{h} = \hat{h}^{(0)} + i\hat{h}^{(1)} + O(B_{ext}^2) \quad (36)$$

$$\varphi_k = \varphi_k^{(0)} + i\varphi_k^{(1)} + O(B_{ext}^2) \quad (37)$$

In these equations superscript (0) stands for a zero magnetic field – unperturbed system; and superscript (1) is the first order response. Current density can be also expanded in this framework; the zero order vanishes as there is no current density at zero field.

$$\mathbf{j} = \mathbf{j}^{(1)} + O(B_{ext}^2) = 2 \sum_i^n \left\{ \varphi_i^{(1)} \nabla \varphi_i^{(0)} - \varphi_i^{(0)} \nabla \varphi_i^{(1)} \right\} - 2\mathbf{A}_{ext} \sum_i^n \varphi_i^{(0)} \varphi_i^{(0)} \quad (38)$$

The first term, involving the perturbed orbitals, is called the paramagnetic term, and the second term is called diamagnetic. To calculate the total current density, orbitals need to be expanded in a finite basis set, and it is not always possible for the first order orbitals, firstly (to be first?). Second, $\{\varphi_i^{(1)}\}$ are gauge dependent. To address these issues, a number of distributed gauge origins approaches have been proposed^{85, 86}. In Individual Gauge for Localized Orbitals (IGLO)⁸⁷ method $\{\varphi_i^{(1)}\}$ orbitals are approximated by localized molecular orbitals; and their charge centers are used as distributed gauge origins. It was the first method to produce accurate results; however, there are a numerous issues: orbital localization is not unique; not all methods allow orbital localization. In Gauge Including Atomic Orbitals (GIAO)^{88, 89} method, distributed gauge origins are introduced on the level of basis set functions: an exponential term depending on vector potential is added to every atomic orbital. Continuous Set of Gauge Transformations (CSGT)^{90, 91} is based on evaluation of the current density on a grid using different gauge origin for every grid point.

2.5.3 Hyperfine Coupling Tensor

Hyperfine interaction occurs between unpaired electrons and magnetically active nuclei. It is described as a 3×3 tensor, and is usually separated into isotropic and anisotropic or dipolar components. $A_{iso}(N)$ are proportional to Fermi contact term⁹² or electron spin densities at the position of a corresponding nucleus.

$$A_{iso}(N) = \frac{4\pi}{3} \beta_e \beta_N g_e g_N \langle S_z \rangle^{-1} \sum_{\mu, \nu} \rho_{\mu, \nu} \langle \varphi_\mu | \delta(\mathbf{r}_N) | \varphi_\nu \rangle \quad (39)$$

Where β_e is the Bohr magneton, β_N is the nuclear magneton, g_e is the free electron g factor, g_N is g factor of the nucleus, $\langle S_z \rangle$ is expectation value of the z component of total electronic spin, $\rho_{\mu, \nu}$ is the spin density matrix.

$$T_{kl}(N) = \frac{1}{2} \beta_e \beta_N g_e g_N \langle S_z \rangle^{-1} \sum_{\mu, \nu} \rho_{\mu, \nu} \left\langle \varphi_\mu \left| \frac{\mathbf{r}_N^2 \delta_{kl} - 3\mathbf{r}_{N,k} \mathbf{r}_{N,l}}{r_N^{-5}} \right| \varphi_\nu \right\rangle \quad (40)$$

Here $\mathbf{r}_N = \mathbf{r} - \mathbf{R}_N$. T is always a traceless tensor; and can be estimated from pure nuclear geometries under an assumption that electron is a point charge and can be localized to a point in space.

A_{iso} is purely quantum mechanical, and requires a lot of caution in calculation. Firstly, hyperfine coupling constants (HFCC) calculations require accounting for electron correlation effects, and unfortunately there are no easy solutions, and choice of the exchange-correlation functional is very much system dependent⁸⁴. Second, as A_{iso} depends heavily on the local quality of the wave function at the nuclei, Slater type orbitals are preferred. However, the STOs are harder to handle and Gaussian type orbitals are employed in majority of the calculations. Addition of very tight s functions to the basis sets was shown to reproduce reliable HFCC values⁹³.

3 Overview of Published Papers

3.1 Solvent Driven Proton Tautomerism in Strong Hydrogen Bonds

Proton tautomerism in complexes with strong hydrogen bonds has been investigated with specific focus on influence of solvent-solute interactions in Publication P1. A number of H-bonded complexes of chloroacetic acid with substituted pyridines was studied by low temperature NMR and FTIR experiments in dichloromethane (DCM). Different substitutions of pyridine changed its pK_a value from -0.44 to 9.6 . The complexes formed with the acid ranged from molecular types ($\text{OH}\cdots\text{N}$), where bridging proton stayed at the acid's side, to zwitterionic ones ($\text{O}^-\cdots\text{HN}^+$), where proton transfer to pyridine moiety occurred. Changes in H-bond geometry of the complexes were reflected in changes of bridging proton NMR chemical shifts, and ^{13}C NMR chemical shifts of acid's carbons as well as the frequency of the C=O stretching mode of the acid. For both ends of the pyridine proton accepting ability range, the situation was simple as compared to its middle, *i. e.* to the region with strongest (shortest) hydrogen bonds. Here FTIR bands exhibited a double peak structure in the C=O signature region (see Figure 3 top left for an example), pointing at fast (picosecond-scale) proton tautomerism in the system: the process is visible in IR timescales, however is too fast in NMR timescales. This is an interesting observation on its own: proton tautomerism is found for a very strong, almost central-symmetric H-bond. Bridging proton moves in an effective double well potential where proton motion occurs along a reaction coordinate which also includes solvent molecules' motion. To investigate the molecular system in fine detail on the corresponding timescales, *ab initio* MD simulations of chloroacetic acid complex with methylpyridine surrounded explicitly by 71 DCM molecules were performed.

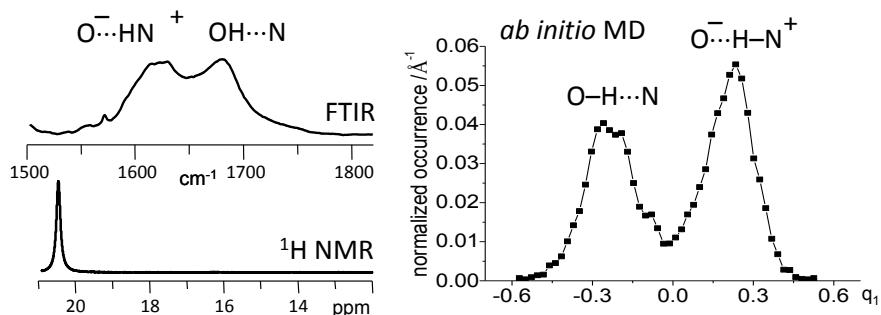


Figure 3. Data for chloroacetic acid complex with methylpyridine in DCM. Part of experimental FTIR ($\nu(\text{C}=\text{O})$ and $\nu_{\text{as}}(\text{CO}_2)$) and ^1H NMR spectra at 179 K (left); distribution of the hydrogen bond asymmetry parameter

$$q_1 = \frac{1}{2}(r_{\text{OH}} - r_{\text{HN}}) \text{ along AIMD trajectory.}$$

Ab initio MD approach allowed following proton motion in the hydrogen bond, as well as solvation shell dynamics in atomistic detail in picoseconds regime. To address H-bond geometry linear combination of the interatomic distances⁵ was employed: $q_1 = \frac{1}{2}(r_{\text{OH}} - r_{\text{HN}})$ representing shift of the bridging proton from the H-bond center in a case of a linear bond and $q_2 = r_{\text{OH}} + r_{\text{HN}}$, which gives H-bond length in the linear case. Those two distances were shown to be interdependent: shorter H-bonds are more symmetric, whereas longer H-bonds are more asymmetric. Histogram of q_1 values

along the MD trajectory (Figure 3 right) is broad and showed clear two peak structure: with peaks corresponding to molecular and zwitterionic forms of the complex. It should be specifically noted here that proton transfer between the forms occurs in a double well potential along a complex reaction coordinate which includes reorientation of solvent molecules.

In order to describe the kinetics of the proton tautomerism, one has to take into account that bridging proton takes part in a number of different motions at the same time: proton stretching vibration (period of ca. 20 fs, keeping in mind that all protons were simulated with double mass) being the fastest. Filtering approach with memory time τ was used to obtain average tautomer lifetimes from the trajectory. The lifetimes of the tautomers, depending on the value of τ , were found to be of about a picosecond, interestingly, roughly matching the rotational diffusion times of the DCM molecules. Various parameters have been calculated to investigate solvent-solute interactions in more detail: strength of the electric field at the bridging proton position, and at the center of the H-bond generated by solvent molecules; relative solvent ordering, and specific orientation of solvent molecules around the H-bond (Figure 4). Our analysis revealed that specific solvent-solute interactions, i.e. formation of $\text{CH}\cdots\text{O}$ H-bonds carbonyl oxygen atom of the acid plays a dominant role, whereas electric field fluctuations (PCM-like approach) have minor influence on the OHN H-bond geometry.

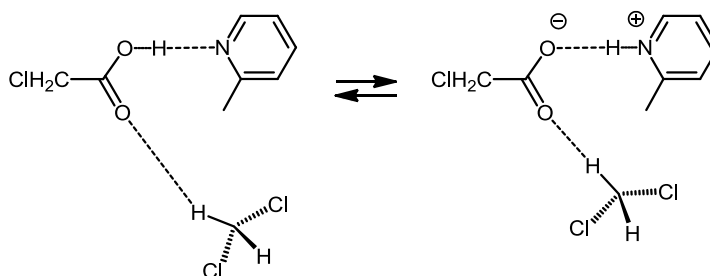


Figure 4. Schematic representation of the $\text{OH}\cdots\text{N}$ (left) and $\text{O}^-\cdots\text{HN}^+$ (right) structures with relative positions of the solvent molecule nearest to carbonyl oxygen atom of the acid.

Power spectrum was calculated as a velocity autocorrelation function from the trajectory^{80, 81}, and corresponding normal modes analysis was performed to assign the bands^{82, 83}. It revealed a double peak structure in the signature range of the C=O stretch which agrees well with the experimental FTIR spectrum. NMR chemical shifts have been calculated for a number of random snapshots along the trajectory. $\delta(^1\text{H})$ as a function of q_1 showed expected bell shape: shifts being smaller for asymmetric proton position and reaching the maximum in the center when bridging proton is maximally deshielded. Distribution of the $\delta(^1\text{H})$ covered a range from 12.5 to 24.5 ppm. The average value of the proton chemical shift agreed well with experimentally measured one (20.1 ppm to 20.5 ppm respectively).

3.2 Influence of Fluctuating Solvent-Solute Hydrogen and Halogen Bonds on FHF^- Anion

Publication P2 focuses on the influence of the specific solvent-solute interactions on the H-bond geometry of the FHF^- anion, counteraction was not included into the simulation box. FHF^- is a classic example of a very strong symmetric H-bond⁹⁴, the properties of which have been extensively investigated experimentally^{19, 94, 95} and theoretically^{96, 97}. A highly symmetric nature of the anion makes it one of the strongest H-bonded complexes with gas phase complexation energy of 44

kcal/mol.⁹⁸ It was shown theoretically that bridging proton moves in a central symmetric highly anharmonic potential.⁹⁶ When F...F distance is increased the potential turns into a double well.⁹⁹ It can be argued that in a condensed phase, interactions with solvent molecules can drive proton motion in a similar fashion as for OHN H-bond, as described in P1. Additionally, fluorine atoms with three lone pairs are expected to be highly susceptible to interactions with solvent molecules. *Ab initio* MD was used to investigate the picosecond changes in the geometry of the anion due to its interactions with the surrounding solvent molecules of DCM or tetrachloromethane (CCl₄); *ab initio* MD trajectory in vacuum was used as a benchmark. Distribution of anion geometry changed upon solvation, containing more asymmetric structures. Moreover, wider distribution of structures was found in CCl₄ than in DCM, which was unexpected as CCl₄ is thought to be a very inert solvent. Fluorine atom can donate its electron density; it can accept hydrogen bonds and take part in halogen bonds with another halogen: interactions of fluorine atom lone pairs with σ -hole of chlorine atoms in the systems. Weak CH...F interactions were found to dominate over possible halogen bonds in DCM. In CCl₄ only halogen CCl...F interactions are possible. Properties of these interactions were investigated for the trajectories: geometry of the bonds, number of the interacting molecules and their relative orientation. Halogen bonds as well as hydrogen bonds were formed along the lone pairs of fluorine atom; on average every fluorine atom has two interacting partners. However, at some points of time the anion is solvated asymmetrically (Figure 5). Furthermore, asymmetry of the solvation shell correlates well with the changes in the bridging proton position in the anion for both solvents. When one fluorine atom has relatively more interactions with the solvent molecules, bridging proton tends to shift to the other, less solvated fluorine atom. For CCl₄ this effect is more pronounced: asymmetric solvation distorts FHF⁻ geometry more, causing larger fluctuations in q_1 values of the hydrogen bond⁵. Distribution of solvent-solute interaction lifetimes along the trajectories shows, that lifetime for CCl₄ is twice longer than that for DCM molecules.

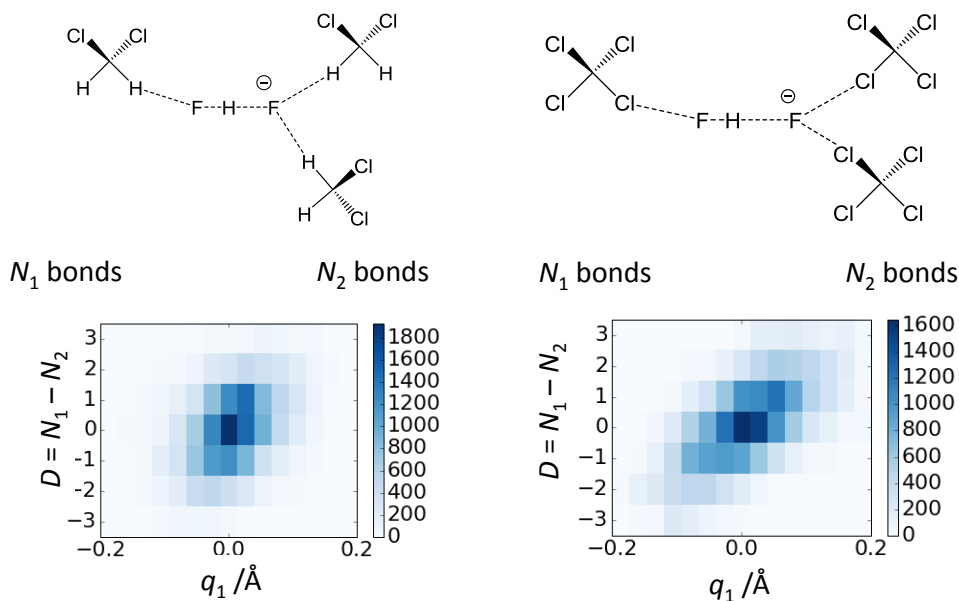


Figure 5. Correlation between solvation shell asymmetry and the hydrogen bond geometry of FHF⁻ in DCM (left) and CCl₄ (right)

The calculated power spectra of FHF⁻ (Figure 6) show differences in band positions of bending and asymmetric stretch as compared to vacuum, while relative differences between the solvents are

comparably less pronounced. Bending frequency is red shifted upon solvation; asymmetric stretch frequency increases and band shape becomes more anisotropic.

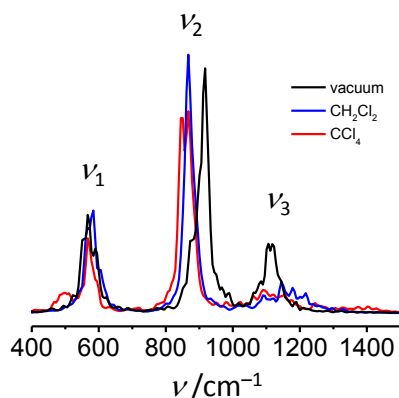


Figure 6. Power spectra of FHF⁻ in vacuum (black line), in DCM (blue line) and in CCl₄ (red line).
 ν_1 symmetric stretch, ν_2 bending, ν_3 asymmetric stretch.

NMR chemical shifts were calculated for all three systems for a number of random snapshots from the trajectories: 30 for FHF⁻ in vacuum and 100 for condensed systems. $\delta(^1\text{H})$ and $\delta(^{19}\text{F})$ respond sensitively to changes in the anion geometry along the trajectories, and a wide distribution of those parameters was observed. Additionally, $\delta(^{19}\text{F})$ was as well highly sensitive to changes in the solvation. Average value for $\delta(^{19}\text{F})$ changing from -292 ppm to -210 ppm and to -147 ppm in vacuum, DCM, and CCl₄ respectively.

3.3 Molecular Mechanism of Overhauser Dynamic Nuclear Polarization in Insulating Solids

Publication P3 is based on the MD study of a particular organic radical BDPA (Figure 7) and its relation to a recently discovered Overhauser effect DNP (OE-DNP) in insulating solids. The effect was recently discovered experimentally²¹ and is exclusively operative in the BDPA radical. Further experimental investigation showed the effect to be matrix dependent²² and operative even at 1.2 K ²³. OE-DNP relies on difference in rates of electron-nuclei zero-quantum and double-quantum relaxation pathways²⁵. Those cross-relaxation transitions are mediated by fluctuating hyperfine interaction. This indicates that BDPA radical had a motion at a rate close to EPR transition (hundreds of GHz, or in picosecond regime in time units) causing hyperfine coupling constants of BDPA protons to fluctuate.

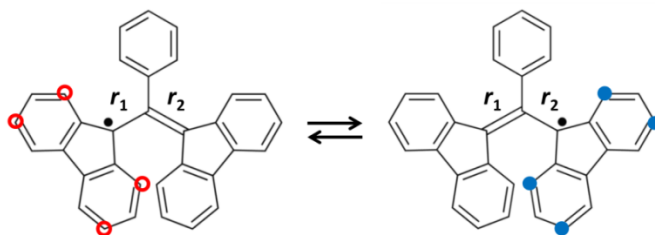


Figure 7 Structure of the BDPA radical, positions of protons with highest values of HFCCs are marked in color.

Investigation was based on classical MD simulation of the radical in a glassy ortoterphenyl matrix as well as *ab initio* MD of the radical in vacuum. Hyperfine coupling constants (HFCC) were calculated every 0.3 ps for both systems. Proton positions with the largest values of isotropic HFCCs are marked in color in Figure 7 above: red and blue groups. Fluctuation pattern of the two groups revealed that they were not only fluctuating in a required time regime, but the fluctuations were also in an out-of-phase way. Those observations suggested underlying geometric motion to be a sort of antisymmetric stretch. A parameter of structure asymmetry $q = r_1 - r_2$ was then introduced; this asymmetry parameter corresponds to structural fluctuations depicted in Figure 7. Its frequency spectrum had a clear peak at around 600 GHz (1.7 ps) and a noticeable signal all the way down to 150 GHz, especially for the BDPA embedded in solvent matrix (Figure 8 left). Plotting q against the scalar coupling A_{iso} of the red group confirms the relationship (Figure 8 right). Interestingly, comparably small geometric changes (change in q value of only 10 pm) cause large changes in the HFCC value (in order of a couple MHz). Vibrational nature of q fluctuations meant the process was active even at very low temperatures.

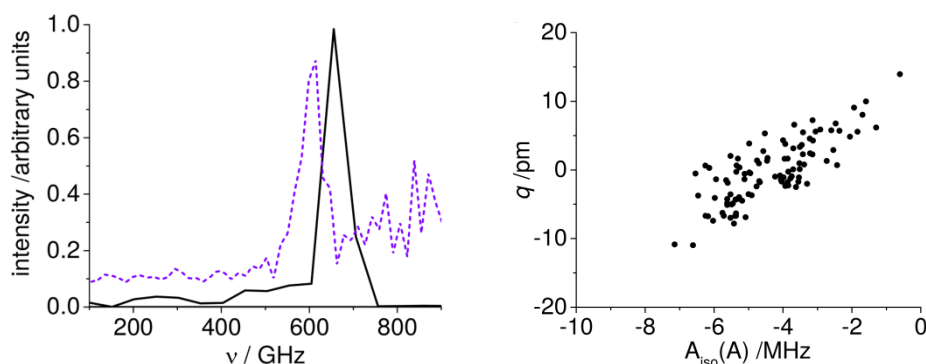


Figure 8. Spectral density of fluctuations of asymmetry parameter $q = r_1 - r_2$ (left): black solid line for BDPA in vacuum; purple dashed line for BDPA in ortoterphenyl matrix. Correlation between q and isotropic part of HFCCs of the red protons' group (red open circles in Figure 7 left) in vacuum (right).

Spectral density of HFC fluctuations at 264 GHz was then used in Spin Dynamics framework to obtain field profile of DNP. Obtained DNP spectrum is in very good agreement with the experiment.

3.4 Salt Bridge in Aqueous Solution of Simple Salts

Publication P4 investigates effects of simple ions on the stability of an Arginine-Aspartate salt bridge. Classical MD simulation of the salt bridge in pure water as well as in 1M aqueous solutions of NaI, NaCl, LiI, LiCl were performed at ambient conditions. Choice of ions was made along Hofmeister²⁶

“salting in”/“salting out” lines: smaller, more compact ions have more kosmotropic character, whereas bulkier ions are more chaotropic. Special focus of current work was put on competition between formations of different ion pairs in solution. As charged amino acids of the salt bridge can, in principle, form ion pairs with simple ions altering stability of the salt bridge.

There are two main timescales of motions in the system: water reorientation around the solvated species: Asp⁻, Arg⁺, and ions, lies in nanosecond regime; and opening of the salt bridge, which is slower, tens to hundred nanoseconds. Umbrella pulling MD was performed to address both processes. Sampling was done along a distance between charge centers of the salt bridge amino acids as a reaction coordinate. Additionally, for water and NaCl pulling along C_α-C_α distance was performed. Analysis of the MD trajectories showed that water structure became more rigid for all salts: with the emergence of a slower rotational relaxation process (Figure 9 left). Furthermore, only water molecules in direct contact with ions were shown to be affected, which agrees with a current picture of ion influence¹⁰⁰. Lifetimes of such aggregates were computed and agreed well with the Hoffmeister series: more kosmotropic Li⁺ and Cl⁻ formed longer-lived aggregates with water molecules as compared to more chaotropic Na⁺ and I⁻. In agreement with this finding (local influence), lifetimes of water-Asp⁻ and water-Arg⁺ aggregates were constant for all trajectories. Interactions of additional ions with the salt bridge as well fell along the Hofmeister lines, Li⁺ - Asp⁻ ion pair being the most long lived, while bulkier charged group of Arg⁺ interacted weaker with halogen anions.

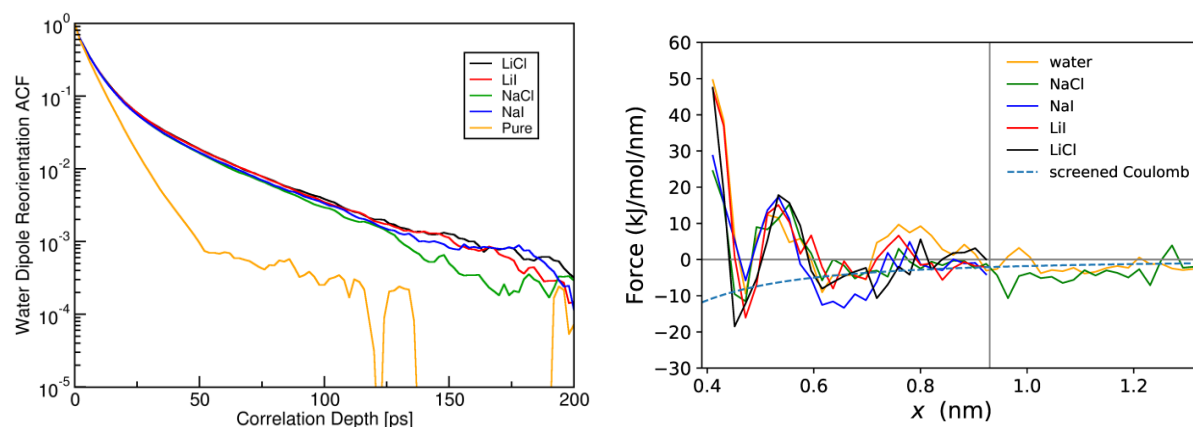


Figure 9. Vector autocorrelation functions of the dipole vector of water for all studied systems (left). Mean force as a function of distance between guanidinium carbon - carboxylic carbon of the Arg-Asp (right).

Shape of the potential of the mean force along the dissociation pathway (Figure 9 right) of the salt bridge did not show ion-specific effects above the noise level. Additionally, shape of the curve for the solvated salt bridge indicates that commonly assumed role of fully solvated salt bridges as structural driving forces may need to be revised.

3.5 Conformational Ensemble of Polyglutamine-14 Chain

Publication P5 deals with conformational space of solvated Polyglutamine-14 peptide with grafted specific FRET-related chromophores followed by a specific solubility tail (WQ14W-tail). Polyglutamine proteins belong to a family of intrinsically disordered proteins: they do not have regular secondary structure as monomers³⁶ and have a very frustrated potential energy landscape with very small regular secondary structure contents.⁴² However, recent review states that “toxic

monomer” hypothesis is an elusive but feasible concept.³⁶ Combination of Hamiltonian Replica Exchange⁵⁰ MD with moderately coarse-grained Monte-Carlo simulations¹⁰¹ was employed to tackle motions in the system occurring in sub-microsecond regime. MD simulations of 12 replicas spanning over 296 K to 600 K were performed for 232 ns per replica, amounting to a full 2.7 μ s simulation time. Results of the simulations were analyzed with a combination of biochemistry analysis toolkit and polymer analysis methods. Special attention was given to transiently stable structures that can facilitate further aggregation.

Distance between the two FRET chromophores was used as a key structural parameter, as it can be then directly compared with experimental FRET data. Radius of gyration of the chain, and its relative shape anisotropy, show wide distribution of values along the reaction coordinate, which is in line with highly flexible nature of Polyglutamine. Based on radius of gyration and partial shape anisotropy, three transiently stable structural motifs have been identified (Figure 10). Those clusters of structures have specific hydrogen bonding pattern and can be characterized as β -turns in different positions of the sequence with overall population of around 3%. Such structures have on average 3.5 backbone–backbone hydrogen bonds per frame on average. Peak at small distances corresponds to structures where chromophores are in contact ($d \approx 0.5$ nm in Figure 10 left); probability for these types of structures was around 13%. Some structures in this group correspond to β -hairpin like structure (~ 1 %), while majority are in an open loop like conformations. Next peak at $d \approx 1$ nm (Figure 10 left) corresponds to a turn in position Q5 to Q8. And the last feature at $d \approx 1.6$ nm (Figure 10 left) corresponds to a turn in positions Q8 to Q11, where it should be noted that these conformations are stabilized by hydrogen bonds between the backbone of the main Polyglutamine chain and the backbone of the solubility tail.

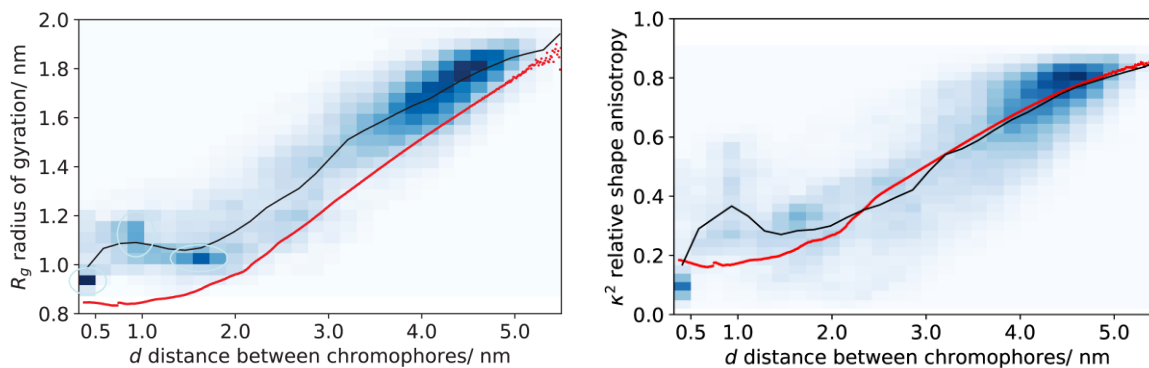


Figure 10. Correlation between distance between the chromophores and radius of gyration (left) and partial anisotropy (right) for the WQ14W-tail chain. 2D histograms correspond to MD data; solid black line corresponds to averaged MD data (averaging along vertical axis); red scatter corresponds to Monte-Carlo results.

To investigate specific influence of chromophores and solubility tail, additional systems were studied within SAMC/PRIME20¹⁰² framework: Q14 with chromophores but without the solubility tail WQ14W and Polyglutamine-16 Q16. The data showed modest influence of chromophores on protein structure. Whereas, solubility tail perturbed system behavior to a greater extent: formation of additional transiently stable structures with the tail, and, particularly, destabilization of β -hairpin structure at small inter chromophore distance.

4 Conclusions

The purpose of this thesis was to investigate the complex interplay of specific intra- and intermolecular interactions in the condensed phase, and to compute their associated spectroscopic signatures. For small hydrogen bonded complexes, fast proton dynamics within the hydrogen bonds was shown to be coupled the dynamics of solvent molecules in a very specific way, namely via transient weak specific directed interactions. Often those interactions were competing: as for a solvated FHF^- anion, there is a competition between halogen and hydrogen bonding with solvent molecules. For large, complex systems, the number of competing interactions increases drastically. This, combined with reduced kinetics, has been addressed by use of enhanced sampling techniques. The latter allowed bridging the large span of timescales of the dynamical processes observed in such large systems: from nanosecond-scale water reorientation dynamics, to microseconds-scale conformational changes in proteins. Calculated geometric parameters in an all-atom resolution allowed to solve a forward problem: calculation of corresponding spectroscopic parameters, sampled from molecular dynamics simulations trajectories.

In the first project, a series of OHN hydrogen bonded complex was investigated by a combination of *ab initio* MD simulations; NMR chemical shifts calculations and IR vibrational analysis through trajectory sampling; combined with experimental NMR and FTIR study. Proton accepting ability of substituted pyridines was modified to allow variation in the OHN hydrogen bond geometry: ranging from molecular to zwitterionic form of the complexes. In the middle of this range, NMR spectra showed formation of strong hydrogen bonds, and FTIR spectra revealed the presence of proton tautomerism. To gain an atomistic picture of the proton tautomerism in the system, one of the complexes was further studied by *ab initio* MD simulations: using a complex of methylpyridine with chloroacetic acid surrounded by 71 CH_2Cl_2 molecules. The distribution of hydrogen bond geometries in the ensemble of solvatomers was very broad and showed a clear double peak structure which can be attributed to molecular and zwitterionic forms of the complex. Further analysis of solvent-solute interactions revealed that fluctuations of electric field generated by dipole moments of solvent molecules in the solvation shell are weakly correlated to the hydrogen bond geometry. However, the formation of specific interactions between carbonyl carbon atom of the acid, and protons of CH_2Cl_2 molecules, correlated well with the OHN hydrogen bond geometry, and can be deemed as one of the main causes for proton jumps within the H-bond.

In the second project, solvent-solute interactions of a FHF^- anion with aprotic solvents were investigated. *Ab initio* MD simulations of the anion in vacuum, CH_2Cl_2 and CCl_4 were performed. FHF^- anion is a classic example of a very strong H-bond, and solvent-solute interactions with neither of the solvents were able to change its average $D_{\infty h}$ symmetry. However, interactions with solvent molecules changed distribution of the H-bond geometries: distribution of the bridging proton positions in the hydrogen bond is wider in CH_2Cl_2 than in vacuum, and even wider in CCl_4 . Those interactions were further analyzed: they were preferentially oriented along lone pairs of fluorine atoms; their length was shorter than sum of Bondi radii of participating atoms. Weak halogen bonds between chlorine atoms of CCl_4 and fluorine atoms of the anion were more effective in breaking the symmetry of the anion, in comparison to weak hydrogen bonding between protons of CH_2Cl_2 molecules and the fluorine atoms of the anion. Additionally, the asymmetry of the solvation shell – when one fluorine atom has more interactions than the other one – was shown to correlate with the bridging proton displacement from the center of the H-bond. NMR chemical shifts of the bridging proton were shown to respond sensitively to the hydrogen bond geometry fluctuations as well as on the solvent. ^{19}F chemical shifts exhibited huge solvent effects, mainly due to changes in the limiting

chemical shift of the FH species. Vibrational analysis also showed high sensitivity of the bands to changes in the anion geometry.

The third project succeeded in explaining molecular motions of a fluxional radical that facilitate Overhauser Effect Dynamic Nuclear Polarization in insulating solids. Molecular dynamics of the radical contain a particular slow vibrational mode that breaks the symmetry of the allyl part of the radical. This motion is coupled with changes in localization of the unpaired electron, inducing an apparent motion of the unpaired electron. Apparent motion of the electron in turn causes fluctuations in the hyperfine interactions between the electron and protons of the radical. All such motions lie within range of electronic transitions in current experimental setups, and Spin Dynamics calculations were able to reproduce all features of the field spectrum (DNP enhancement as a function of magnetic field strength).

For larger biological systems, interplay of different effects was analyzed. For a fully solvated salt bridge between Arginine and Aspartic acid anion in pure water, and in 1 M aqueous salt solutions, analysis showed that Hofmeister ions do influence properties of the salt bridge as well as water in a very local and specific way: smaller and more kosmotropic ions form longer lived ion pairs with water and the amino-acids, whereas larger and more chaotropic ions ion-pairs were found to be shorter lived. Remarkably, Li^+ formed very long-lived ion pairs with Asp^- (approximately during 50% of performed simulations). Additionally, the enthalpic function of a fully solvated salt bridge was minor, regardless of solvent composition; meaning that studied salt bridge is a structure stability element but not a structural driving force. For Polyglutamine-14 with grafted FRET related chromophores, and four residue solubility tail conformational space was investigated. Additionally, interactions of the tail and the chromophores with the main chain were examined. Competition between backbone-backbone hydrogen bonding and sidechain-backbone hydrogen bonding was addressed. Glutamines are renowned for their ability to form sidechain-backbone hydrogen bonds to increase self-interaction and decrease surface area. Indeed, even for the extended chain, at least two hydrogen bonds were present on average, whereas at small distances that number rose to six on average. Analysis revealed that the chain is highly flexible, with a small percentage of regular transiently stable secondary structures (~3%). However, those transiently stable structures are in β -turn conformations, which are argued to be of importance for early stages of nucleation. Chromophores were found to have little influence on chain properties. However, the four residue solubility tail has been found to cause more specific changes: such as the formation of different transiently stable structures, including the tail. Effect of the tail was similar to the effect of flanking residues of Polyglutamine segment of huntingtin protein, and can be of importance for future investigations of the real protein.

5 References

1. P. Hobza, K. Müller-Dethlefs and R. S. o. Chemistry, *Non-covalent Interactions: Theory and Experiment*, Royal Society of Chemistry 2010.
2. A. Y. Ben-Naim, *Hydrophobic Interactions*, Springer US 2012.
3. G. Gilli and P. Gilli, *The Nature of the Hydrogen Bond: Outline of a Comprehensive Hydrogen Bond Theory*, OUP Oxford 2009.
4. T. Murakhtina, J. Heuft, E. J. Meijer and D. Sebastiani, *ChemPhysChem*, 2006, **7**, 2578-2584.
5. H.-H. Limbach, P. M. Tolstoy, N. Pérez-Hernández, J. Guo, I. G. Shenderovich and G. S. Denisov, *Israel Journal of Chemistry*, 2009, **49**, 199-216.
6. H.-H. Limbach, M. Pietrzak, S. Sharif, P. M. Tolstoy, I. G. Shenderovich, S. N. Smirnov, N. S. Golubev and G. S. Denisov, *Chemistry – A European Journal*, 2004, **10**, 5195-5204.
7. B. Koepe, S. A. Pylaeva, C. Allolio, D. Sebastiani, E. T. J. Nibbering, G. S. Denisov, H. H. Limbach and P. M. Tolstoy, *Physical Chemistry Chemical Physics*, 2017.
8. B. Koepe, P. M. Tolstoy and H.-H. Limbach, *Journal of the American Chemical Society*, 2011, **133**, 7897-7908.
9. P. M. Tolstoy, J. Guo, B. Koepe, N. S. Golubev, G. S. Denisov, S. N. Smirnov and H.-H. Limbach, *The Journal of Physical Chemistry A*, 2010, **114**, 10775-10782.
10. P. M. Tolstoy, B. Koepe, G. S. Denisov and H.-H. Limbach, *Angewandte Chemie International Edition*, 2009, **48**, 5745-5747.
11. C. L. Perrin, *Pure and Applied Chemistry*, 2009, **81**, 571-583.
12. C. L. Perrin and J. S. Lau, *Journal of the American Chemical Society*, 2006, **128**, 11820-11824.
13. L. O. Paulson and D. T. Anderson, *The Journal of Physical Chemistry A*, 2009, **113**, 1770-1778.
14. T. Yamashita and K. Takatsuka, *The Journal of Chemical Physics*, 2007, **126**, -.
15. F. Dahms, R. Costard, E. Pines, B. P. Fingerhut, E. T. J. Nibbering and T. Elsaesser, *Angewandte Chemie International Edition*, 2016, **55**, 10600-10605.
16. S. Pylaeva, C. Allolio, B. Koepe, G. S. Denisov, H.-H. Limbach, D. Sebastiani and P. M. Tolstoy, *Physical Chemistry Chemical Physics*, 2015, **17**, 4634-4644.
17. M. Garcia-Viloca, À. González-Lafont and J. M. Lluch, *Journal of the American Chemical Society*, 1999, **121**, 9198-9207.
18. P. Sebald, A. Bargholz, R. Oswald, C. Stein and P. Botschwina, *The Journal of Physical Chemistry A*, 2013, **117**, 9695-9703.
19. K. Kawaguchi and E. Hirota, *Journal of Molecular Structure*, 1995, **352-353**, 389-394.
20. J. Almlöf, *Chemical Physics Letters*, 1972, **17**, 49-52.
21. T. V. Can, M. A. Caporini, F. Mentink-Vigier, B. Corzilius, J. J. Walish, M. Rosay, W. E. Maas, M. Baldus, S. Vega, T. M. Swager and R. G. Griffin, *The Journal of Chemical Physics*, 2014, **141**, 064202.
22. M. Lelli, S. R. Chaudhari, D. Gajan, G. Casano, A. J. Rossini, O. Ouari, P. Tordo, A. Lesage and L. Emsley, *Journal of the American Chemical Society*, 2015, **137**, 14558-14561.
23. X. Ji, T. V. Can, F. Mentink-Vigier, A. Bornet, J. Milani, B. Vuichoud, M. A. Caporini, R. G. Griffin, S. Jannin, M. Goldman and G. Bodenhausen, *Journal of Magnetic Resonance*, 2018, **286**, 138-142.
24. O. Haze, B. Corzilius, A. A. Smith, R. G. Griffin and T. M. Swager, *Journal of the American Chemical Society*, 2012, **134**, 14287-14290.

25. A. S. Lilly Thankamony, J. J. Wittmann, M. Kaushik and B. Corzilius, *Progress in Nuclear Magnetic Resonance Spectroscopy*, 2017, **102-103**, 120-195.
26. F. Hofmeister, *Archiv für experimentelle Pathologie und Pharmakologie*, 1888, **24**, 247-260.
27. G. Stirnemann, E. Wernersson, P. Jungwirth and D. Laage, *Journal of the American Chemical Society*, 2013, **135**, 11824-11831.
28. J. Boisson, G. Stirnemann, D. Laage and J. T. Hynes, *Physical Chemistry Chemical Physics*, 2011, **13**, 19895-19901.
29. H. Langer and H. G. Hertz, *Berichte der Bunsengesellschaft für physikalische Chemie*, 1977, **81**, 478-490.
30. M. D. Smith and L. Cruz, *The Journal of Physical Chemistry B*, 2013, **117**, 14907-14915.
31. Q. Liao, M. C. Owen, S. Bali, B. Barz and B. Strodel, *Chemical Communications*, 2018, **54**, 7766-7769.
32. M. Senske, D. Constantinescu-Aruxandei, M. Havenith, C. Herrmann, H. Weingärtner and S. Ebbinghaus, *Physical Chemistry Chemical Physics*, 2016, **18**, 29698-29708.
33. D. E. DRAPER, *RNA*, 2004, **10**, 335-343.
34. H. R. Bosshard, D. N. Marti and I. Jelesarov, *Journal of Molecular Recognition*, 2004, **17**, 1-16.
35. J. E. Donald, D. W. Kulp and W. F. DeGrado, *Proteins: Structure, Function, and Bioinformatics*, 2011, **79**, 898-915.
36. R. Wetzel, *Journal of Molecular Biology*, 2012, **421**, 466-490.
37. S. Chen, V. Berthelier, W. Yang and R. Wetzel, *Journal of Molecular Biology*, 2001, **311**, 173-182.
38. H. Y. Zoghbi and H. T. Orr, *Annual Review of Neuroscience*, 2000, **23**, 217-247.
39. A. S. Holehouse and R. V. Pappu, *Annual Review of Biophysics*, 2018, **47**, 19-39.
40. S. L. Crick, M. Jayaraman, C. Frieden, R. Wetzel and R. V. Pappu, *Proceedings of the National Academy of Sciences*, 2006, **103**, 16764-16769.
41. A. Vitalis, X. Wang and R. V. Pappu, *Journal of Molecular Biology*, 2008, **384**, 279-297.
42. D. Punihaole, R. S. Jakubek, R. J. Workman, L. E. Marbella, P. Campbell, J. D. Madura and S. A. Asher, *The Journal of Physical Chemistry B*, 2017, **121**, 5953-5967.
43. A. De Simone, L. Esposito, C. Pedone and L. Vitagliano, *Biophysical Journal*, 2008, **95**, 1965-1973.
44. M. S. Miettinen, L. Monticelli, P. Nedumpully-Govindan, V. Knecht and Z. Ignatova, *Biophysical journal*, 2014, **106**, 1721-1728.
45. K. A. Beauchamp, Y.-S. Lin, R. Das and V. S. Pande, *Journal of Chemical Theory and Computation*, 2012, **8**, 1409-1414.
46. O. Rahaman, A. C. T. van Duin, W. A. Goddard and D. J. Doren, *The Journal of Physical Chemistry B*, 2011, **115**, 249-261.
47. T. S. Mahadevan and S. H. Garofalini, *The Journal of Physical Chemistry B*, 2007, **111**, 8919-8927.
48. T. S. Hofer, M. Hitzengerger and B. R. Randolph, *Journal of Chemical Theory and Computation*, 2012, **8**, 3586-3595.
49. C. Abrams and G. Bussi, *Entropy*, 2014, **16**, 163-199.
50. L. Wang, R. A. Friesner and B. J. Berne, *The Journal of Physical Chemistry B*, 2011, **115**, 9431-9438.
51. D. v. d. S. Mark J. Abraham, Erik Lindahl, Berk Hess, and the GROMACS development team 2018.

52. D. Marx and J. Hutter, *Ab Initio Molecular Dynamics: Basic Theory and Advanced Methods*, Cambridge University Press, Cambridge, 2009.
53. H. C. Andersen, *The Journal of Chemical Physics*, 1980, **72**, 2384-2393.
54. H. J. C. Berendsen, J. P. M. Postma, W. F. van Gunsteren, A. DiNola and J. R. Haak, *The Journal of Chemical Physics*, 1984, **81**, 3684-3690.
55. S. Nosé, *Molecular Physics*, 1984, **52**, 255-268.
56. W. G. Hoover, *Physical Review A*, 1985, **31**, 1695-1697.
57. G. Bussi, D. Donadio and M. Parrinello, *The Journal of Chemical Physics*, 2007, **126**, 014101.
58. M. Parrinello and A. Rahman, *Physical Review Letters*, 1980, **45**, 1196-1199.
59. M. Parrinello and A. Rahman, *Journal of Applied Physics*, 1981, **52**, 7182-7190.
60. G. J. Martyna, M. E. Tuckerman, D. J. Tobias and M. L. Klein, *Molecular Physics*, 1996, **87**, 1117-1157.
61. M. E. Tuckerman, J. Alejandre, R. López-Rendón, A. L. Jochim and G. J. Martyna, *Journal of Physics A: Mathematical and General*, 2006, **39**, 5629-5651.
62. A. D. MacKerell Jr., N. Banavali and N. Foloppe, *Biopolymers*, 2000, **56**, 257-265.
63. J. Wang, R. M. Wolf, J. W. Caldwell, P. A. Kollman and D. A. Case, *Journal of Computational Chemistry*, 2004, **25**, 1157-1174.
64. C. Oostenbrink, A. Villa, A. E. Mark and W. F. Van Gunsteren, *Journal of Computational Chemistry*, 2004, **25**, 1656-1676.
65. W. Damm, A. Frontera, J. Tirado-Rives and W. L. Jorgensen, *Journal of Computational Chemistry*, 1997, **18**, 1955-1970.
66. M. B. Gee, N. R. Cox, Y. Jiao, N. Benteitis, S. Weerasinghe and P. E. Smith, *Journal of Chemical Theory and Computation*, 2011, **7**, 1369-1380.
67. M. Fyta, I. Kalcher, J. Dzubiella, L. Vrbka and R. R. Netz, *The Journal of Chemical Physics*, 2010, **132**, 024911.
68. D. Horinek, S. I. Mamatkulov and R. R. Netz, *The Journal of Chemical Physics*, 2009, **130**, 124507.
69. I. S. Joung and T. E. Cheatham, 3rd, *The journal of physical chemistry. B*, 2008, **112**, 9020-9041.
70. S. Piana, K. Lindorff-Larsen and David E. Shaw, *Biophysical Journal*, 2011, **100**, L47-L49.
71. S. Rauscher, V. Gapsys, M. J. Gajda, M. Zweckstetter, B. L. de Groot and H. Grubmüller, *Journal of Chemical Theory and Computation*, 2015, **11**, 5513-5524.
72. K. T. Debiec, A. M. Gronenborn and L. T. Chong, *The Journal of Physical Chemistry B*, 2014, **118**, 6561-6569.
73. Y. Sugita, A. Mitsutake and Y. Okamoto, *Generalized-Ensemble Algorithms for Protein Folding Simulations* 2007.
74. M. E. Tuckerman, *Statistical Mechanics: Theory and Molecular Simulation*, Oxford University Press 2011.
75. Y. Sugita and Y. Okamoto, *Chemical Physics Letters*, 1999, **314**, 141-151.
76. J. A. Lemkul and D. R. Bevan, *The Journal of Physical Chemistry B*, 2010, **114**, 1652-1660.
77. S. Kumar, J. M. Rosenberg, D. Bouzida, R. H. Swendsen and P. A. Kollman, *Journal of Computational Chemistry*, 1992, **13**, 1011-1021.
78. G. Bussi, *Molecular Physics*, 2014, **112**, 379-384.
79. F. Jensen, *Introduction to Computational Chemistry*, Wiley 2007.
80. S. Brumer, *The Journal of Chemical Physics*, 1983, **79**, 4539-4544.
81. M. Thomas, M. Brehm, R. Fligg, P. Vöhringer and B. Kirchner, *Physical Chemistry Chemical Physics*, 2013, **15**, 6608-6622.

82. G. Mathias and M. D. Baer, *Journal of Chemical Theory and Computation*, 2011, **7**, 2028-2039.
83. M. Thomas, M. Brehm, O. Hollóczki, Z. Kelemen, L. Nyulászi, T. Pasinszki and B. Kirchner, *The Journal of Chemical Physics*, 2014, **141**, 024510.
84. M. Kaupp, M. Bühl and V. G. Malkin, *Calculation of NMR and EPR parameters: theory and applications*, John Wiley & Sons 2006.
85. J. R. Cheeseman, G. W. Trucks, T. A. Keith and M. J. Frisch, *The Journal of Chemical Physics*, 1996, **104**, 5497-5509.
86. F. Jensen, *Journal of Chemical Theory and Computation*, 2008, **4**, 719-727.
87. W. Kutzelnigg, U. Fleischer and M. Schindler, in *Deuterium and Shift Calculation*, Springer Berlin Heidelberg 1991, vol. 23, ch. 3, pp. 165-262.
88. R. Ditchfield, *Molecular Physics*, 1974, **27**, 789-807.
89. F. London, *J. Phys. Radium*, 1937, **8**, 397-409.
90. T. A. Keith and R. F. W. Bader, *Chemical Physics Letters*, 1992, **194**, 1-8.
91. T. A. Keith and R. F. W. Bader, *Chemical Physics Letters*, 1993, **210**, 223-231.
92. W. Kutzelnigg, *Theoretica chimica acta*, 1988, **73**, 173-200.
93. D. P. Chong, in *Recent Advances in Density Functional Methods* 1995, pp. i-xii.
94. I. G. Shenderovich, P. M. Tolstoy, N. S. Golubev, S. N. Smirnov, G. S. Denisov and H.-H. Limbach, *Journal of the American Chemical Society*, 2003, **125**, 11710-11720.
95. R. D. Hunt and L. Andrews, *FTIR spectra of the HF-2 and H2F-3 anions isolated in solid argon and neon* 1987.
96. G. Pérez-Hernández, J. González-Vázquez and L. González, *The Journal of Physical Chemistry A*, 2012, **116**, 11361-11369.
97. S. Hirata, K. Yagi, S. A. Perera, S. Yamazaki and K. Hirao, *The Journal of Chemical Physics*, 2008, **128**, 214305.
98. C. Stein, R. Oswald, P. Sebald, P. Botschwina, H. Stoll and K. A. Peterson, *Molecular Physics*, 2013, **111**, 2647-2652.
99. A. M. Panich, *Chemical Physics*, 1995, **196**, 511-519.
100. Y. Zhang and P. S. Cremer, *Current Opinion in Chemical Biology*, 2006, **10**, 658-663.
101. M. Nakano, H. Watanabe, S. M. Rothstein and S. Tanaka, *The Journal of Physical Chemistry B*, 2010, **114**, 7056-7061.
102. X. Wang, A. Vitalis, M. A. Wyczalkowski and R. V. Pappu, *Proteins: Structure, Function, and Bioinformatics*, 2006, **63**, 297-311.
103. K. Kar, C. L. Hoop, K. W. Drombosky, M. A. Baker, R. Kodali, I. Arduini, P. C. A. van der Wel, W. S. Horne and R. Wetzel, *Journal of Molecular Biology*, 2013, **425**, 1183-1197.
104. F. Liang, C. Liu and R. J. Carroll, *Journal of the American Statistical Association*, 2007, **102**, 305-320.
105. M. Cheon, I. Chang and C. K. Hall, *Proteins: Structure, Function, and Bioinformatics*, 2010, **78**, 2950-2960.

6 Academic Curriculum Vitae

Svetlana Pylaeva

1. Personal Information

Address	Wilhelminenstr. 18, 04129, Leipzig, Germany
Phone	+49 157 31879281
E-mail	Svetlana.Pylaeva@chemie.uni-halle.de
Nationality	Russia
Date of birth	February, 6 th , 1987
Place of birth	Syktyvkar, Russia
Mother tongue	Russian, Komi
Other languages	English, German

2. Professional skills

Domain of specialization	Quantum-chemical calculations; molecular dynamics simulations; <i>ab initio</i> MD; molecular spectroscopy.
Selected skills	Computer simulations (<i>ab initio</i> MD, quantum chemical calculations, classical MD), programming languages: Python.
Specialized computer software experience	CP2K, GROMACS, Gaussian09, ORCA, VMD, Maple, MatLab.

3. Education

2015 – present	PhD student, Institute of Physical Chemistry, Martin-Luther Universität Halle-Wittenberg, Germany.
2012 – 2014	Master Student, St. Petersburg State University, St. Petersburg, Russia.
2008 – 2012	Bachelor Student, St. Petersburg State University, St. Petersburg, Russia.
2004 – 2006	Bachelor Student, St. Petersburg State University, St. Petersburg, Russia.
1994 – 2004	Student, School with profound study of English language, Syktyvkar, Russia

4. Work experience

2015 – present	Scientist, Institute of Chemistry, Martin-Luther Universität Halle-Wittenberg, Germany
11.2016-01.2017	Visiting Student, KAUST Catalysis Center, King Abdullah University of Science and Technology, Saudi Arabia
2012 – 2014	NMR and MRI specialist, Center for Magnetic Resonance, St. Petersburg State University, St. Petersburg, Russia.
06.2013 – 01.2014	Master degree work, Institute of Chemistry, Martin-Luther Universität Halle-Wittenberg, Germany
04 – 05.2012	Bachelor degree work, Institute of Physics, Freie Universität Berlin,

Germany

2010 – 2014

Bachelor degree work, Master degree work, PhD degree work, St. Petersburg State University, St. Petersburg, Russia.

5. Papers

1. S. Pylaeva, C. Allolio, B. Koeppel, G.S. Denisov, H.-H. Limbach, D. Sebastiani, P.M. Tolstoy, Proton transfer in short hydrogen bonded complex caused by solvation shell fluctuations: ab initio MD and NMR/UV study of an (OHO)⁻ bonded system, *Phys. Chem. Chem. Phys.*, 2015, **17**, 4634-4644
2. M. Sigalov, S. Pylaeva, P. Tolstoy, Hydrogen Bonding in Bis-(6-amino-1,3-dimethyluracil-5-yl)-methane Derivatives: Dynamic NMR and DFT Evaluation, *JPCA*, 2016, **120**(17), 2737
3. B. Koeppel, S. Pylaeva, C. Allolio, D. Sebastiani, E. Nibbering, G.S. Denisov, H.-H. Limbach, P.M. Tolstoy, Polar solvent fluctuations drive proton transfer in hydrogen bonded complexes of carboxylic acid with pyridines: NMR, IR and ab initio MD study, *Phys. Chem. Chem. Phys.*, 2016, **19**, 1010
4. S. Pylaeva, K.L. Ivanov, M. Baldus, D. Sebastiani, H. Elgabarty, Molecular Mechanism of Overhauser Dynamic Nuclear Polarization in Insulating Solids, *J. Phys. Chem. Lett.*, 2017, **8**(10), 2137
5. S. Pylaeva, H. Elgabarty, D. Sebastiani, P.M. Tolstoy, Symmetry and dynamics of FHF⁻ anion in vacuum, in CD₂Cl₂ and in CCl₄. Ab initio MD study of fluctuating solvent–solute hydrogen and halogen bonds, *Phys. Chem. Chem. Phys.*, 2017, **38**, 26107
6. S. Pylaeva, A. Boeker, H. Elgabarty, W. Paul, and D. Sebastiani, The conformational ensemble of polyglutamine-14 chains: specific influence of solubility tail and chromophores, *ChemPhysChem*, 2018, doi:[10.1002/cphc.201800551](https://doi.org/10.1002/cphc.201800551)
7. S. Pylaeva, M. Brehm, D. Sebastiani, Salt Bridge in Aqueous Solution: Strong Structural Motifs but Weak Enthalpic Effect, *Scientific Reports*, 2018, **8**, 13626

7 Publications

List of publications I co-authored that constitute the basis of the thesis. My responsibilities and contributions are outlined for every publication.

- P1 Polar solvent fluctuations drive proton transfer in hydrogen bonded complexes of carboxylic acid with pyridines: NMR, IR and ab initio MD study.
B. Koeppel, S. Pylaeva, C. Allolio, D. Sebastiani, E. T. J. Nibbering, G. S. Denisov, H.-H. Limbach, and P. M. Tolstoy, *Physical Chemistry Chemical Physics*, 2017, **19**, 1010.

I performed calculations of NMR chemical shielding constants, analyzed data and prepared simulations related figures for the manuscript. I participated in writing of the manuscript in the part related to simulation results.

- P2 Symmetry and dynamics of FHF⁻ anion in vacuum, in CD₂Cl₂ and in CCl₄. Ab initio MD study of fluctuating solvent-solute hydrogen and halogen bonds
S. Pylaeva, H. Elgabarty, D. Sebastiani, and P. M. Tolstoy, *Physical Chemistry Chemical Physics*, 2017, **19**, 26107.

I performed AIMD simulations and calculated NMR chemical shielding constants, and performed analysis of the data. I additionally participated in writing of the manuscript.

- P3 Molecular mechanism of Overhauser Dynamic Nuclear Polarization in insulating solids
S. Pylaeva, K. L. Ivanov, M. Baldus, D. Sebastiani, and H. Elgabarty, *The Journal of Physical Chemistry Letters*, 2017, **8**, 2137.

I performed classical MD and AIMD simulations, HFCC calculations and analysis of the data. I prepared figures for the manuscript and took part in writing.

- P4 Salt bridge in aqueous solution: strong structural motifs but weak enthalpic effect
S. Pylaeva, M. Brehm, and D. Sebastiani, *Scientific Reports*, 2018, **8**, 13626.

I performed the simulations, analyzed the data and wrote major part of the manuscript.

- P5 The conformational ensemble of Polyglutamine-14 chains: specific influences of solubility tail and chromophores
S. Pylaeva, A. Böker, H. Elgabarty, W. Paul, and D. Sebastiani, *ChemPhysChem*, 2018, **19**, 2931.

I performed the HREX simulations, analyzed the data and wrote major part of the manuscript.

Polar solvent fluctuations drive proton transfer in hydrogen bonded complexes of carboxylic acid with pyridines: NMR, IR and ab initio MD study.

B. Koepe, S. Pylaeva, C. Allolio, D. Sebastiani, E. T. J. Nibbering, G. S. Denisov, H.-H. Limbach, and P. M. Tolstoy, *Physical Chemistry Chemical Physics*, 2017, **19**, 1010.

Reproduced from Ref. B. Koepe, S. A. Pylaeva, C. Allolio, D. Sebastiani, E. T. J. Nibbering, G. S. Denisov, H.-H. Limbach and P. M. Tolstoy, *Phys. Chem. Chem. Phys.*, 2017, 19, 1010 with permission from the PCCP Owner Societies

DOI: 10.1039/C6CP06677A



Cite this: *Phys. Chem. Chem. Phys.*,
2017, **19**, 1010

Polar solvent fluctuations drive proton transfer in hydrogen bonded complexes of carboxylic acid with pyridines: NMR, IR and *ab initio* MD study†

B. Koepe,^a S. A. Pylaeva,^b C. Allolio,^b D. Sebastiani,^{*b} E. T. J. Nibbering,^{*c}
G. S. Denisov,^d H.-H. Limbach^e and P. M. Tolstoy^{*f}

We study a series of intermolecular hydrogen-bonded 1:1 complexes formed by chloroacetic acid with 19 substituted pyridines and one aliphatic amine dissolved in CD₂Cl₂ at low temperature by ¹H and ¹³C NMR and FTIR spectroscopy. The hydrogen bond geometries in these complexes vary from molecular (O–H...N) to zwitterionic (O[–]...H–N⁺) ones, while NMR spectra show the formation of short strong hydrogen bonds in intermediate cases. Analysis of C=O stretching and asymmetric CO₂[–] stretching bands in FTIR spectra reveal the presence of proton tautomerism. On the basis of these data, we construct the overall proton transfer pathway. In addition to that, we also study by use of *ab initio* molecular dynamics the complex formed by chloroacetic acid with 2-methylpyridine, surrounded by 71 CD₂Cl₂ molecules, revealing a dual-maximum distribution of hydrogen bond geometries in solution. The analysis of the calculated trajectory shows that the proton jumps between molecular and zwitterionic forms are indeed driven by dipole–dipole solvent–solute interactions, but the primary cause of the jumps is the formation/breaking of weak CH...O bonds from solvent molecules to oxygen atoms of the carboxylate group.

Received 28th September 2016,
Accepted 2nd December 2016

DOI: 10.1039/c6cp06677a

www.rsc.org/pccp

1. Introduction

Proton tautomerism in hydrogen bonds (H-bonds) is a well-established phenomenon and a thoroughly studied subject, notably for H-bonded systems in liquid solutions, with a significant number of publications based on optical^{1–8} and NMR spectroscopy.^{9–15}

The experimental data are often discussed in terms of a tautomeric equilibrium between two fixed states. This implies that in a series of changing external conditions or a series of homologous complexes the proton transfer pathway occurs as shown in Fig. 1a, where each row corresponds to a particular system (or a set of external conditions), characterized by a certain value of equilibrium constant *K*. Alternatively, the same information can be depicted as a series of double-well potential energy surfaces (PES) of various degrees of asymmetry for the

bridging proton motion. However, in many cases NMR has shown the formation of complexes with strong H-bonds, which are characterized by a quasi-symmetric position of the proton.^{16–18} This leads to a scheme shown in Fig. 1b, which can be characterized by a series of single-well proton potentials with the changing position of the minimum (“mesomeric” scheme, in contrast to the tautomeric one). In the gas phase, a tautomeric equilibrium between molecular and zwitterionic forms of a complex has not been observed before. Instead, in a series of works based on rotation spectra of hydrogen halide–amine complexes a “mesomeric” proton transfer pathway was shown.¹⁹ The IR spectra of the same systems embedded in noble gas cryo-matrices have indicated that upon increase of the polarizability of matrix atoms a molecular complex gradually turns into a zwitterionic one.²⁰ In recent years, attempts were made to combine tautomeric and mesomeric views into one, resulting in a model which is illustrated in Fig. 1c.^{14,15,21,22} Here, a tautomeric shift of the equilibrium is accompanied by a mesomeric change of the structures of the individual tautomers.

It also has been demonstrated that a crucial role is played by the thermal fluctuations of the solvent molecules in the proximity of the complex.^{23–25} The coupling of the bridging proton motion to the solvation shell configuration (solvent coordinate) is schematically shown in Fig. 2: at each horizontal cut (fixed solvent coordinate) the light bridging proton adjusts its position in a corresponding single-well potential. As a result, the “double-well”

^a Department of Chemistry, Humboldt-Universität zu Berlin, Germany

^b Institute of Chemistry, Martin-Luther Universität Halle-Wittenberg, Germany.
E-mail: daniel.sebastiani@chemie.uni-halle.de

^c Max Born Institut für Nichtlineare Optik und Kurzzeitspektroskopie, Berlin, Germany. E-mail: nibbering@mbi-berlin.de

^d Department of Physics, St. Petersburg State University, Russia

^e Institute of Chemistry and Biochemistry, Freie Universität Berlin, Germany

^f Center for Magnetic Resonance, St. Petersburg State University, Russia.
E-mail: peter.tolstoy@spbu.ru

† Electronic supplementary information (ESI) available. See DOI: 10.1039/c6cp06677a

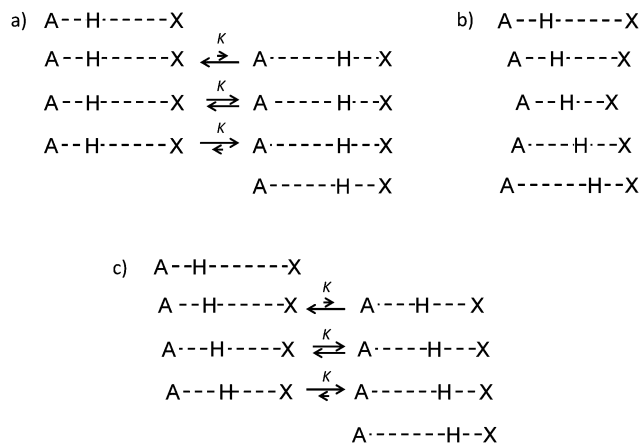


Fig. 1 Schemes of the bridging proton transfer pathways for hypothetical series of complexes with intermolecular H-bonds in solution: (a) tautomeric equilibrium; (b) continuous ("mesomeric") proton transfer and (c) combined scheme, where two-state tautomerism is combined with the continuous shift of proton positions in each individual tautomer.

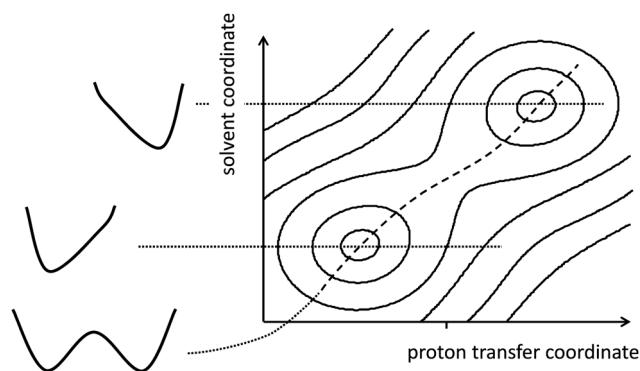


Fig. 2 Schematic representation of the proton transfer pathway for a hydrogen bonded complex in liquid solution. Proton coordinate adjusts to the solvent coordinate and the double-well potential is realized along the coordinate including solvent motion.

proton potential is realized along the combined coordinate shown as dashed line. Perhaps the most notable feature in Fig. 2 is that each tautomer is represented not by a single structure, but by an ensemble of "solvatomers", the notion which was recently confirmed by *ab initio* molecular dynamics simulations (*ab initio* MD) of an $(OHO)^-$ -bonded system.²⁴ In this approach the two-state model of tautomerism is an approximation, substituted by the whole proton distribution function.

Intermolecular OHN-bonded complexes formed by carboxylic acids and various nitrogen bases (pyridines, amines *etc.*) can be considered as one of the classical objects for H-bond research. Carboxylic acids and nitrogen bases readily form 1:1 complexes that can be quite strong^{26,27} and display a range of H-bond geometries. Previously, some of us have established several NMR hydrogen bond correlations for OHN complexes, using 1H and ^{15}N NMR chemical shifts, $^1J_{NH}$ coupling constant, carboxylic carbon ^{13}C NMR chemical shift, H/D isotope effects on all of the above-mentioned parameters as well as the value of $^{15}N-^2H$ dipole-dipole coupling constant (for complexes in solid state).^{9,17,28-32}

These correlations aimed to connect gradual changes in experimental NMR parameters with gradual changes in the average H-bond geometry expressed *via* linear combinations of interatomic distances $q_1 = 1/2(r_{OH} - r_{HN})$ and $q_2 = r_{OH} + r_{HN}$. It should be noted that q_1 and q_2 themselves are correlated, as was shown for various types of H-bonded complexes by neutron diffraction:^{33,34} shortening of the $O \cdots N$ distance (q_2 decrease) is accompanied by the symmetrization of the H-bond ($|q_1|$ decrease). While NMR hydrogen bond correlations proved to be quite useful and reliable,³⁵ the problem of possible proton tautomerism within the complex, *i.e.* $O-H \cdots N \rightleftharpoons O^- \cdots H-N^+$, was addressed in NMR studies only occasionally by us⁹ (see also early works in ref. 8, 36 and 37) and other work groups.¹² In the case of a fast proton tautomerism between the molecular and the zwitterionic forms, every experimentally observed NMR parameter becomes a weighted-average over two intrinsic values. As a result, it is often difficult to distinguish the spectral manifestations of the proton displacement in the H-bond and the shift of the tautomeric equilibrium.

In the IR spectroscopic studies the possibility of proton tautomerism in carboxylic acid/pyridine complexes has been known and explored for a long time.^{1-4,9} The IR spectral bands of individual isomers can be observed independently⁵ or as part of the overall inhomogeneously broadened band.^{6,7} However, despite widely acclaimed success in correlating some IR spectroscopic observables with the H-bond geometry (see for example correlation of ν_{OH} stretching frequency with the $O \cdots O$ distance,³⁸⁻⁴¹ or with the $O \cdots N$ distance⁴²) the underlying microscopic mechanisms for the parameter value spread in these correlation plots have remained an issue for continued research, being either of intramolecular nature or caused by surroundings effects (in particular electric fields). Ultrafast infrared 2D-IR and pump-probe spectroscopy has provided key insight into the degree of inhomogeneous broadening and spectral diffusion of disordered H-bond networks,⁴³ in particular water as a liquid⁴⁴⁻⁴⁸ and as hydrating agent,⁴⁹⁻⁵³ and of the role of anharmonic couplings of low-frequency H-bond modulation modes and of Fermi resonances of fingerprint vibrations (in particular OH or NH bending) with OH and NH stretching vibrations in medium strong H-bonds.^{54,55} Recently femtosecond IR pump-probe experiments have elucidated the ultrafast nature of the electrical fields imposed by the fluctuating polar solvent on the proton transfer coordinate of the Zundel cation $H_5O_2^+$.⁵⁶ For OHN-bonded complexes much less is established. The relative importance of the intrinsic H-bond strength and the coupling with the polar solvent has been explored for aromatic alcohol-acetonitrile complexes, where the OHN hydrogen bond can be categorized as weak, even – for 2-naphthol – in the electronic excited state.⁵⁷ For strong (short) OHN-bonded complexes other IR marker modes have been explored in a limited number of studies.^{58,59}

As mentioned above, the gradual geometric shift and tautomeric equilibrium are not mutually exclusive. By using combined NMR/UV-vis setup designed by some of us⁶⁰ we have recently demonstrated on the example of $(OHO)^-$ hydrogen bonded complexes formed by 2-chloro-4-nitrophenol and a series of

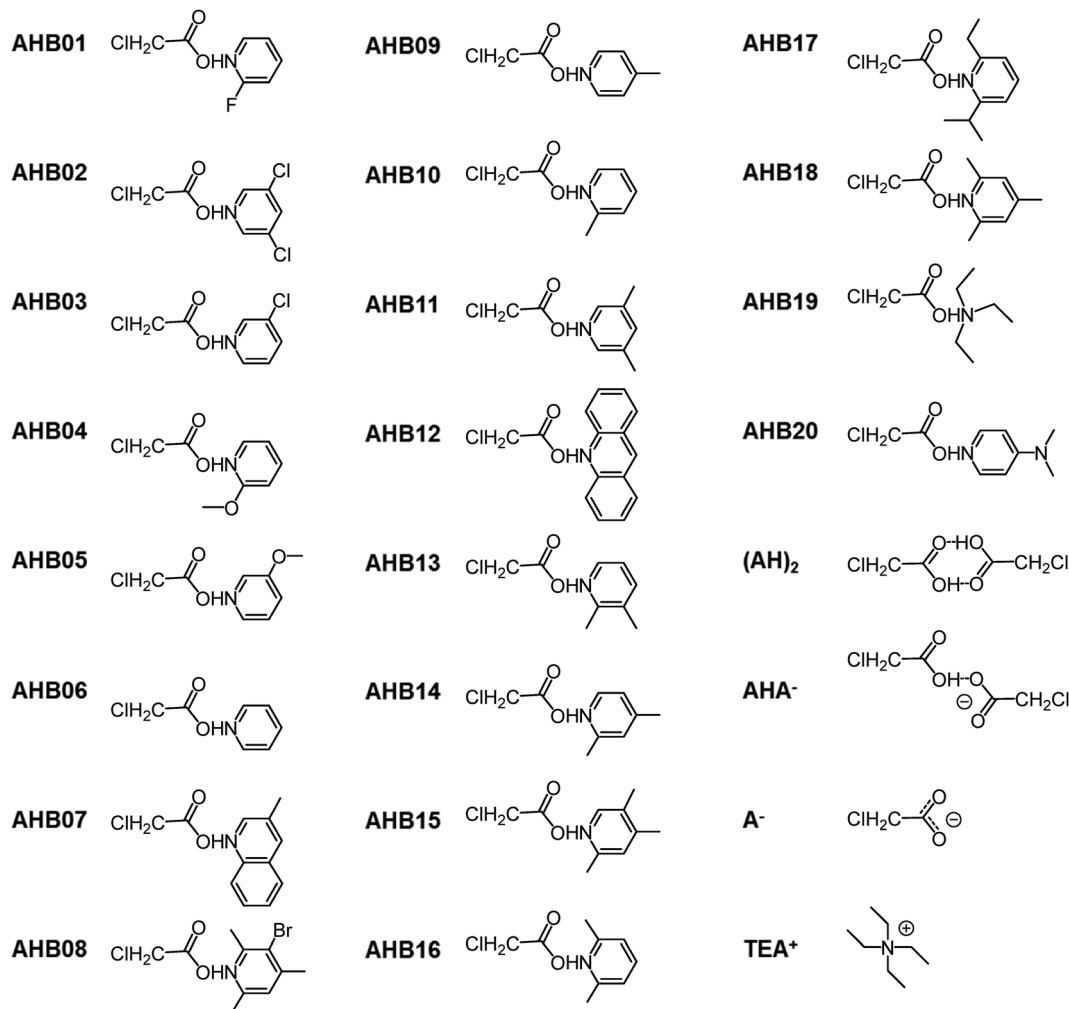


Fig. 3 Schematic representation of the complexes **AHB01–AHB20** of chloroacetic acid and N-bases studied in this work. Chloroacetic acid self-associates **(AH)₂**, **AHA⁻**, anion **A⁻** and counter-cation tetraethylammonium (**TEA⁺**) for charged complexes are shown as well. In all cases, the hydrogen bond geometries are shown formally simply as “OHN” and “OHO”, without implying a particular bridging proton position.

carboxylates that the proton transfer pathway as shown in Fig. 1c is being realized in a polar aprotic solution. The tautomerism itself, the role of the counter-cation and the role of solvent molecules' dynamics in driving the bridging proton motion have been confirmed by *ab initio* MD simulations.²⁴ While in the combined spectroscopy NMR and UV-vis spectra were recorded simultaneously and the resulting spectral information was perfectly consistent (allowing for 2D correlations plots⁶¹), it is possible to obtain NMR and optical data independently. In this work we expand this line of research into the area of OHN-bonded complexes and NMR/IR spectra.⁶² We revisit the question of the proton transfer pathway and the solvent–solute coupling on the example of intermolecular complexes of carboxylic acid and nitrogen bases dissolved in polar aprotic medium. For this study we have selected 20 complexes formed by chloroacetic acid with nitrogen bases (19 pyridines and 1 amine), as well as some self-associates of chloroacetic acid, dissolved in CD₂Cl₂ (CH₂Cl₂) at 170–300 K.

All studied complexes are depicted in Fig. 3 and labeled **AHB01–AHB20** for OHN-bonded complexes, **(AH)₂**, **AHA⁻** and **A⁻**

for the cyclic dimer, the homo-conjugated anion and the anion of chloroacetic acid, respectively. The counter-cation used for anionic systems was tetraethylammonium, labeled **TEA⁺** in Fig. 3. As one of our goals is to determine the H-bond geometries, in Fig. 3 we avoid showing the proton position. As main spectroscopic observables we have selected ¹H and ¹³C NMR chemical shifts, as well as frequencies of ¹²C=O and ¹³C=O stretching bands in IR spectra. Carbonyl stretching vibrations are often used as marker modes for H-bonded complexes of carboxylic acids, because such bands are intensive and are located in the frequency range relatively free from other strong contributions.⁶³ Ring modes of pyridines and OH stretching modes of the acid appeared to be less informative and will be mentioned only briefly in the text. Changing the base in the series **AHB01–AHB20** served as a way to change the geometry of the system (and/or equilibrium constant of the tautomerism), while changing the temperature served as a way to change the properties of the solvation shell and *via* this the structure of the complex as well. The interaction of the polar aprotic medium with a system exhibiting high atomic polarizability and potentially large dipole

moment is expected to be substantial. In order to look at the system in atomistic detail we have chosen one of the complexes, namely, the complex of chloroacetic acid with 2-methylpyridine (**AHB10**), and have studied it with *ab initio* MD. This method allowed us to investigate H-bond dynamics and also to study weak specific solvent–solute interactions.

The main questions which we address in this paper are as follows. Which of the proton transfer pathways shown in Fig. 1 applies to the studied systems? How well does the two-state model represent the situation? In case of proton tautomerism, what exactly drives the proton motion back and forth? Besides, we want to correlate the $\nu_{\text{C=O}}$ frequency of chloroacetic acid with the hydrogen bond geometry.

2. Experimental

All samples studied in this work are dichloromethane (CH_2Cl_2 or CD_2Cl_2) solutions. CH_2Cl_2 (Merck, amylene stabilized) and CD_2Cl_2 (99.8%, Deutero GmbH) were dried by molecular sieves (4 Å). 3-bromo-2,4,6-collidine was synthesized from 2,4,6-collidine by Andrey Gurinov by the procedure described in ref. 64.

All other chemicals were obtained commercially (Alfa Aesar, Aldrich) and used without further processing. Samples were obtained from dichloromethane stock solutions of acids and bases (0.2–0.5 M) using microliter pipettes.

2.1 Tetraethylammonium salts of chloroacetic acid

0.10 mL chloroacetic acid solution (0.20 M in MeOH) were mixed with 0.19 mL tetraethylammonium hydroxide (TEAOH) solution (0.10 M in methanol) and the solvent was evaporated in vacuum. The residue was dried by addition of a small amount of dry CH_2Cl_2 and subsequent vacuum evaporation (repeated twice). Finally, the residue was taken up in 0.5 mL of CH_2Cl_2 (0.04 M TEA chloroacetate) and FTIR spectra of this solution were recorded before and after each addition of sub molar equivalent amounts of chloroacetic acid as 0.20 M CH_2Cl_2 solution. After cumulated addition of 0.6 and 0.8 equivalents for natural abundance and $1\text{-}^{13}\text{C}$ -labeled acids, respectively, the solution was diluted by addition of 0.5 mL CH_2Cl_2 and of the resulting solution (0.02 M TEA chloroacetate) variable temperature FTIR spectra were acquired.

2.2 Pyridine complexes of chloroacetic acid

Concentration of chloroacetic acid typically was 0.03 M. Base concentrations were equal or higher and optimized empirically starting from close to 1 : 1 ratio, using ^1H NMR spectra recorded at *ca.* 180 K as the criterion. It was found that, on the one hand, high base concentrations ensure selectivity of formation of 1 : 1 acid–base complexes in exclusion of, for example, 2 : 1 complexes, while too high excess of base led to significant broadening and upfield shifts of bridging proton NMR signal, possibly due to signal averaging with increasing amount of residual water. Optimum acid/base ratio varied between almost 1 : 4 and 1 : 1 for weak to strong bases. In case of **AHB20**, resolving the complexes' ^{13}C NMR signals required much

higher base concentration (1 : 5) than the 1 : 1 optimum for proton spectra. For FTIR isotope difference spectra of pairs of samples containing a CD_2Cl_2 solution of a pyridine derivative and either chloroacetic acid in natural isotope abundance or $1\text{-}^{13}\text{C}$ -chloroacetic acid (99%) were prepared under ^1H NMR monitoring such that acid/base ratio differed by not more than 5%.

2.3 NMR and FTIR spectroscopic experiments

Samples for the measurement of ^1H and ^{13}C NMR spectra were obtained from the same CD_2Cl_2 solutions as used for preparing the samples for FTIR. NMR spectra were recorded at about 170 K using thin wall samples tubes and a probe optimized for ^{13}C detection. Spectra were calibrated to $\delta(\text{CHDCl}_2) = 5.32$ ppm and $\delta(^{13}\text{CD}_2\text{Cl}_2) = 53.5$ ppm, respectively. FTIR spectra were recorded with a Varian 640 FTIR spectrometer equipped with a vacuum cryostat (Specac Ltd). Sample solutions were contained between CaF_2 windows (1×20 mm²) and 0.2 mm PTFE spacers, tightly pressed together by home-made sample holders, keeping losses to surrounding vacuum to a minimum. Raw absorption data was acquired against blank reference. Subtraction of temperature specific solvent spectra and compensation for residual gases (CO_2 , H_2O) was performed in subsequent processing. Isotope difference spectra were obtained from individually processed spectra; scaling was adjusted to optimum cancellation of invariant spectral components. Further data treatment is described in Results.

2.4 Computational details

We performed *ab initio* MD simulation of the solvated complex using the CP2K simulation package.⁶⁵ We chose GPW method,⁶⁶ the BLYP-D2 DFT functional^{67–69} together with a TZVP basis on all atoms with the exception of oxygen and hydrogen, for which an aug-TZV2P/TZV2P basis sets were used, respectively. The plane-wave cutoff was set to 350 Ry. We used GTH pseudopotentials for all atoms.⁷⁰ The simulations were performed in an *NVT* ensemble at 300 K using a CSV thermostat⁷¹ with a time constant of 100 fs. All hydrogen atoms were simulated as deuterium atoms, which allowed us to increase the time step to 1 fs; from now on we will refer to them as “protons” for convenience. The employed SCF convergence was 10^{-8} a.u. The molecular dynamics was done in a cubic periodic box with a side length of 20 Å. The initial geometry of the complex was optimized in gas phase using Gaussian09.⁷² Then the complex was inserted in previously equilibrated solvent box by calculating the molecular volume of the overlapping van der Waals radii of its atoms and removing the equivalent volume of DCM molecules calculated in the same way. Simulation was then performed for the complex surrounded by 71 DCM molecules for 31 ps: 26 ps were used for data sampling after 5 ps of equilibration. We used VMD⁷³ and TRAVIS⁷⁴ for trajectory analysis.

Chemical shifts were calculated in Gaussian09 at PBE0/IGLO-III^{75–78} level of theory for a set of 98 random snapshots extracted from the trajectory. All solvent molecules within 3.3 Å range from the complex were taken into account. Isotropic magnetic shieldings were referenced to tetramethylsilane

(^1H and ^{13}C) and to 2-methylpyridine (^{15}N) calculated at the same level of theory.

3. Results

Parts of NMR and IR spectra of a subset of the studied complexes, **AHB01** through **AHB20** of chloroacetic acid with pyridines (see Fig. 3) are shown in Fig. 4 and 5, respectively. The complete sets of spectra are given in Fig. S1–S10 in ESI.†

Parameters of the complete set of complexes **AHB01**–**AHB20** for the temperature *ca.* 170 K are summarized in Table 1 and for other temperatures in Table S1 of ESI.† Aiming at ordering the complexes by degree of proton transfer, we took the bases' $\text{p}K_{\text{a}}$ values as initial guideline, but made some minor changes to this order when adopting the chemical shift $\delta(\text{C}2)$ (chloromethyl carbon atom) of the chloroacetic acid moiety as the preferred criterion. This choice will be justified below.

3.1. NMR spectra

Fig. 4a shows the successive down- and up-field trends of the bridging proton chemical shifts characteristic of proton transfer through the center of the hydrogen bond. Interestingly, this coincides with the monotonic downfield shift of the C2 resonances of the chloroacetic acid moieties shown in Fig. 4c that we used to define the order of spectra. Conversely, the C1 signals in Fig. 4b follow the monotonic downfield trend of the C2 signals only within the first half of the pathway.

For further elucidation, plots of just discussed NMR parameters for the complete set of systems studied are given in Fig. 6. Fig. 6a and b show the chemical shifts of the hydrogen bonding proton *vs.* $\delta(\text{C}1)$ and $\delta(\text{C}2)$, respectively. In Fig. 6c, the $\text{p}K_{\text{a}}(\text{BH}^+)$ values of the bases in aqueous solution, taken from literature, are plotted *vs.* $\delta(\text{C}2)$. Carbon chemical shifts of the

chloroacetate anion (tetraethylammonium salt) are represented by vertical dashed lines marked "A". Dotted lines indicate possible correlated changes of spectral parameters of complexes along the proton transfer coordinate (hand drawn guides for the eye).

Considering Fig. 6a and b we note that within the initial stages of proton transfer from O to N, both $\delta(\text{C}1)$ and $\delta(\text{C}2)$ increase monotonically. While for $\delta(\text{C}2)$ this trend seems to continue within zwitterionic complexes, no further increase in $\delta(\text{C}1)$ is observed and, in fact, $\delta(\text{C}1)$ seems to even slightly decline again on the far end of the pathway.³¹ Even though statements on that region are complicated by the scarcity of experimental data on corresponding **AHB** complexes, this view seems to be confirmed by considering data of the chloroacetate anion which should constitute the limiting case of full proton transfer: while $\delta(\text{C}2)$ of tetraethylammonium chloroacetate exceeds all values found for **AHB** complexes, its $\delta(\text{C}1)$ signal falls behind all the respective data. In Fig. 6c, we find that $\delta(\text{C}2)$ displays a clear sigmoidal correlation with $\text{p}K_{\text{a}}(\text{BH}^+)$ (similar sigmoidal dependencies on $\text{p}K_{\text{a}}$ for the hydrogen bonded complexes with increasing degree of proton transfer have been previously observed for various parameters by IR and NQR, see *f.e.* ref. 80).

Finally, a comment to the open square data points in the plots of Fig. 6 corresponding to **AHB19** (the triethylamine complex) which constitutes a significant outlier both in Fig. 6b and c. Both the bridging proton chemical shift for **AHB19** of *ca.* 13.4 ppm as well as $\text{p}K_{\text{a}}(\text{B19H}^+) \approx 10.8$ seem to suggest that triethylamine is by far the strongest proton acceptor of the series much rather than **B20** (4-dimethylaminopyridine) whose complex **AHB20** shows the highest $\delta(\text{C}2)$. However, both the low proton chemical shift for **AHB19** and the high $\text{p}K_{\text{a}}$ of **B19H}^+ are probably misleading: triethylamine is the only aliphatic base of the series which leads to two considerations. Firstly, proton chemical shifts**

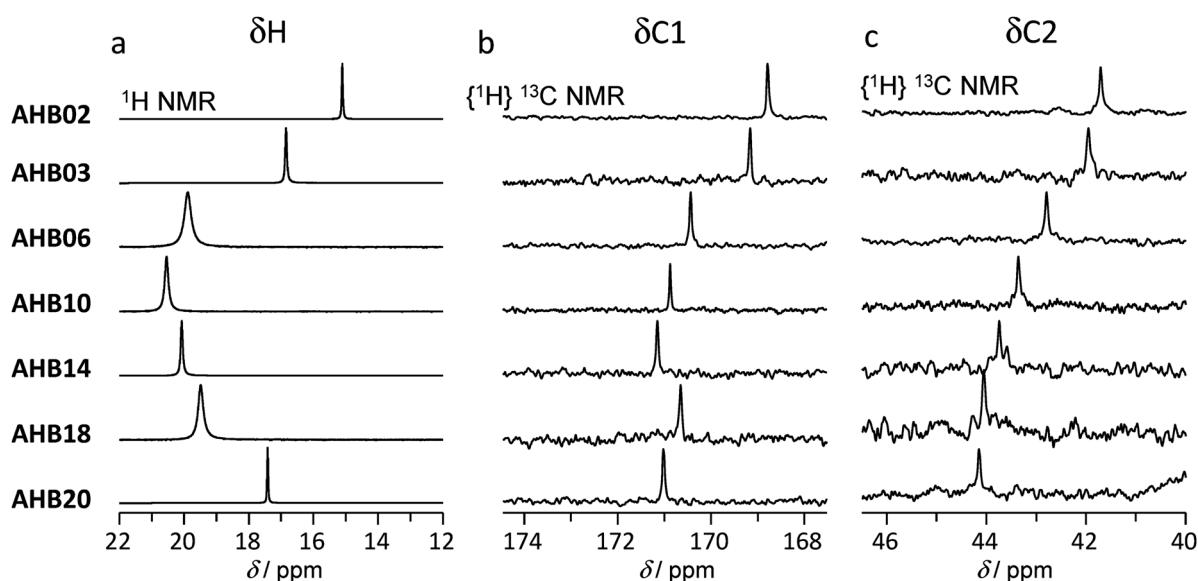


Fig. 4 Parts of ^1H and ^{13}C NMR spectra of samples, containing chloroacetic acid and various N-bases in CD_2Cl_2 solution, measured at *ca.* 170 K. Out of the complete set of complexes (**AHB01**–**AHB20**) only several have been selected as a representative subset.

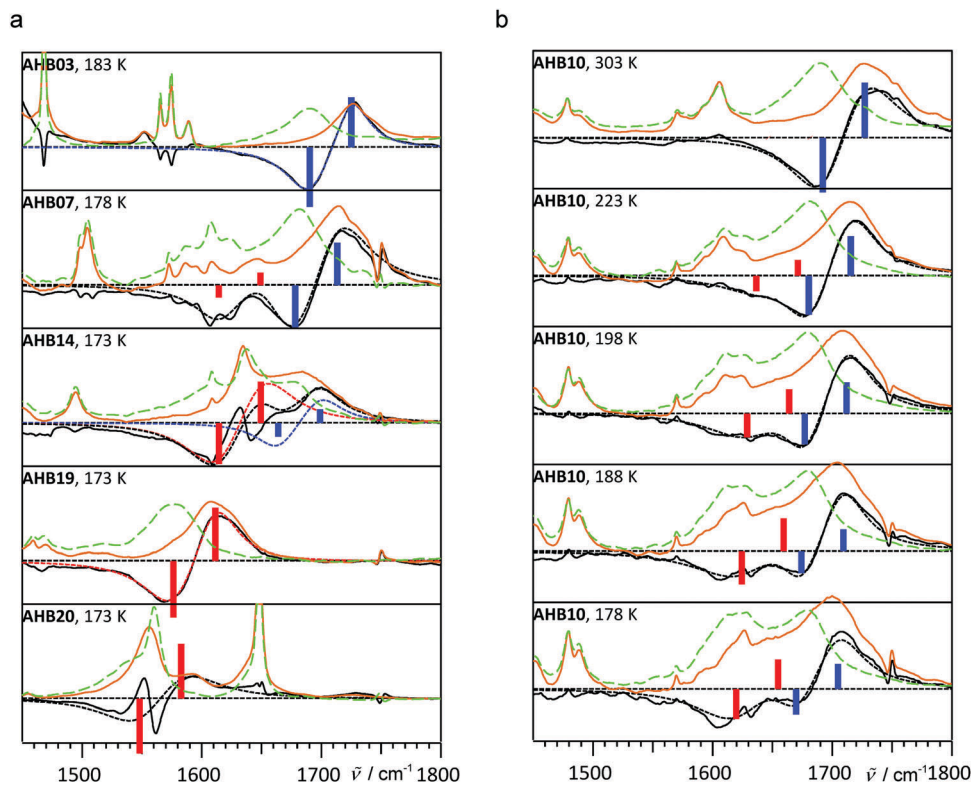


Fig. 5 Parts of IR spectra in the region of C=O stretching vibration of samples, containing chloroacetic acid and various N-bases in CH_2Cl_2 solution, measured at around 180 K (exact temperature are given in the figure) for complexes **AHB03**, **AHB07**, **AHB14**, **AHB19** and **AHB20** (a) and at various temperatures for **AHB10** complex (b). Spectra of the complexes containing ^{13}C -labelled chloroacetic acid are shown as green traces (long dashes), complexes containing non-labelled acid are shown as solid orange traces. Black solid traces correspond to the isotope difference spectra (the spectrum of ^{13}C -labelled species minus the spectrum of non-labelled species). Blue, red and black dotted traces correspond to the result of the fitting, as described in the Discussion section.

Table 1 Properties of chloroacetic acid base complexes **AHB**. Definition of bases **B01** to **B20**, $\text{p}K_{\text{a}}$ values of conjugated bases BH^+ ,⁷⁹ molar ratio $n_{\text{B}}/n_{\text{AH}}$ in NMR samples. Spectral parameters obtained at ca. 170 K in dichloromethane solution: chemical shifts δ (in ppm) of hydrogen bonding protons (H), and chloroacetic acid nuclei H2, C1, and C2. IR parameters determined at given temperatures T : vibrational frequency $\bar{\nu}$ and band width $\Delta\bar{\nu}$ (both in cm^{-1}) of the carbonyl stretching and asymmetric carboxylate stretching vibrations of the ^{12}C isotopologs of neutral and anionic acid moieties, respectively; fractional integrated intensity x_{red} of the band of the latter of the two modes

Complex	Base B	$\text{p}K_{\text{a}}(\text{BH}^+)$	$n_{\text{B}}/n_{\text{AH}}$	$\delta(\text{H})$	$\delta(\text{H}2)$	$\delta(\text{C}1)$	$\delta(\text{C}2)$	T/K	$\bar{\nu}(^{12}\text{C}=\text{O})$ ("blue")		$\bar{\nu}_{\text{as}}(^{12}\text{CO}_2^-)$ ("red")		x_{red}
									$\bar{\nu}$	$\Delta\bar{\nu}$	$\bar{\nu}$	$\Delta\bar{\nu}$	
AHB01	2-Fluoropyridine	-0.44	2.6	14.58	4.25	168.57	41.64		n.d. ^a				
AHB02	3,5-Dichloropyridine	0.71	3.2	15.11	4.23	168.79	41.71	178	1730	28 ^b			0
AHB03	3-Chloropyridine	2.81	3.5	16.85	4.22	169.17	41.95	183	1725	38			0
AHB04	2-Methoxypyridine	3.28	2.0	16.79	4.22	169.09	42.07		n.d.				
AHB05	3-Methoxypyridine	4.78	2.4	19.34	4.19	170.12	42.59	178	1719	47			0
AHB06	Pyridine	5.23	1.4	19.88	4.18	170.44	42.79	188	1717	49	1645	62	0.13
AHB07	3-Methylquinoline	5.7	1.3	20.36	4.25	171.08	42.89	178	1713	66	1649	50	0.23
AHB08	3-Bromo-2,4,6-collidine	4.96	2.7	19.80	4.14	170.13	43.10		n.d.				
AHB09	4-Picoline	5.99	1.0	20.42	4.14	170.95	43.27	188	1708	46	1651	74	0.59
AHB10	2-Picoline	6.00	1.3	20.54	4.14	170.88	43.35	178	1705	53	1655	81	0.54
AHB11	3,5-Lutidine	6.15	1.2	20.47	4.13	171.08	43.37		n.d.				
AHB12	Acridine	5.58	1.4	20.77	4.32	170.73	43.42		n.d.				
AHB13	2,3-Lutidine	6.57	1.1	20.38	4.12	171.08	43.68	173	1699	47	1645	74	0.77
AHB14	2,4-Lutidine	6.63	1.1	20.07	4.11	171.15	43.74	173	1699	46	1650	65	0.75
AHB15	2,3,5-Collidine	6.53	1.1	19.84	4.11	171.19	43.85	183	1696	33	1640	79	0.90
AHB16	2,6-Lutidine	6.65	1.0	20.19	4.10	170.65	43.87	188	1684	80	1634	80	0.75
AHB17	2-Ethyl-6-isopropyl-pyr.		1.3	20.03	4.11	170.71	43.92	178	1670	80	1624	80	0.71
AHB18	2,4,6-Collidine	7.43	1.0	19.49	4.07	170.65	44.05	173	1746	80	1617	80	1
AHB19	Triethylamine	10.75	1.0	13.36	3.97	170.79	44.07	173	—	—	1612	47 ^b	1
AHB20	4-(Dimethylamino)-pyr.	9.60	1.0	17.42	4.06	171.02	44.15	173			1583	75	1

^a n.d. – not determined. ^b Widths of bands of ^{13}C isotopologs of **AHB03** and **AHB19** were 49 and 60 cm^{-1} , while isotope shifts were 38 and 34 cm^{-1} respectively. In other cases, equal isotope shifts of 35 cm^{-1} were assumed in the fitting procedure of difference spectra.

of its complexes are likely not directly comparable to those of pyridines (just like aliphatic alcohols need a different treatment than phenols;⁸³ this is probably connected to the deshielding effects of the π -electron systems in phenols and pyridines). Secondly, the conclusions on proton donating/accepting abilities of species in aprotic media based on pK_a values obtained in water can only be reliable by comparison within a given class of compounds.¹⁵ We note that a similar outlying of the data point was previously reported for the $\nu(\text{OD})$ stretching frequency of methanol complexes with pyridines and aliphatic amines.⁸¹

3.2. FTIR spectra

It quickly became obvious during our initial attempts at correlating frequencies of vibrational modes of the carboxylic group of **AHB** complexes to the degree of proton transfer that while the $\nu(\text{C}=\text{O})$ bands seemed to display a rather clear monotonic downshift between **AHB01** and **AHB10** (see full set of IR spectra in ESI,† Fig. S4–S10), corresponding spectral contributions become very broad and increasingly obscured by other transitions in later stages of the proton transfer making a quantitative analysis rather difficult. Conversely, $\nu_{\text{as}}(\text{CO}_2^-)$ may quite readily be assigned in case of **AHB19** only and is broad and obscured in other zwitterionic species. Similar problems as those just described for the 1800 to 1600 cm^{-1} spectral region preclude straightforward analysis of the region between 1400 and 1350 cm^{-1} region where $\nu(\text{C}-\text{O})$ and $\nu_{\text{sym}}(\text{CO}_2^-)$ are located.⁸²

In order to overcome this difficulty in this work we have conducted a combined FTIR study of acid–base complexes **AHB** both in natural isotope abundance and of their $1\text{-}^{13}\text{C}$ isotopologues of the chloroacetic acid moieties. The analysis of isotope difference spectra in which all spectral contributions unrelated to the carboxylic group should cancel was performed revealing the desired spectral information. A subset of corresponding data is shown in Fig. 5 in which orange and green traces correspond to systems containing chloroacetic acid in natural isotope abundance and 99% $1\text{-}^{13}\text{C}$ -labelled, respectively. Black solid traces are difference spectra (the spectrum of ^{13}C -labelled species minus the spectrum of non-labelled species, *i.e.* the green trace minus the orange trace).

The spectra of **AHB03** and **AHB19** (Fig. 5a) are most readily analyzed. Major features of the difference spectra of these species are dispersion shaped and centered on about 1710 and 1590 cm^{-1} , respectively. These major features in both cases may be fitted employing pairs of positive and negative Lorentzian peaks (sums represented by dotted lines). In case of **AHB03**, these peaks, corresponding to $\nu(^{12}\text{C}=\text{O})$ and $\nu(^{13}\text{C}=\text{O})$ are located at 1725 and 1687 cm^{-1} and have widths (FWHM) of 38 and 49 cm^{-1} , respectively. The frequencies and integrated intensities of the peaks are represented by the blue vertical bars. We note that there are several sharp features in the region of 1570 cm^{-1} (probably these are the ring mode vibrations of the pyridine moiety) that do not seem to be entirely indifferent to isotope substitution and hence do not entirely cancel in the difference spectrum. For **AHB19**, we attribute the peaks in the difference spectrum at 1612 and 1578 cm^{-1} (widths 47 and 60 cm^{-1}) to $\nu_{\text{as}}(^{12}\text{CO}_2^-)$ and $\nu_{\text{as}}(^{13}\text{CO}_2^-)$, respectively, represented by red

vertical bars. We note that the isotope effects on vibrational frequencies in **AHB03** and **AHB19** are quite similar: 38 and 34 cm^{-1} , respectively.

The spectra of **AHB20** can be treated in analogy to the previous if care is taken to compensate in the fitting procedure for an additional sharp and somewhat intense dispersion shaped feature (two Lorentzian peaks of inverse sign, widths 15 cm^{-1} , offset 4 cm^{-1}) centered on 1550 cm^{-1} (the origin of this spectral feature is not clear). The dashed line in the figure represents the broad contribution only, attributable to $\tilde{\nu}_{\text{as}}(\text{CO}_2^-)$.

Lets us next address the spectrum of complex **AHB10** recorded at 178 K (Fig. 5b, bottom). The broad and complex shape of difference spectrum with maximum absolute values separated by as much as 100 cm^{-1} can hardly be treated in analogy to the previous spectra. Especially the suggestive double maximum structure of the spectrum of the ^{13}C isotopologue prompted us to try a dual band deconvolution approach on it, namely assuming coexistence of $\nu(\text{C}=\text{O})$ and $\nu_{\text{as}}(\text{CO}_2^-)$ modes. Fitting the difference spectrum consequently involves four Lorentzian peaks, two per isotope. In order to assure numerical stability of the fitting algorithm, we fixed the isotope splitting in both modes to 35 cm^{-1} and constrained widths and areas of spectral contributions of each given mode to be identical by absolute values for both isotopologues. The total four Lorentzian fit functions are represented in Fig. 5 by black dashed lines. We observe that this approach well describes the data, especially when applied to spectra of **AHB10** acquired at temperatures higher than 178 K (upper part of Fig. 5b). The same procedure was employed successfully on the spectra of **AHB07** and **AHB14** at 173–178 K (Fig. 5a) and a number of other systems at various temperatures.

Summarizing the results in Fig. 5a we observe two concurrent monotonous trends within the series of spectra: firstly, band intensity is redistributed from $\nu(\text{C}=\text{O})$ band (blue) to $\nu_{\text{as}}(\text{CO}_2^-)$ band (red), and, secondly, both bands, if present, shift to lower frequencies (red shift). Similar effects can be seen in temperature-dependent spectra for a given system, such as **AHB10**, shown in Fig. 5b: upon lowering the temperature the band intensity is redistributed from $\nu(\text{C}=\text{O})$ band to $\nu_{\text{as}}(\text{CO}_2^-)$ band, and both bands shift to lower frequencies. The significance of these findings will be further elucidated in the Discussion.

3.3. *Ab initio* molecular dynamics simulations

While the detailed description of the results of *ab initio* MD simulations will be given in the next section, here we present the general information which will facilitate future discussion. For the complex of chloroacetic acid with 2-methylpyridine (complex **AHB10**) solvated by 71 CD_2Cl_2 molecules the trajectory (last 26 ps of it, 1 fs steps) was analyzed as described in Experimental section. A typical structure of the hydrogen bonded complex is shown in Fig. 7. The solvent molecules were removed from Fig. 7 for clarity.

To examine the geometry of the H-bond of the complex we have built distributions of its key geometric parameters along the trajectory, shown in Fig. 8. In each case in Fig. 8 it is depicted which angle or dihedral angle is being plotted. The plots in Fig. 8

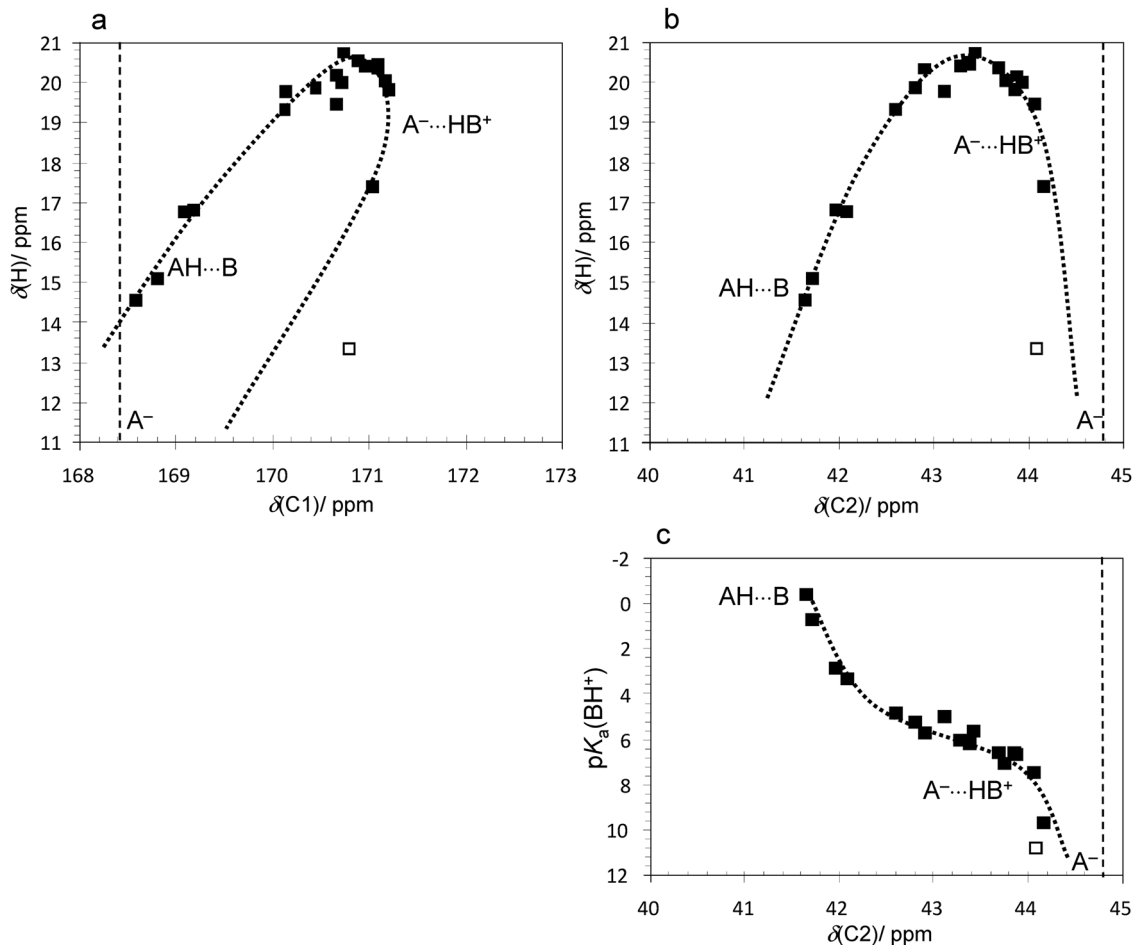


Fig. 6 Plots of NMR parameters of complexes **AHB01**–**AHB20** listed in Table 1. (a) $\delta(\text{H})$ vs. $\delta(\text{C}1)$. (b) $\delta(\text{H})$ vs. $\delta(\text{C}2)$. (c) $\text{p}K_a(\text{BH}^+)$ vs. $\delta(\text{C}2)$. Open square point: **AHB19** (triethylamine complex). Vertical dashed line corresponds to the chloroacetic acid anion (A^-).

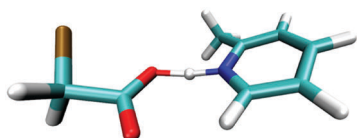


Fig. 7 The typical conformation of the **AHB10** complex according to the *ab initio* MD simulations. The solvent molecules are removed from the figure for clarity.

have been individually normalized so that abscissa numbers are not directly comparable.

During the whole course of the simulation the complex is not broken and the H-bond stays close to linear (Fig. 8a). *trans*-Configuration with respect to the mutual orientation of the “free” carbonyl group of the acid and methyl group of pyridine dominates (Fig. 8b), though there is a small peak in dihedral angle distribution at $\sim 60^\circ$ which indicates that *cis*-configuration is also present. Though the planar configuration is most probable, most of the time the instant conformation is non-planar. The H-bond of the complex is oriented along the lone pair of the nitrogen atom (Fig. 8c) and perpendicular to the line connecting two oxygen atoms of chloroacetic acid (Fig. 8d).

The position of the bridging proton in the hydrogen bond changes significantly during the simulation. In Fig. 9 we show the time dependence of the proton position measured as the linear combination of interatomic distances $q_1 = 1/2 (r_{\text{OH}} - r_{\text{HN}})$. The proton crosses the hydrogen bond center several times, effectively interconverting molecular $\text{O}-\text{H}\cdots\text{N}$ ($q_1 < 0$), and zwitterionic $\text{O}^-\cdots\text{H}-\text{N}^+$ ($q_1 > 0$) structures.

4. Discussion

4.1. NMR spectra

While the chemical shift of the bridging proton certainly is one of the most prominent NMR parameters in the characterization of hydrogen bonds, its employment suffers from some drawbacks. One of these drawbacks, encountered particularly in studies of short hydrogen bonds, is that proton chemical shift passes a maximum when bridging proton crosses the H-bond center⁸³ and as a result it is sometimes hard to determine on which side of the H-bond center the proton resides. Several NMR parameters have been considered and employed to help to answer this question. For complexes of pyridines, the chemical

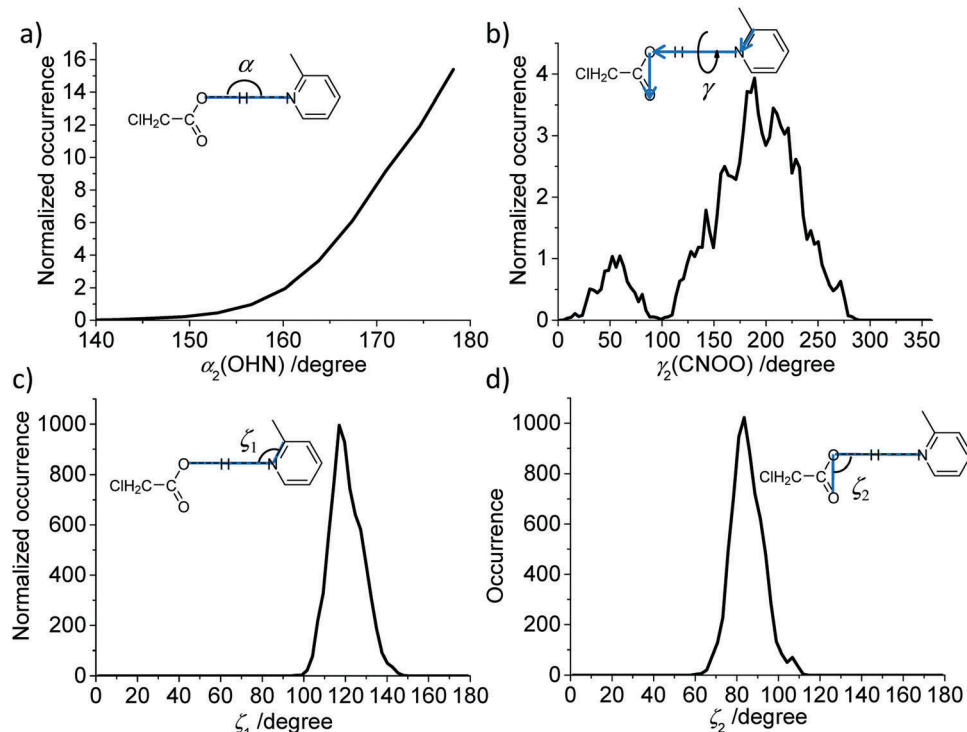


Fig. 8 The key geometrical parameters (exact definitions are given graphically for each plot) of the **AHB10** complex along the *ab initio* MD trajectory. (a) The OHN angle α which describes the linearity of the hydrogen bond; (b) the CNOO dihedral angle γ which describes the co-planarity of the pyridine ring and the COO group; (c) the CNO angle ζ_1 which describes how well the lone pair of the nitrogen atom points towards the oxygen atom involved in the hydrogen bond; (d) the NOO angle ζ_2 which describes the mutual orientation of the COO and pyridine moieties.

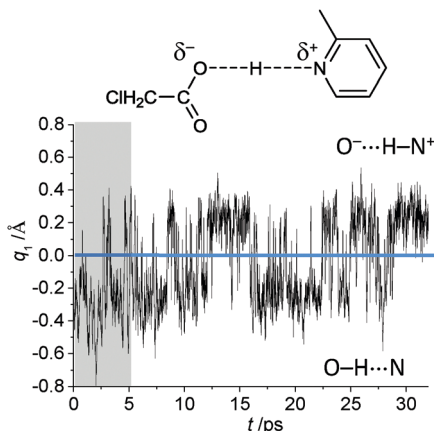


Fig. 9 Time evolution of the bridging proton position in the complex of chloroacetic acid with 2-methylpyridine (**AHB10**) according to *ab initio* MD simulation. Proton position is measured as $q_1 = 1/2(r_{\text{OH}} - r_{\text{HN}})$.

shift of ^{15}N ,³⁵ H/D isotope effect on it,²⁹ $^1J_{\text{NH}}$ coupling constant^{18b} and N-H dipole-dipole coupling⁹ have been previously used. The sign of the primary H/D isotope effect has been proposed as a criterion to distinguish between symmetric and asymmetric proton positions in the bridge.¹⁶ For hydrogen bonded complexes involving carboxylic acids, the chemical shift of carboxylic carbon $\delta(\text{C1})$ and secondary H/D isotope effects on that parameter have been exploited with some success.^{31,84}

Here, on the example of **AHB01–AHB20** complexes we show that $\delta(\text{C2})$ correlates well with the bridging proton chemical shift $\delta(\text{H})$ (Fig. 6b) and also it correlates in a sigmoidal fashion with $\text{p}K_{\text{a}}(\text{BH}^+)$ of the base (Fig. 6c). We conclude that $\delta(\text{C2})$ is a valuable parameter in the characterization of hydrogen bonds of this carboxylic acid. Despite the rather remote location of the C2 nucleus with respect to the hydrogen bond, $\delta(\text{C2})$ offers a monotonous correlation to the degree of proton transfer and in this respect may be regarded superior to $\delta(\text{C1})$. This means that the dotted curve in Fig. 6b represents in a way the proton transfer pathway (*i.e.* along this curve the proton transfer coordinate changes monotonously). The $\delta(\text{H})$ vs. $\delta(\text{C2})$ correlation can be affected – and is indeed affected, as will become clear after analyzing IR spectra – by the presence of the tautomeric equilibria between molecular and zwitterionic forms of the complexes. Similar effect has been previously observed for $\delta(^{15}\text{N})$ vs. $\delta(\text{H})$ correlation for pyridine–acid complexes and it is sometimes referred to as “corner-cutting effect”,⁸⁵ which means that bridging proton chemical shift does not reach its maximal possible value.

4.2. FTIR spectra

The primary analysis of the isotope difference IR spectra performed as described in the Results section led to the set of $\nu(\text{C}=\text{O})$ and $\nu_{\text{as}}(\text{CO}_2^-)$ band positions and corresponding relative integrated intensities for **AHB01–AHB20** complexes. In other words, the dual band structure in the IR spectra was

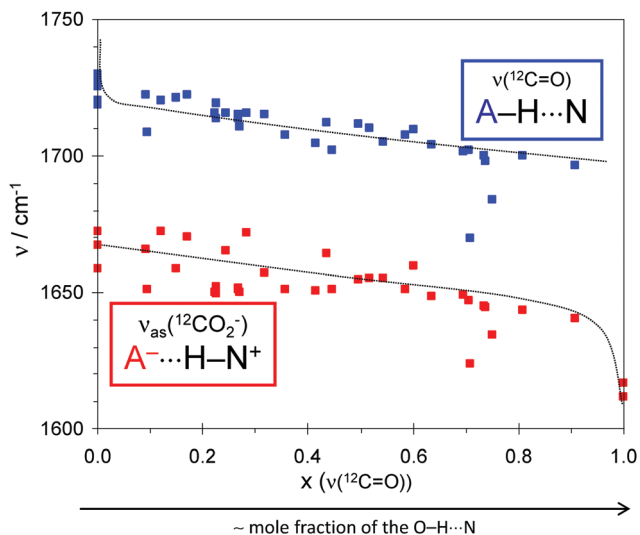


Fig. 10 The corresponding data points can be found in Table 1 and Table S1 (ESI[†]). The value x is the relative intensity of $\nu(^{12}\text{C}=\text{O})$ band defined as $x = I(\nu(^{12}\text{C}=\text{O})) / (I(\nu(^{12}\text{C}=\text{O})) + I(\nu_{\text{as}}(^{12}\text{CO}_2^-)))$, where I stands for the integrated intensity of the corresponding IR band.

taken as a direct evidence of co-existence of proton tautomers: a molecular one $\text{O}-\text{H}\cdots\text{N}$ (giving rise to $\nu(\text{C}=\text{O})$ band) and a zwitterionic one $\text{O}^-\cdots\text{H}-\text{N}^+$ (giving rise to $\nu_{\text{as}}(\text{CO}_2^-)$ band). As it was pointed out in Introduction, the two-state approach is an approximation, which does not take into account the variety of possible solvent shell configurations. We will come back to this when discussing the results of the *ab initio* MD simulation, but for the analysis of the IR spectra the two-state approximation works quite well. It was also mentioned in the Results section that with increased basicity of the base the IR band intensity is redistributed from $\nu(\text{C}=\text{O})$ band to $\nu_{\text{as}}(\text{CO}_2^-)$ band and both bands shift to lower frequencies. This is visualized in Fig. 10 where we show $\nu(^{12}\text{C}=\text{O})$ and $\nu_{\text{as}}(^{12}\text{CO}_2^-)$ band positions as a function of the relative intensity x of $\nu(^{12}\text{C}=\text{O})$ band. In other words, x is defined as $I(\nu(^{12}\text{C}=\text{O})) / (I(\nu(^{12}\text{C}=\text{O})) + I(\nu_{\text{as}}(^{12}\text{CO}_2^-)))$, where I stands for the integrated intensity of the corresponding IR band. Thus, the band position might be considered as a “spectroscopic proton transfer coordinate”, while the band intensities are proportional to the mole fractions of tautomers. We conclude that the combined proton transfer pathway similar to the one shown in Fig. 1c (and found previously for OHO^- hydrogen-bonded complexes²⁴) applies here for OHN -bonded complexes **AHB01**–**AHB20**. The two-state interpretation of IR spectra does not invalidate the interpretation of $\delta(\text{C}2)$ NMR parameter as another “spectroscopic proton transfer coordinate”. Indeed, $\delta(\text{C}2)$ averaged over two tautomers corresponds to the fictitious “average geometry” of the complex but remains monotonously dependent on the degree of proton transfer.

It is important to point out that all temperature points (Table 1 and Table S1, ESI[†]) are included into the Fig. 10 and they fall reasonably well on the same correlation line. Lowering the temperature leads to predictable and monotonous changes in the geometries of individual tautomers (measured as band positions)

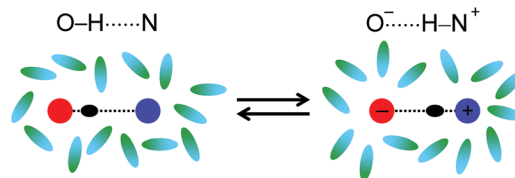


Fig. 11 Schematic representation of the solvent ordering (green-blue ovals) around molecular (left) and zwitterionic (right) forms of the OHN -bonded complex. The figure is aimed to illustrate purely “dielectric” way of describing solvent–solute interactions.

and their mole fractions (measured as relative band intensities). At this point, it is worth asking a question why the temperature affects the geometry of the complex at all? As one can safely neglect tiny changes in the populations of vibrational levels, the only remaining option is to consider the solvent–solute interactions. In our view, changes in the temperature lead to changes in the populations of various “solvatomers” (conformers of the solvation shell and the complex itself). One can look at it in two different ways, which will be described below.

One way to look at solvent–solute interactions and to roughly predict which solvatomers will be populated and which solvatomers will be depopulated upon lowering the temperature is to consider the effective polarity of the solvation shell. At lower temperatures the structures with higher ordering of the polar solvent molecules around the complex and subsequently higher dipole moment of the complex (higher degree of proton transfer; more zwitterionic nature) should be preferred. In contrast, at higher temperatures a less ordered solvation shell is more probable from the entropy point of view and as a result molecular structures of the complex with lower dipole moment should be preferred. The polarity argument (which can also be called dielectric argument) is illustrated schematically in Fig. 11.

Above, we have avoided using the term “dielectric constant of the solvent” as it is a macroscopic parameter and it should not be applied to individual molecules. However, the dielectric constant of dichloromethane rises upon temperature decrease (from 9 at room temperature to *ca.* 16 close to the freezing point⁸⁶) and technically the presence of more polarizable medium should also stabilize more polar structures. In the next section we will briefly return to this question when describing the results of DFT calculations.

Another way of looking at solvent–solute interactions is to consider specific interactions such as CH hydrogen bonding between the solvent and the solute. This will be also discussed in the next section.

4.3. *Ab initio* MD simulations

We return to the analysis of the *ab initio* MD trajectory. In Fig. 12a the correlation between two hydrogen bond coordinates, namely, $q_1 = 1/2(r_{\text{OH}} - r_{\text{HN}})$ and $q_2 = r_{\text{OH}} + r_{\text{HN}}$, is shown. This correlation has the typical parabolic shape, established previously by neutron diffraction for hydrogen bonds of various types.^{33,34} The q_1 vs. q_2 correlation shows that the shorter is the

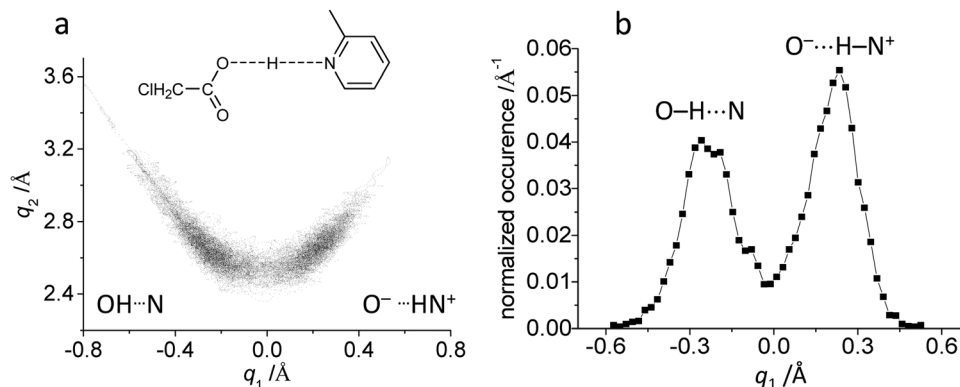


Fig. 12 Hydrogen bond geometries of **AHB10** complex, according to *ab initio* MD simulations. (a) Correlation between $q_1 = 1/2 (r_{\text{OH}} - r_{\text{HN}})$ and $q_2 = r_{\text{OH}} + r_{\text{HN}}$ geometric parameters; (b) normalized occurrence (having the meaning of the probability density) of q_1 values.

heavy atom distance, the closer is the bridging proton to the hydrogen bond center.

In Fig. 12a the density of points reflects the abundance of the structures in the simulation. Based on this, the proton position distribution (probability density or normalized occurrence) has been constructed as a function of q_1 (Fig. 12b). This distribution has two broad but clearly visible maxima, which can be associated with O-H...N ($q_1 < 0$) and O⁻...H-N⁺ ($q_1 > 0$) tautomers. The width of two peaks in Fig. 12b reflects the variety of solvatomers (and corresponding H-bond geometries) which all can be grouped into one or another “tautomer”. There is also some probability density of finding the bridging proton very close to the middle of the hydrogen bond; such structures cannot be unambiguously assigned to either tautomer. Still, the relatively good separation of two maxima in Fig. 12b justifies the two-state approach used in the analysis of IR spectra. Less pronounced dual maximum proton distribution (and thus less clear case of two-state tautomerism) has been previously found by *ab initio* MD for (OHO)⁻ hydrogen bonded complex of acetic acid with 4-nitrophenolate.²⁴

In order to describe the kinetics of proton tautomerism one has to define first what constitutes the “jump” event. The first obvious requirement is that the sign of q_1 should change. However, one should also account for possible fast oscillations around $q_1 = 0$ Å which have more to do with the proton stretching vibration than with the proton tautomerism. In order to filter out such fluctuations we have included a second requirement: before and after the jump the system has to spend a certain time τ without changing the sign of q_1 . In this way the number of jump events depends on τ . It seems physically reasonable to set τ to at least the duration of two or three proton stretching vibrational periods (*ca.* 20 fs each; keep in mind that in simulation all protons were treated as deuterons). In this approach for $\tau = 40$ fs we obtain the average residence times of O-H...N and O⁻...H-N⁺ tautomers equal to 0.62 ps and 0.76 ps, respectively, while the duration of the jump is about 20 fs. One of such jump events – a small section of the time dependence of Fig. 9 – is illustrated in Fig. 13.

The residence times obtained for other values of τ are given in Table S2 of ESI.† Taking into account the arbitrary nature of

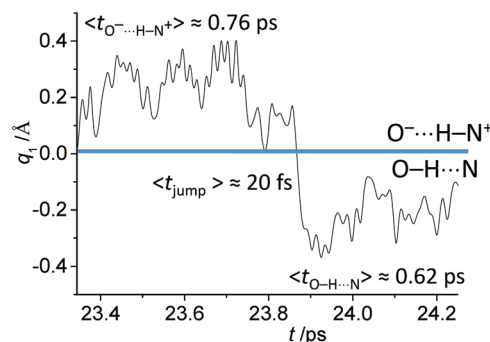


Fig. 13 Part of the *ab initio* MD trajectory for **AHB10** showing the jump of the bridging proton from O⁻...H-N⁺ to O-H...N tautomers. The average residence times ($\langle t_{\text{O-H}\cdot\cdot\text{N}} \rangle$ and $\langle t_{\text{O}^{\cdot\cdot}\text{H-N}^+} \rangle$) are estimated for $\tau = 40$ fs (for more details see text).

the definition of the jump event, it is advisable to take the exact values of the residence times with caution. However, in general the lifetimes of tautomers of about a picosecond seem to be reliable enough. For comparison, in Fig. S11 (ESI†) we plot the time dependence of q_1 where each point is averaged over 1 ps (so called window average; another way of filtering high-frequency noise), which gives us nine “jumps” for the whole trajectory. Interestingly, the estimated kinetics of proton tautomerism roughly matches the rotational diffusion times of dichloromethane, which is also in the order of a picosecond.^{87,88}

The value of the residence time of a tautomer has an implication for the interpretation of the experimental IR spectra. To assess the magnitude of inhomogeneity and the impact of solvent fluctuations on spectral diffusion, ultrafast 2D-IR experiments appear to be the method of choice to elucidate the characteristic time scales, which we anticipate to have major components in the (sub)picosecond time range. In addition to that, the rapid jump of the bridging proton between the two sites as indicated by the *ab initio* trajectory of Fig. 13 suggests a dominant role of this exchange mechanism on similar time scales. In Fig. 14 we show power spectrum of **AHB10** in the region around 1600 cm⁻¹ calculated from *ab initio* MD trajectory. Normal mode analysis⁸⁹ reveals that the selected region of the power spectrum contains only $\nu(\text{C}=\text{O})$ and $\nu_{\text{as}}(\text{CO}_2^-)$ vibrations.

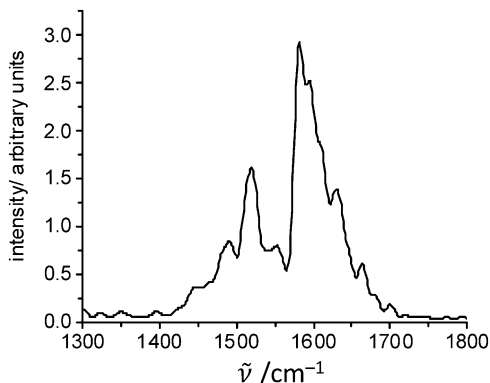


Fig. 14 Part of the power spectrum constructed from the *ab initio* MD trajectory for **AHB10** in the region of $\nu(\text{C}=\text{O})$ and $\nu_{\text{as}}(\text{CO}_2^-)$ vibrations.

One can see that the dual-band shape of the power spectrum is consistent with the existence of two tautomers and also with the dual-band feature of experimental IR spectra (though one should not compare the intensities).

Now we come to the question of the direct causes of the proton jumps. As it was mentioned above, there are different possible scenarios here, which we discuss in the following paragraphs.

Firstly, the solvent ordering might create electric fields in the region of the OHN hydrogen bond, which displace the light bridging particle due to its high atomic polarizability (because of the shallow proton stretching potential in the short strong H-bond). This in turn increases the dipole moment of the solute by proton transfer from molecular to zwitterionic form. By analyzing the *ab initio* MD trajectory and assigning point atomic charges to all atoms of the solvent molecules, we have constructed the distribution of electrostatic field components due to the solvent molecules. The electrostatic field was projected along the ON axis for two points in space: at the bridging proton position (Fig. 15a) and at the geometric center between O and N atoms (Fig. 15b), as a function of q_1 . It seems that the overall

electric field situation is almost identical for molecular ($q_1 < 0$) and zwitterionic ($q_1 > 0$) tautomers. This is remarkable, because in principle one could have expected strong electrostatic field effects in a system that can significantly change its dipole moment by proton transfer.

Another way to evaluate the electrostatic interactions between the solvent molecules and the solvated complex is to construct a parameter describing how well solvent molecules orient their individual dipole moments along the electrostatic field created by the dipole moment of the solvated complex. Following this logic, for each time step of the sampling and for all solvent molecules we have calculated the order parameter λ defined as shown in the top part of Fig. 16 (to construct the dipole moment of the complex we have assigned the charge plus one to the nitrogen atom and minus one to the oxygen atom of the OHN bridge). The correlation between λ and q_1 is shown in the bottom part of Fig. 16. The order parameter seems to be close to zero on average and one can barely discern an asymmetry in the correlation, indicating that there is no dipole-dipole solvent ordering in the solvation box as a whole.

Yet another way to treat the effect of the electrostatic field is to model the solvent as the polarizable continuum. We have performed additional DFT calculations (B3LYP/6-311++G(d,p), PCM, other details see in ESI†) of the equilibrium structures and of the potential energy curves along the proton transfer coordinate for **AHB10** at various values of the dielectric constant of the medium ϵ . The results are presented in Fig. S12 (ESI†). In short, these calculations show that in vacuum the only existing energy minimum corresponds to the O–H \cdots N structure, while upon ϵ increase the second minimum develops, corresponding to the O $^- \cdots$ H–N $^+$ structure. However, at $\epsilon = 20$ the energy barrier between two minima is only 1 kcal mole $^{-1}$, which is too low to consider individual tautomers (the zero-point vibrational level should lie higher than the top of the barrier). Interestingly enough, not the development of the second minimum but rather a smooth “mesomeric” proton transfer was previously experimentally found for Cl–H \cdots NH $_3$,

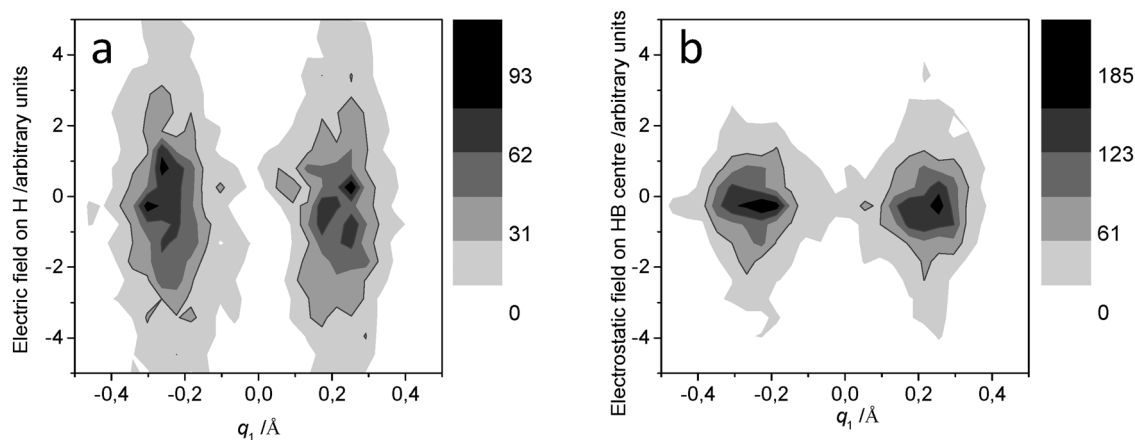


Fig. 15 Distribution of electrostatic field component along the ON axis due to solvent molecules approximated by point charges. Distribution is constructed for two points in space: at the bridging proton position (a) and at the geometric center between O and N atoms (b), as a function of q_1 . The gray-scales are given in the number of counts.

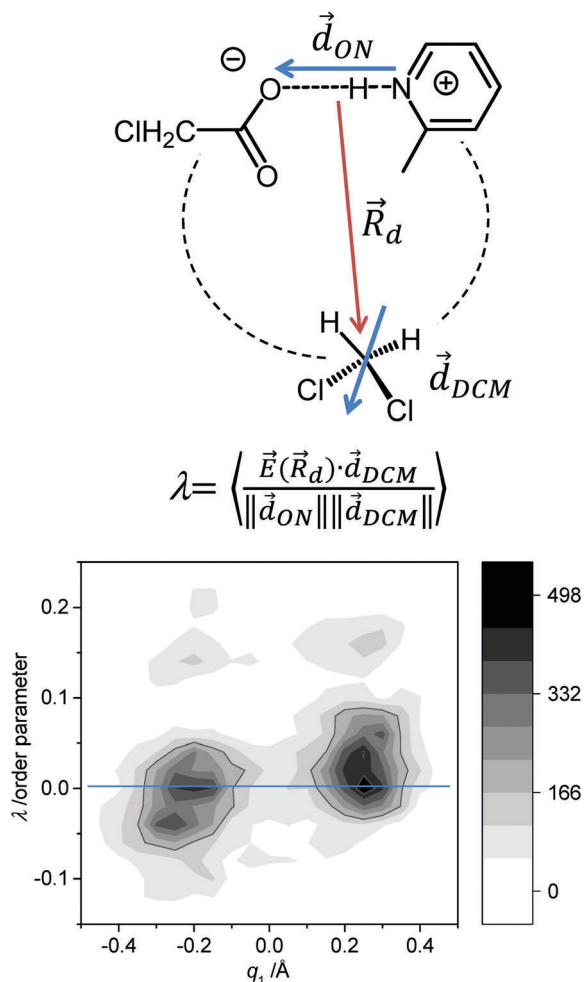


Fig. 16 The definition of the order parameter λ and the correlation between λ and q_1 constructed for all solvent molecules in the simulation box. The gray-scale is given in the number of counts.

complexes in noble gas matrices with increasing polarizability of matrix atoms.^{19,20} There are also some experimental indications that the “dielectric argument” does not describe the situation sufficiently. Additional NMR experiments (not shown) revealed that addition of a few percent of chloroform to dichloromethane samples of chloroacetic acid pyridine complexes lead to an increase of proton transfer towards the base for given temperatures. This phenomenon is hard to rationalize in terms of the dielectric continuum model: the dielectric constant of chloroform is roughly half that of dichloromethane⁹⁰ and the decrease in solvent polarity by chloroform addition should lead to a decrease in proton transfer (see *e.g.* ref. 29). However, the above observation one can understand considering solvent solute hydrogen bonding, which is discussed in the next paragraph. Such hydrogen bonding is expected to be stronger in case of chloroform, which is a stronger proton donor than dichloromethane; the significance of this will become apparent below.

Let us now consider the influence that specific interactions, such as weak CHO hydrogen bonds between the solute and the solvent, might have on the geometry of the strong hydrogen

bond in the solute complex. Previously, such H-bonds have been found for the anionic complex of acetic acid with nitrophenolate in CD_2Cl_2 .²⁴ At this point we should mention that in limiting cases some of specific solvent solute interactions might be qualified as electrostatic interactions rather than weak H-bonds. However, in this work we omit such distinction and refer to all specific CHO solvent-interactions as to hydrogen bonds, as we believe it captured their essential characteristics. In this work we have tried a number of geometric parameters of the solvation shell and show the results only for those which give better correlations with the OHN bridging proton position. In Fig. 17 we plot the correlation between r_2 distance from the oxygen atom of “free” carbonyl to dichloromethane protons and CHO angle ϕ_2 for **AHB10**, subdivided into two parts: for $q_1 < 0$ (Fig. 17a) and $q_1 > 0$ (Fig. 17b). Only those snapshots of the trajectory were included in Fig. 17, in which the q_2 parameter (see Fig. 12) was shorter than 2.8 Å, as for the longer distances the proton jumps become increasingly unlikely.

One can notice that for zwitterionic structures the solvent molecules form slightly stronger (shorter) CHO hydrogen bonds with the “free” carbonyl group. This suggests the cooperative coupling of CHO and OHN hydrogen bonds as a mechanism of proton transfer: strengthening of the CHO bond leads to a partial charge transfer and decreases the negative charge on the carboxylic group, which in turn decreases the proton accepting ability of the oxygen atom involved in the OHN bond. As a result the structure with the proton transfer is being preferentially stabilized.

A correlation similar to the one shown in Fig. 17 can be constructed for the r_1 distance from the oxygen atom of OHN bridge to dichloromethane protons and CHO angle ϕ_1 for **AHB10** (see Fig. 18). One can see that while the protons of the solvent molecules are generally further away, there is still a strengthening of the CHO hydrogen bond for zwitterionic structures.

In summary, the dielectric effects on the bridging proton position are likely to play a certain role, but the explicit calculations of the local electrostatic field of the solvent approximated by the point atomic charges along the *ab initio* MD trajectory did not reveal it. In other words, contrary to the common knowledge electric field fluctuations and dipole orientation – which is basically a PCM representation of the solvent – is only weakly correlated with the bridging proton position in the hydrogen bond. However all atom representation of the solvent is way more informative: specific solvent-solute interactions (breakage/formation of a weak hydrogen bond with the solvent) are well correlated with the OHN proton position. This is another indication that individual atoms and their positions matter a lot in a proper description of solvent solute interactions. The mechanism of proton transfer is illustrated in Fig. 19. One can also look at this in an opposite way: the proton position in the short strong OHN hydrogen bond appeared to be a sensitive indicator of the formation of weak CHO hydrogen bonds with the solvent.

In the final part of the analysis of the MD simulation we turn to the calculation of NMR parameters. For a randomly selected 98 snapshots from the trajectory we have calculated NMR chemical shifts (as described in Experimental section) for the

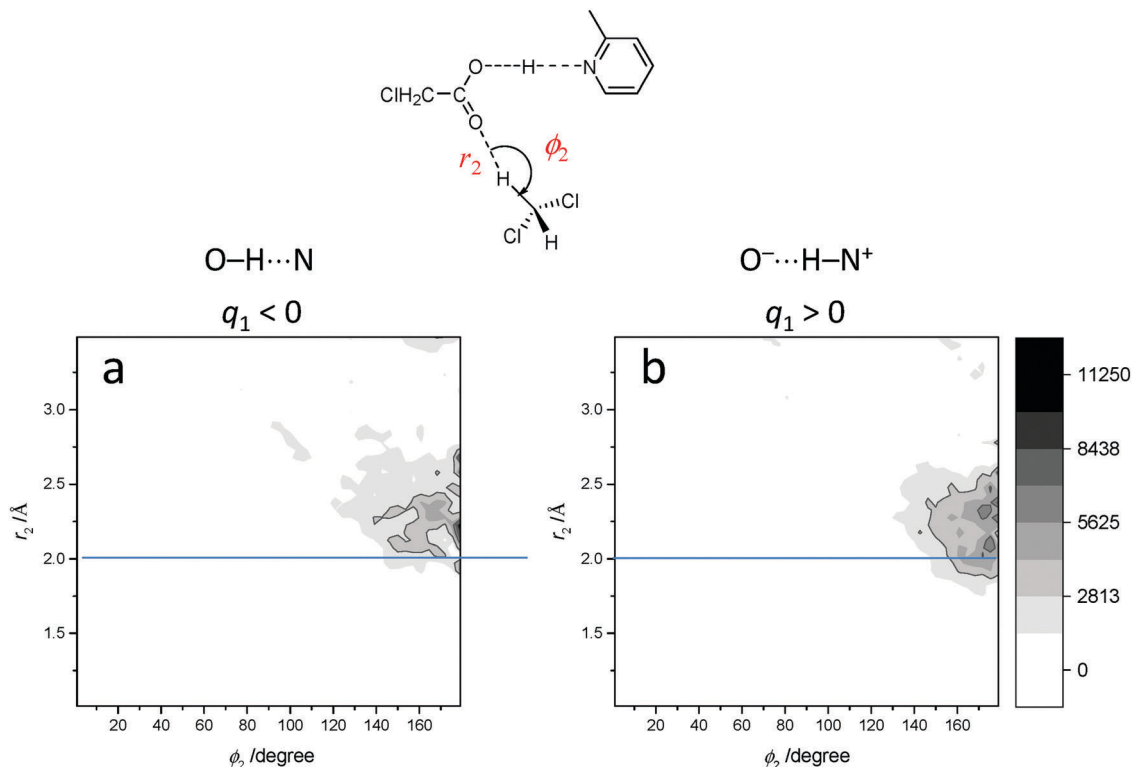


Fig. 17 Correlation between distance r_2 from the oxygen atom of “free” carbonyl to dichloromethane protons and CHO angle ϕ_2 for the *ab initio* MD trajectory for **AHB10** (with additional requirement $q_2 < 2.8 \text{ \AA}$) subdivided into two parts: for $q_1 < 0$ (a) and $q_1 > 0$ (b). Darker colours correspond to higher intensity (the scale in the right part of the figure corresponds to the occurrence, *i.e.* the number of counts).

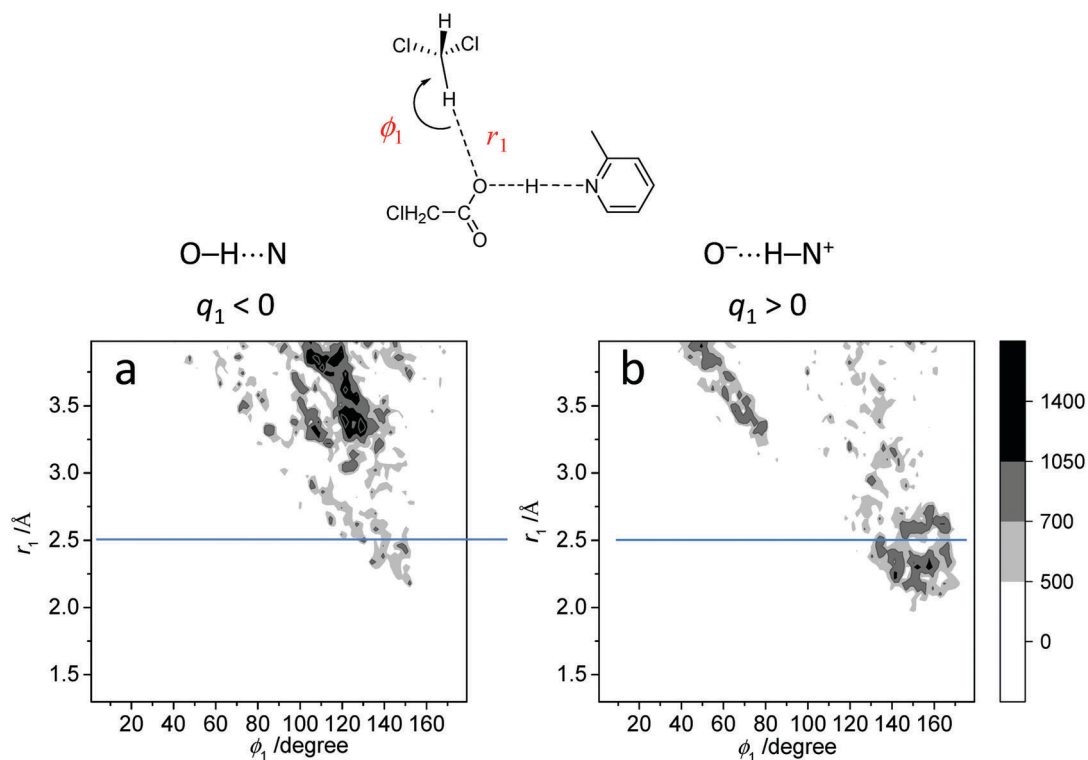


Fig. 18 Correlation between distance r_1 from the oxygen atom of OHN bridge to dichloromethane protons and CHO angle ϕ_1 for the *ab initio* MD trajectory for **AHB10** (with additional requirement $q_2 < 2.8 \text{ \AA}$) subdivided into two parts: for $q_1 < 0$ (a) and $q_1 > 0$ (b). Darker colours correspond to higher intensity (the scale in the right part of the figure corresponds to the occurrence, *i.e.* the number of counts).

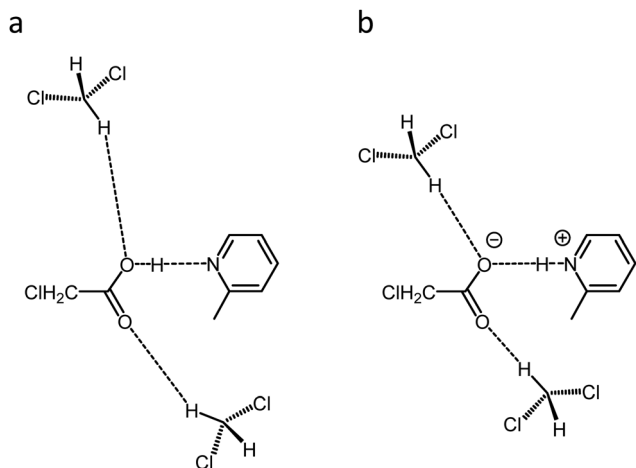


Fig. 19 Schematic representation of the $\text{O}-\text{H}\cdots\text{N}$ and $\text{O}^-\cdots\text{H}-\text{N}^+$ structures with relative positions of the solvent molecule nearest to "free" carbonyl group. (a) Molecular complex exhibiting weaker (longer) CHO hydrogen bonds with the nearest solvent molecules; (b) zwitterionic complex exhibiting stronger (shorter) CHO hydrogen bonds with the nearest solvent molecules.

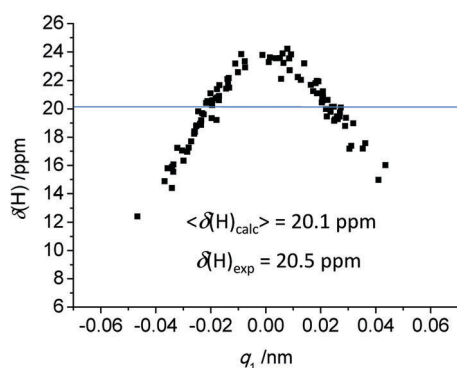


Fig. 20 Bridging proton chemical shift for **AHB10** complex, calculated for 98 random snapshots of the *ab initio* MD trajectory. The blue horizontal line corresponds to the average value. The experimental value of $\delta(\text{H})_{\text{exp}}$, measured at 178 K, is also given.

bridging proton (Fig. 20), as well as C1, C2 carbons of chloroacetic acid and nitrogen nucleus of methylpyridine (Fig. S13, ESI[†]).

The proton chemical shift shows the expected parabolic behavior and the average calculated value $\langle \delta(\text{H})_{\text{calc}} \rangle = 20.1 \text{ ppm}$ fits surprisingly well to the experimental value $\delta(\text{H})_{\text{exp}} = 20.5 \text{ ppm}$, which supports the notion that the computed trajectory represents the actual situation in the solution. The maximal value of proton chemical shift is *ca.* 24 ppm, probably due to the presence of ring currents in the pyridine ring moiety. Carbon chemical shifts are less informative, as they apparently depend on a number of variables (bond distances, angles, dihedral angles) apart of the dependence on the bridging proton position.⁹¹ Averaging over these non-essential variables starts to reveal the dependence of the H-bond geometry (see Fig. S5, ESI[†]), despite the fact that the absolute values were not scaled and numerically they are off the experimental ones. Sampling more snapshots of the trajectory would increase the quality of

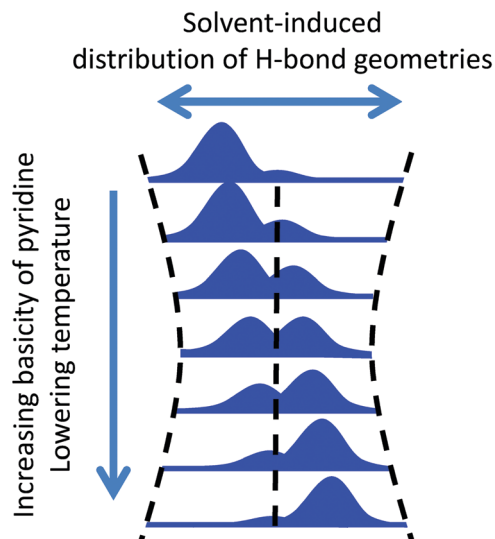


Fig. 21 Schematic representation of the overall proton transfer pathway for OHN-bonded complexes formed by chloroacetic acid with pyridines in solution in CD_2Cl_2 .

the averaging. Finally, the nitrogen chemical shifts are less scattered and show the expected high-field shift of about 130 ppm upon protonation of pyridine (Fig. S5, ESI[†]).^{9,29,85}

5. Conclusions

We have studied a series of intermolecular hydrogen-bonded 1 : 1 complexes formed by chloroacetic acid with 19 substituted pyridines and one aliphatic amine dissolved in CD_2Cl_2 at low temperature by ^1H , ^{13}C NMR and FTIR spectroscopy. The hydrogen bond geometries in these complexes vary from molecular ($\text{O}-\text{H}\cdots\text{N}$) to zwitterionic ($\text{O}^-\cdots\text{H}-\text{N}^+$) ones. The NMR spectra showed formation of short strong H-bonds in intermediate cases. For the same complexes, analysis of $\text{C}=\text{O}$ stretching and asymmetric CO_2^- stretching bands in FTIR spectra revealed presence of proton tautomerism. On the basis of these data, the overall proton transfer pathway was constructed, which is schematically shown in Fig. 21. For most of the complexes a dual-maximum distribution of hydrogen bond geometries exists in solution, and upon changing proton acceptor or temperature the positions of these two maxima change together with their relative intensities. Such proton transfer pathway is combining features of a classical "tautomeric" (Fig. 1a) and classical "mesomeric" (Fig. 1b) pathways.

The description given above is due to the solvent-solute interactions, both dielectric (dipole-dipole) and specific (weak H-bonding to the solvent). The distribution of hydrogen bond geometries in the ensemble of solvatomers and the properties of the solvation shell causing proton jumps have been investigated by *ab initio* MD simulations performed for one of the complexes, namely, a chloroacetic acid complex with 2-methylpyridine. We showed that the electric field fluctuations (PCM-like approach) is only weakly correlated with H-bond geometry. At the same time,

specific solvent–solute interactions such as strengthening/weakening of C–H···O=C hydrogen bonds between CD₂Cl₂ solvent molecules and oxygen atoms of the acid correlate with the bridging proton position in the strong OHN bond and it is likely to be one of the major causes for proton jumps (see Fig. 19). This illustrates how all atom representation of the solvent improves the overall description of the hydrogen bonded complexes in condensed phase.

Acknowledgements

NMR and IR measurements and were performed within the framework of a grant from the Deutsche Forschungsgemeinschaft (Project No. DFG – NI 492/11-1). *Ab initio* MD simulations were performed within the framework of a grant from the Deutsche Forschungsgemeinschaft Se1008/11-1. The analysis of the CHO hydrogen bonding with the solvent was performed within the framework of the RFBR grant 14-03-00111. The analysis of the OHN hydrogen bond geometry was performed within the framework of the RFBR grant 15-03-04605. We thank Dr Andrei Gurinov for the synthesis of 3-bromo-2,4,6-collidine. This work is supported by the travel grant (SP) by German-Russian Interdisciplinary Science Center (G-RISC) funded by the German Federal Foreign Office *via* the German Academic Exchange Service (DAAD).

References

- 1 C. L. Perrin, J. S. Lau and B. K. Ohta, Low-Barrier Hydrogen Bonds in Pyridine–Dichloroacetic Acid Complexes, *Pol. J. Chem.*, 2003, **77**, 1693–1703.
- 2 G. M. Barrow, The Nature of Hydrogen Bonded Ion-Pairs: The Reaction of Pyridine and Carboxylic Acids in Chloroform, *J. Am. Chem. Soc.*, 1956, **78**, 5802–5806.
- 3 G. S. Denisov, J. Starosta and V. M. Schreiber, Spectra of complexes with hydrogen bond and of ion pairs in the long-wavelength IR region (700–70 cm⁻¹). The system pyridine-acid, *Opt. Spektrosk.*, 1973, **35**, 447–452.
- 4 J. Nasielski and E. Vander Donckt, Propriétés physico-chimiques de composés à caractère aromatique—V: Etude, par spectroscopie ultraviolette, de l'interaction entre les dérivés monoazaaromatiques et les acides carboxyliques. Mise en évidence d'un potentiel à deux minimums pour le lien hydrogène, *Spectrochim. Acta*, 1963, **19**, 1989–2009.
- 5 T. Scharge, T. N. Wassermann and M. A. Suhm, Weak hydrogen bonds make a difference: Dimers of jet-cooled halogenated ethanols, *Z. Phys. Chem.*, 2008, **222**, 1407–1452.
- 6 L. O. Paulson and D. T. Anderson, High-Resolution Vibrational Spectroscopy of trans-Formic Acid in Solid Parahydrogen, *J. Phys. Chem. A*, 2009, **113**, 1770–1778.
- 7 T. Yamashita and K. Takatsuka, Hydrogen-bond assisted enormous broadening of infrared spectra of phenol-water cationic cluster: An *ab initio* mixed quantum-classical study, *J. Chem. Phys.*, 2007, **126**, 074304.
- 8 G. V. Gusakova, G. S. Denisov, A. L. Smolyansky and V. M. Schreiber, Hydrogen bond and proton transfer in carboxylic acid-amin system. Spectroscopic study of the equilibrium between the molecular complex and the ion pair, *Doklady Akad. Sci.*, 1970, **193**, 1065–1068.
- 9 N. S. Golubev, G. S. Denisov and A. I. Koltsov, Proton Spin-Spin Coupling in Complexes of Formic Acid with Proton Acceptors, *J. Mol. Struct.*, 1981, **75**, 333–337.
- 10 P. Lorente, I. G. Shenderovich, G. Buntkowsky, N. S. Golubev, G. S. Denisov and H. H. Limbach, ¹H/¹⁵N NMR chemical shielding, dipolar ¹⁵N,²H coupling and hydrogen bond geometry correlations in a novel series of hydrogen bonded acid–base complexes of collidine with carboxylic acids, *Magn. Reson. Chem.*, 2001, **39**, S18–S29.
- 11 H.-H. Limbach, G. S. Denisov, I. G. Shenderovich and P. M. Tolstoy, “Proton Tautomerism in Systems of Increasing Complexity: Examples from Organic Molecules to Enzymes” in *Tautomerism: Concepts and Applications in Science and Technology*, ed. L. Antonov, Wiley-VCH Verlag GmbH & Co. KGaA, 2016, pp. 329–372.
- 12 Z. Dega-Szafran and E. Dulewicz, ¹H NMR Studies of Solvent Effects on Hydrogen Bonding in Some Pyridine Trifluoroacetates, *Org. Magn. Reson.*, 1981, **16**, 214–219.
- 13 N. S. Golubev, S. N. Smirnov, P. M. Tolstoy, S. Sharif, M. D. Toney, G. S. Denisov and H.-H. Limbach, Observation by NMR of the tautomerism of an intramolecular OHOHN-charge relay chain in a model Schiff base, *J. Mol. Struct.*, 2007, **844**, 319–327.
- 14 B. Koeppe, P. M. Tolstoy and H.-H. Limbach, Reaction Pathways of Proton Transfer in Hydrogen Bonded Phenol-Carboxylate Complexes Explored by UVNMR, *J. Am. Chem. Soc.*, 2011, **133**, 7897–7908.
- 15 B. Koeppe, J. Guo, P. M. Tolstoy, G. S. Denisov and H.-H. Limbach, Solvent and H/D Isotope Effects on the Proton Transfer Pathways in Heteroconjugated Hydrogen-Bonded Phenol-Carboxylic Acid Anions Observed by Combined UV-vis and NMR Spectroscopy, *J. Am. Chem. Soc.*, 2013, **135**, 7553–7566.
- 16 P. Schah-Mohammed, I. G. Shenderovich, C. Detering, H.-H. Limbach, P. M. Tolstoy, S. N. Smirnov, G. S. Denisov and N. S. Golubev, Hydrogen/Deuterium Isotope Effects on NMR Chemical Shifts of Formally Symmetric Complexes with a Strong Intermolecular Hydrogen Bond in Liquid Solutions at 100–150 K, *J. Am. Chem. Soc.*, 2000, **122**, 12878–12879.
- 17 S. N. Smirnov, N. S. Golubev, G. S. Denisov, H. Benedict, P. Schah-Mohammed and H. H. Limbach, Hydrogen/Deuterium Isotope Effects on the NMR Chemical Shifts and Geometries of Intermolecular Low-Barrier Hydrogen Bonded Complexes, *J. Am. Chem. Soc.*, 1996, **118**, 4094–4101.
- 18 (a) I. G. Shenderovich, H.-H. Limbach, S. N. Smirnov, P. M. Tolstoy, G. S. Denisov and N. S. Golubev, H/D Isotope Effects on the Low-temperature NMR Parameters and Hydrogen Bond Geometries of (FH)₂F⁻ and (FH)₃F⁻ dissolved in CDF₃/CDF₂Cl, *Phys. Chem. Chem. Phys.*, 2002, **4**, 5488–5497; (b) I. G. Shenderovich, P. M. Tolstoy, N. S. Golubev, S. N. Smirnov, G. S. Denisov and H.-H. Limbach, Low-temperature

- NMR Studies of the Structure and Dynamics of a Novel Series of Acid–Base Complexes of HF with Collidine Exhibiting Scalar Couplings Across Hydrogen Bonds, *J. Am. Chem. Soc.*, 2003, **125**, 11710–11720.
- 19 A. J. Barnes and A. C. Legon, Proton transfer in amine-hydrogen halide complexes: comparison of low temperature matrices with the gas phase, *J. Mol. Struct.*, 1998, **448**, 101–106.
 - 20 L. Andrews, X. Wang and Z. Mielke, Infrared Spectrum of the H₃N–HCl Complex in Solid Ne, Ne/Ar, Ar, and Kr. Matrix Effects on a Strong Hydrogen-Bonded Complex, *J. Phys. Chem. A*, 2001, **105**, 6054–6064.
 - 21 S. Sharif, G. S. Denisov, M. D. Toney and H.-H. Limbach, NMR Studies of Coupled Low- and High-Barrier Hydrogen Bonds in Pyridoxal-5'-Phosphate Model Systems in Polar Solution, *J. Am. Chem. Soc.*, 2007, **129**, 6313–6327.
 - 22 J. Guo, P. M. Tolstoy, B. Koeppel, N. S. Golubev, G. S. Denisov, S. N. Smirnov and H.-H. Limbach, Hydrogen Bond Geometries and Proton Tautomerism of Homo-Conjugated Anions of Carboxylic Acids Studied via H/D Isotope Effects on ¹³C NMR Chemical Shifts, *J. Phys. Chem. A*, 2012, **116**, 11180–11188.
 - 23 M. Garcia-Viloca, A. Gonzalez-Lafont and J. M. Lluch, Asymmetry of the Hydrogen Bond of Hydrogen Phthalate Anion in Solution. A QM/MM Study, *J. Am. Chem. Soc.*, 1999, **121**, 9198–9207.
 - 24 S. Pylaeva, C. Allolio, B. Koeppel, G. S. Denisov, H.-H. Limbach, D. Sebastiani and P. M. Tolstoy, Proton transfer in a short hydrogen bond caused by solvation shell fluctuations: an ab initio MD and NMR/UV study of an (OHO)[−] bonded system, *Phys. Chem. Chem. Phys.*, 2015, **17**, 4634–4644.
 - 25 Y. Mori and Y. Masuda, Effect of solvent on proton location and dynamic behavior in short intramolecular hydrogen bonds studied by molecular dynamics simulations and NMR experiments, *Chem. Phys.*, 2015, **458**, 18–29.
 - 26 T. Steiner, I. Majerz and C. C. Wilson, First O–H–N Hydrogen Bond with a Centered Proton Obtained by Thermally Induced Proton Migration, *Angew. Chem., Int. Ed.*, 2001, **40**, 2651–2654.
 - 27 T. Steiner, C. C. Wilson and I. Majerz, Neutron diffraction study of a very short O–H···N hydrogen bond: crystalline adduct of 2-methylpyridine and pentachlorophenol, *Chem. Commun.*, 2000, 1231–1232.
 - 28 S. N. Smirnov, H. Benedict, N. S. Golubev, G. S. Denisov, M. M. Kreevoy, R. L. Schowen and H. H. Limbach, Exploring Zero-point Energies and Hydrogen Bond Geometries along Proton Transfer Pathways by Low-temperature NMR, *Can. J. Chem.*, 1999, **77**, 943–949.
 - 29 P. M. Tolstoy, S. N. Smirnov, I. G. Shenderovich, N. S. Golubev, G. S. Denisov and H. H. Limbach, NMR Studies of Solid State - Solvent and H/D Isotope Effects on Hydrogen Bond Geometries of 1:1 Complexes of Collidine with Carboxylic Acids, *J. Mol. Struct.*, 2004, **700**, 19–27.
 - 30 H. H. Limbach, M. Pietrzak, S. Sharif, P. M. Tolstoy, I. G. Shenderovich, S. N. Smirnov, N. S. Golubev and G. S. Denisov, NMR-Parameters and Geometries of OHN and ODN Hydrogen Bonds of Pyridine–Acid Complexes, *Chem. – Eur. J.*, 2004, **10**, 5195–5204.
 - 31 P. M. Tolstoy, J. Guo, B. Koeppel, N. S. Golubev, G. S. Denisov, S. N. Smirnov and H. H. Limbach, Geometries and Tautomerism of OHN Hydrogen Bonds in Polar Solution probed by H/D Isotope Effects on ¹³C NMR Chemical Shifts, *J. Phys. Chem. A*, 2010, **114**, 10775–10782.
 - 32 B. C. K. Ip, I. G. Shenderovich, P. M. Tolstoy, J. Frydel, G. S. Denisov, G. Buntkowsky and H. H. Limbach, NMR Studies of Solid Pentachlorophenol-4-Methylpyridine Complexes Exhibiting Strong OHN Hydrogen Bonds: Geometric H/D Isotope Effects and Hydrogen Bond Coupling Cause Isotopic Polymorphism, *J. Phys. Chem. A*, 2012, **116**, 11370–11387.
 - 33 T. J. Steiner and W. Saenger, Lengthening of the covalent O–H bond in O–H···O hydrogen bonds re-examined from low-temperature neutron diffraction data of organic compounds, *Acta Crystallogr., Sect. B: Struct. Sci.*, 1994, **50**, 348–357.
 - 34 T. Steiner, Lengthening of the Covalent X–H Bond in Heteronuclear Hydrogen Bonds Quantified from Organic and Organometallic Neutron Crystal Structures, *J. Phys. Chem. A*, 1998, **102**, 7041–7052.
 - 35 S. Sharif, E. Fogle, M. D. Toney, G. S. Denisov, I. G. Shenderovich, G. Buntkowsky, P. M. Tolstoy, M. Chan Huot and H. H. Limbach, NMR Localization of Protons in Critical Enzyme Hydrogen Bonds, *J. Am. Chem. Soc.*, 2007, **129**, 9558–9559.
 - 36 G. S. Denisov and V. M. Schreiber, Infrared Study of the Interaction of Pentachlorophenol with Secondary Amines, *Spectrosc. Lett.*, 1972, **5**, 377–384.
 - 37 G. S. Denisov and V. M. Schreiber, The Evolution of the Potential Surface of Chlorophenoles – Amines Interaction, *Doklady Akad. Sci.*, 1974, **215**, 310–313.
 - 38 E. Libowitzki, Correlation of O–H Stretching Frequencies and O–H···O Hydrogen Bond Lengths in Minerals, *Monatsh. Chem.*, 1999, **130**, 1047–1059.
 - 39 J. Emsley, Very strong hydrogen bonding, *Chem. Soc. Rev.*, 1980, **9**, 91–124.
 - 40 W. Mikenda, Stretching frequency versus bond distance correlation of O–D(H)···Y (Y = N, O, S, Se, Cl, Br, I) hydrogen bonds in solid hydrates, *J. Mol. Struct.*, 1986, **147**, 1–15.
 - 41 A. Novak, Hydrogen bonding in solids correlation of spectroscopic and crystallographic data, *Struct. Bonding*, 1974, **18**, 177–216.
 - 42 A. Lautié, F. Froment and A. Novak, Relationship between NH Stretching Frequencies and N···O Distances of Crystals Containing NH···O Hydrogen-Bonds, *Spectrosc. Lett.*, 1976, **9**, 289–299.
 - 43 E. T. J. Nibbering and T. Elsaesser, Ultrafast vibrational dynamics of hydrogen bonds in the condensed phase, *Chem. Rev.*, 2004, **104**, 1887–1914.
 - 44 C. J. Fecko, J. D. Eaves, J. J. Loparo, A. Tokmakoff and P. L. Geissler, Ultrafast hydrogen-bond dynamics in the infrared spectroscopy of water, *Science*, 2003, **301**, 1698–1702.
 - 45 J. B. Asbury, T. Steinel, C. Stromberg, S. A. Corcelli, C. P. Lawrence, J. L. Skinner and M. D. Fayer, Water dynamics: Vibrational echo correlation spectroscopy and comparison to molecular dynamics simulations, *J. Phys. Chem. A*, 2004, **108**, 1107–1119.

- 46 M. L. Cowan, B. D. Bruner, N. Huse, J. R. Dwyer, B. Chugh, E. T. J. Nibbering, T. Elsaesser and R. J. D. Miller, Ultrafast memory loss and energy redistribution in the hydrogen bond network of liquid H₂O, *Nature*, 2005, **434**, 199–202.
- 47 D. Laage and J. T. Hynes, A molecular jump mechanism of water reorientation, *Science*, 2006, **311**, 832–835.
- 48 H. J. Bakker and J. L. Skinner, Vibrational Spectroscopy as a Probe of Structure and Dynamics in Liquid Water, *Chem. Rev.*, 2010, **110**, 1498–1517.
- 49 H. J. Bakker, *Chem. Rev.*, 2008, **108**, 1456–1473.
- 50 M. Ji, M. Odellius and K. J. Gaffney, *Science*, 2010, **328**, 1003–1005.
- 51 Ł. Szyk, M. Yang, E. T. J. Nibbering and T. Elsaesser, Ultrafast Vibrational Dynamics and Local Interactions of Hydrated DNA, *Angew. Chem., Int. Ed.*, 2010, **49**, 3598–3610.
- 52 R. Costard, I. A. Heisler and T. Elsaesser, Structural Dynamics of Hydrated Phospholipid Surfaces Probed by Ultrafast 2D Spectroscopy of Phosphate Vibrations, *J. Phys. Chem. Lett.*, 2014, **5**, 506–511.
- 53 D. Laage, G. Stirnemann, F. Sterpone, R. Rey and J. T. Hynes, Reorientation and allied dynamics in water and aqueous solutions, *Annu. Rev. Phys. Chem.*, 2011, **62**, 395–416.
- 54 K. Heyne, N. Huse, J. Dreyer, E. T. J. Nibbering, T. Elsaesser and S. Mukamel, Coherent low-frequency motions of hydrogen bonded acetic acid dimers in the liquid phase, *J. Chem. Phys.*, 2004, **121**, 902–913.
- 55 N. Huse, B. D. Bruner, M. L. Cowan, J. Dreyer, E. T. J. Nibbering, R. J. D. Miller and T. Elsaesser, Anharmonic couplings underlying ultrafast vibrational dynamics of hydrogen bonds in liquids, *Phys. Rev. Lett.*, 2005, **95**, 147402.
- 56 F. Dahms, R. Costard, E. Pines, B. P. Fingerhut, E. T. J. Nibbering and T. Elsaesser, The Hydrated Excess Proton in the Zundel Cation H₅O₂(+): The Role of Ultrafast Solvent Fluctuations, *Angew. Chem., Int. Ed.*, 2016, **55**, 10600–10605.
- 57 B. T. Psciuk, M. Prémont-Schwarz, B. Koeppe, S. Keinan, D. Xiao, E. T. J. Nibbering and V. S. Batista, Correlating Photoacidity to Hydrogen-Bond Structure by Using the Local O–H Stretching Probe in Hydrogen-Bonded Complexes of Aromatic Alcohols, *J. Phys. Chem. A*, 2015, **119**, 4800–4812.
- 58 Z. Dega-Szafran and E. Dulewicz, Infrared and ¹H Nuclear Magnetic Resonance Studies of Hydrogen Bonds in Some Pyridine Trifluoroacetates and their Deuteriated Analogues in Dichloromethane, *J. Chem. Soc., Perkin Trans. 2*, 1983, 345–351.
- 59 V. Balevicius, K. Aidas, I. Svoboda and H. Fuess, Hydrogen Bonding in Pyridine N-Oxide/Acid Systems: Proton Transfer and Fine Details Revealed by FTIR, NMR, and X-ray Diffraction, *J. Phys. Chem. A*, 2012, **116**, 8753–8761.
- 60 P. M. Tolstoy, B. Koeppe, G. S. Denisov and H.-H. Limbach, Combined NMR/UV-Vis Spectroscopy in the Liquid State: Study of the Geometries of Strong OHO Hydrogen Bonds of Phenols with Carboxylic Acids, *Angew. Chem., Int. Ed.*, 2009, **48**, 5745–5747.
- 61 B. Koeppe, P. M. Tolstoy, E. T. J. Nibbering and T. Elsaesser, Two-dimensional UV-vis/NMR Correlational Spectroscopy: A Heterospectral Signal Assignment of Hydrogen-Bonded Complexes, *J. Phys. Chem. Lett.*, 2011, **2**, 1106–1110.
- 62 B. Koeppe, E. T. J. Nibbering and P. M. Tolstoy, NMR and FT-IR studies on the association of derivatives of thymidine, adenosine, and 6-N-methyl-adenosine in aprotic solvents, *Z. Phys. Chem.*, 2013, **227**, 723–749.
- 63 (a) N. V. Drichko, G. Y. Kerenskaia and V. M. Schreiber, Medium and temperature effects on the infrared spectra and structure of carboxylic acid–pyridine complexes: acetic acid, *J. Mol. Struct.*, 1999, **477**, 127–141; (b) K. Takei, R. Takahashi and T. Noguchi, Correlation between the Hydrogen-Bond Structures and the C=O Stretching Frequencies of Carboxylic Acids as Studied by Density Functional Theory Calculations: Theoretical Basis for Interpretation of Infrared bands of Carboxylic groups in Proteins, *J. Phys. Chem. B*, 2008, **112**, 6725–6731; (c) G. V. Gusakova, G. S. Denisov and A. L. Smolyansky, On ν_{CO} Frequencies in IR Spectrum of Non-Symmetrically Perturbed Carboxylate Ion, *Opt. Spectrosc.*, 1972, **32**, 922–925.
- 64 D. Heckmann, A. Meyer, B. Laufer, G. Zahn, R. Stragies and H. Kessler, Rational Design of Highly Active and Selective Ligands for the $\alpha 5\beta 1$ Integrin Receptor, *ChemBioChem*, 2008, **9**, 1397–1407.
- 65 C. Mundy, F. Mohamed, F. Schiffman, G. Tabacchi, H. Forbert, W. Kuo, J. Hutter, M. Krack, M. Iannuzzi and M. McGrath, CP2K, <http://www.cp2k.org/>, 2000.
- 66 G. Lippert, J. Hutter and M. Parrinello, A hybrid Gaussian and plane wave density functional scheme, *Mol. Phys.*, 1997, **92**, 477–487.
- 67 S. Grimme, Semiempirical GGA-type density functional constructed with a long-range dispersion correction, *J. Comput. Chem.*, 2006, **27**, 1787–1799.
- 68 A. D. Becke, Density-functional exchange-energy approximation with correct asymptotic behavior, *Phys. Rev. A: At., Mol., Opt. Phys.*, 1988, **38**, 3098–3100.
- 69 C. Lee, W. Yang and R. G. Parr, Development of the Colle-Salvetti correlation-energy formula into a functional of the electron density, *Phys. Rev. B: Condens. Matter Mater. Phys.*, 1988, **37**, 785–789.
- 70 S. Goedecker, M. Teter and J. Hutter, Separable dual-space Gaussian pseudopotentials, *Phys. Rev. B: Condens. Matter Mater. Phys.*, 1996, **54**, 1703–1710.
- 71 G. Bussi, D. Donadio and M. Parrinello, Canonical sampling through velocity rescaling, *J. Chem. Phys.*, 2007, **126**, 014101/1.
- 72 M. J. Frisch, G. W. Trucks, H. B. Schlegel, G. E. Scuseria, M. A. Robb, J. R. Cheeseman, G. Scalmani, V. Barone, B. Mennucci, G. A. Petersson, H. Nakatsuji, M. Caricato, X. Li, H. P. Hratchian, A. F. Izmaylov, J. Bloino, G. Zheng, J. L. Sonnenberg, M. Hada, M. Ehara, K. Toyota, R. Fukuda, J. Hasegawa, M. Ishida, T. Nakajima, Y. Honda, O. Kitao, H. Nakai, T. Vreven, J. A. Montgomery Jr., J. E. Peralta, F. Ogliaro, M. Bearpark, J. J. Heyd, E. Brothers, K. N. Kudin, V. N. Staroverov, R. Kobayashi, J. Normand, K. Raghavachari, A. Rendell, J. C. Burant, S. S. Iyengar, J. Tomasi, M. Cossi, N. Rega, J. M. Millam, M. Klene, J. E. Knox, J. B. Cross, V. Bakken, C. Adamo, J. Jaramillo, R. Gomperts, R. E. Stratmann, O. Yazyev, A. J. Austin, R. Cammi, C. Pomelli, J. W. Ochterski, R. L. Martin, K. Morokuma,

- V. G. Zakrzewski, G. A. Voth, P. Salvador, J. J. Dannenberg, S. Dapprich, A. D. Daniels, Ö. Farkas, J. B. Foresman, J. V. Ortiz, J. Cioslowski and D. J. Fox, *Gaussian 09, Revision A.02*, Gaussian Inc., Wallingford CT, 2009.
- 73 W. Humphrey, A. Dalke and K. Schulten, VMD: visual molecular dynamics, *J. Mol. Graphics*, 1996, **14**, 33–38.
- 74 M. Brehm and B. Kirchner, TRAVIS – A Free Analyzer and Visualizer for Monte Carlo and Molecular Dynamics Trajectories, *J. Chem. Inf. Model.*, 2011, **51**, 2007–2023.
- 75 K. L. Schuchardt, B. T. Didier, T. Elsethagen, L. Sun, V. Gurumoorthi, J. Chase, J. Li and T. L. Windus, Basis Set Exchange: A Community Database for Computational Sciences, *J. Chem. Inf. Model.*, 2007, **47**, 1045–1052.
- 76 D. Feller, The role of databases in support of computational chemistry calculations, *J. Comput. Chem.*, 1996, **17**, 1571–1586.
- 77 C. Adamo and V. Barone, Toward reliable density functional methods without adjustable parameters: The PBE0 model, *J. Chem. Phys.*, 1999, **110**, 6158–6170.
- 78 W. Kutzelnigg, U. Fleischer and M. Schindler, *Deuterium and Shift Calculation*, Springer Berlin Heidelberg, 1991, vol. 23, p. 165.
- 79 The majority of pKa values comes from the *CRC Handbook of Chemistry and Physics*, ed. D. R. Lide, CRC Press, Boca Raton, 84th edn, 2004; B2 and B20: D. D. Perrin, “*Dissociation Constants of Organic Bases in Aqueous Solution (Supplement 1972)*”, Butterworths, London, 1972 Calculated values for B7, B8, B15 were taken from ACS SciFinder.
- 80 J. Kalenik, I. Majerz, L. Sobczyk, E. Grech and M. M. M. Habeeb, ³⁵Cl Nuclear Quadrupole Resonance and Infrared Studies of Hydrogen-bonded Adducts of 2-Chloro-4-nitrobenzoic Acid, *J. Chem. Soc., Faraday Trans. 1*, 1989, **85**, 3187–3193.
- 81 M. Tamres, S. Searles, E. M. Leighly and D. W. Mohrman, Hydrogen Bond Formation with Pyridines and Aliphatic Amines, *J. Am. Chem. Soc.*, 1954, **76**, 3983–3985.
- 82 O. F. Mohammed, D. Pines, E. Pines and E. T. J. Nibbering, Aqueous bimolecular proton transfer in acid–base neutralization, *Chem. Phys.*, 2007, **341**, 240–257.
- 83 H.-H. Limbach, P. M. Tolstoy, N. Perez-Hernandez, J. Guo, I. G. Shenderovich and G. S. Denisov, OHO Hydrogen Bond Geometries and NMR Chemical Shifts: From Equilibrium Structures to Geometric H/D Isotope Effects with Applications for Water, Protonated Water and Compressed Ice, *Isr. J. Chem.*, 2009, **49**, 199–216.
- 84 P. M. Tolstoy, P. Schah-Mohammedi, S. N. Smirnov, N. S. Golubev, G. S. Denisov and H.-H. Limbach, Characterization of Fluxional Hydrogen-Bonded Complexes of Acetic Acid and Acetate by NMR: Geometries and Isotope and Solvent Effects, *J. Am. Chem. Soc.*, 2004, **126**, 5621–5634.
- 85 S. Sharif, G. S. Denisov, M. D. Toney and H. H. Limbach, NMR Studies of Solvent-Assisted Proton Transfer in a Biologically Relevant Schiff Base: Towards a Distinction of Geometric and Equilibrium H-Bond Isotope Effects, *J. Am. Chem. Soc.*, 2006, **128**, 3375–3387.
- 86 S. O. Morgan and H. H. Lowry, Dielectric polarization of some pure organic compounds in the dissolved, liquid, and solid states, *J. Phys. Chem.*, 1930, **34**, 2385–2432.
- 87 A. Hacura, Anisotropy of molecular reorientation in liquid methylene chloride, *J. Mol. Liq.*, 1992, **54**, 33–38.
- 88 J. Hunger, A. Stoppa, A. Thoman, M. Walther and R. Buchner, Broadband dielectric response of dichloromethane, *Chem. Phys. Lett.*, 2009, **471**, 85–91.
- 89 M. Thomas, M. Brehm, O. Hollóczki, Z. Kelemen, L. Nyulászi, T. Pasinszki and B. Kirchner, Simulating the vibrational spectra of ionic liquid systems: 1-ethyl-3-methylimidazolium acetate and its mixtures, *J. Chem. Phys.*, 2014, **141**, 024510.
- 90 Dielectric constant of chloroform is *ca.* 4.7 vs. that of dichloromethane 8.8 at room temperature: the values of the latter increase more strongly with decreasing temperature; for the reference see *CRC Handbook*, full reference in ref. 79.
- 91 S. Piana, D. Sebastiani, P. Carloni and M. Parrinello, Ab Initio Molecular Dynamics-Based Assignment of the Protonation State of Pepstatin A/HIV-1 Protease Cleavage Site, *J. Am. Chem. Soc.*, 2001, **123**, 8730–8737.

Symmetry and dynamics of FHF⁻ anion in vacuum, in CD₂Cl₂ and in CCl₄. Ab initio MD study of fluctuating solvent-solute hydrogen and halogen bonds
S. Pylaeva, H. Elgabarty, D. Sebastiani, and P. M. Tolstoy, *Physical Chemistry Chemical Physics*, 2017, **19**, 26107.

S. A. Pylaeva, H. Elgabarty, D. Sebastiani and P. M. Tolstoy, *Phys. Chem. Chem. Phys.*, 2017, 19, 26107 – Published by the PCCP Owner Societies

DOI: 10.1039/C7CP04493C



Cite this: *Phys. Chem. Chem. Phys.*,
2017, 19, 26107

Symmetry and dynamics of FHF[−] anion in vacuum, in CD₂Cl₂ and in CCl₄. *Ab initio* MD study of fluctuating solvent–solute hydrogen and halogen bonds†

S. A. Pylaeva,^a H. Elgabarty,^a D. Sebastiani^{id}^a and P. M. Tolstoy^{id}^{*b}

FHF[−] anion is a classic example of a central-symmetric strongly hydrogen bonded system that has been intensively investigated both experimentally and theoretically. In this paper we focus on solvent effects on symmetry, structure and dynamics of the anion. The FHF[−] anion is studied in vacuum, dissolved in CH₂Cl₂ and dissolved in CCl₄ by *ab initio* molecular dynamics simulations. We show that CH₂Cl₂ molecules form CH⋯F hydrogen bonds with lone pairs of fluorine atoms, while CCl₄ molecules form halogen bonds. These specific non-covalent solvent–solute interactions are cooperatively coupled to the FHF[−] hydrogen bonds. The fluctuation of solvent molecules' positions is the driving force changing the FHF[−] hydrogen bond geometry. Most of the time, the anion is solvated asymmetrically, which leads to the asymmetric bridging particle position, though the time-averaged *D*_{∞h} symmetry is retained. Interestingly, this transient asymmetrization of FHF[−] is more pronounced in CCl₄, than in CH₂Cl₂. We show that the ¹H and ¹⁹F NMR chemical shifts react sensitively to the changes of anion's geometry and the limiting chemical shifts of free solvated FH and F[−] are strongly solvent-dependent.

Received 4th July 2017,
Accepted 8th September 2017

DOI: 10.1039/c7cp04493c

rsc.li/pccp

Introduction

The geometric, energetic and spectroscopic properties of hydrogen bonded complexes are susceptible to the structure and dynamics of the surrounding medium. For example, in molecular crystals and in hydrophobic pockets of biomolecules steric factors and local polarity often determine the bridging proton position.^{1,2} In solutions, the thermal fluctuations of solvent dipoles in the solvation shell and specific solvent–solute interactions may significantly influence the structure of a hydrogen bonded complex.^{3–6} In particular, in the case of formally symmetric hydrogen bonds transient asymmetric solvation shell structures (which may include counterions for charged systems) may break the overall symmetry of the complex.⁴ For example, Perrin *et al.* have studied the solvent effects on the symmetry of an intramolecular (OHO)[−] hydrogen bond in case of symmetric counter cation placement⁷ and have coined the term “solvatomers”⁸ to describe conformations (sometimes true isomers) that differ in solvation. In ref. 9 authors argue that the observation of an equilibrium between two strongly hydrogen-bonded tautomers

of a formally symmetric NHN system could be due to the reorganization of the solvent, switching between two asymmetric solvation patterns. It has been proposed to detect experimentally the presence of an equilibrium by performing its isotopic perturbation (H/D or ¹⁶O/¹⁸O replacement).^{7,10,11}

Recently we have studied by a combination of *ab initio* molecular dynamics simulations (*ab initio* MD) and experimental low-temperature combined NMR/UV-Vis spectroscopy¹² strongly OHO-bonded anionic complex of 4-nitrophenolate and acetic acid dissolved in CD₂Cl₂.¹³ In this system an effective double-well proton potential is realized and the fast reversible proton transfer in the OHO bond is driven by the solvent–solute interactions. While the overall effect of solvation by a polar medium is clearly present,¹⁴ the primary driving force of proton transfer was shown to be the formation and breakage of weak CH⋯O=C hydrogen bonds between solvent molecules and the “free” carbonyl group of the acetic acid. Expanding the line of research to neutral OHN-bonded complexes, a series of complexes formed by chloroacetic acid and substituted pyridines has been studied by low-temperature combined NMR/IR spectroscopy.¹⁵ *Ab initio* MD simulations carried out for the complex of acetic acid with 2-methylpyridine dissolved in dichloromethane have revealed that the proton transfer from the molecular OH⋯N to the zwitterionic O[−]⋯HN⁺ form occurs in the pico-second time range and it is driven by the cooperative interaction of the OHN hydrogen bond and CH⋯O=C bonds with

^a Institute of Chemistry, Martin-Luther Universität Halle-Wittenberg, Germany.
E-mail: daniel.sebastiani@chemie.uni-halle.de

^b Center for Magnetic Resonance, St. Petersburg State University, Russia.
E-mail: peter.tolstoy@spbu.ru

† Electronic supplementary information (ESI) available. See DOI: 10.1039/c7cp04493c



solvent molecules. In contrast to liquid solutions, in molecular crystals with OHN hydrogen bonds, where the surrounding medium is essentially static (and stabilization of zwitterionic structures is less likely¹⁶), the proton tautomerism is often suppressed.¹⁷ For charged systems with intramolecular (NHN)⁺ hydrogen bonds the solvent and counter-anion effects have been previously studied experimentally^{18,19} and computationally.²⁰ In ref. 19 it was argued that the increase of the solvent polarity leads to the separation of the (NHN)⁺-bonded complex and its counteranion and in average results in the symmetrisation of the (NHN)⁺ bridge. The nuclear quantum effects on distribution of bridging proton position could be accounted for by using path integral molecular dynamics simulations (PIMD). Recently, this approach has been applied to short OHO,²¹ OHN²² and other hydrogen bonds, including intramolecular ones²³ and the ones found inside the active sites of enzymes.²⁴

One of the most famous examples of an extremely strong and short symmetric hydrogen bond is FHF⁻ anion. The recent estimates give the gas phase complexation energy around 44 kcal mol⁻¹.²⁵ In the gas phase the bridging proton is located at the geometric centre between two fluorines (*D*_{∞h} point group of symmetry for the anion), as confirmed by IR spectroscopy^{26–28} The experimental value of FHF⁻ vibrational frequencies are $\nu_1 = 583 \text{ cm}^{-1}$ (symmetric stretch) $\nu_2 = 1286 \text{ cm}^{-1}$ (bending) and $\nu_3 = 1331 \text{ cm}^{-1}$ (asymmetric stretch).²⁷ Deuteration of the complex results in so-called anomalous Ubbelohde effect.^{29,30} the F...F distance slightly shortens in FDF⁻, as compared to FHF⁻.²⁶ This could be rationalized in terms of a smaller spread of the deuteron's vibrational wave function, which allows two fluorines to come closer to each other.³¹ Apart of the Ubbelohde effect, the equilibrium structure of FDF⁻ anion is similar to that of FHF⁻. The symmetry of the FHF⁻ (FDF⁻) anion remains unbroken in noble gas matrices³² and in KHF₂ (KDF₂) crystals.³³ In a recent paper Grabowski² has analyzed the available crystal structures including FHF⁻ fragment and found out that while in some cases the gas-phase symmetry *D*_{∞h} is preserved, in many other cases it is deformed due to interactions with the surrounding medium, mainly by the formation of external hydrogen bonds. In a polar aprotic medium, such as a mixture of liquefied gases CDF₂/CDF₂Cl the FHF hydrogen bond in the FHF⁻NBu₄⁺ complex retains its average symmetry, as evidenced by the positive value of the primary H/D isotope effect³⁴ ($\delta D - \delta H > 0.32 \text{ ppm}$; $\delta H = 16.6 \text{ ppm}$ ³⁵). However, the situation depends on the strength of the intermolecular interactions: in the presence of a strongly interacting counter-cation, such as 2,4,6-trimethylpyridinium,³⁶ the transient symmetry of FHF⁻ is broken, though in the NMR time scale two fluorine atoms stay chemically equivalent due to the rapid rotation of the anion.

The FHF⁻ anion is a popular system for theoretical investigations. The small number of atoms allows for high-precision calculations of the multidimensional potential energy surface (PES).^{37,38} It has been demonstrated that in the gas phase the potential for the proton stretching motion is highly anharmonic and has a “flat-bed” single-well shape, which leads to the delocalization of the bridging particle near the H-bond center.

Depending on the level of theory used, the calculations of the vibrational frequencies using the multidimensional PES show some spread around the experimental values. In some cases computed frequencies match rather well – difference less than 10 cm⁻¹ – with the experiment.^{39–42} Upon increase of the F...F distance a barrier for the proton motion appears and grows, eventually rising above the zero-point energy level and creating a dual maximum shape of the proton wave function.⁴³ It could be argued that in a condensed medium such double well potential is realized along the proton transfer coordinate that includes the solvent molecule motions.⁴⁴

The NMR parameters of FHF⁻ anion have been computed by several authors.^{35,41,45} The results show the low-field bridging proton chemical shift and high values of the ¹J_{HF} and ²J_{FF} coupling constants for the isolated anion, which reproduce rather well the available experimental data. Additionally, in ref. 46 various vibrational contributions to the resulting value of the positive primary H/D isotope have been discussed and in ref. 47 the solvent-induced temperature dependencies of NMR parameters of FHF⁻ anion were analyzed. Recently published results of the gas phase path integral molecular dynamics study (MP2/6-31++G**)⁴⁸ of FHF⁻ and FDF⁻ have reproduced the main features of the anion: *D*_{∞h} symmetry, anomalous Ubbelohde effect on the F...F distance upon deuteration and the narrower distribution of *D* positions, as compared to H. It has also been reported that despite the linear configuration of three atoms in the optimized geometry of the anion the most probably structure in the gas phase is bent (more on that in Discussion).

In this work we present the results of *ab initio* MD investigation of FHF⁻ anion in three environments: in vacuum and in two explicit solvents, CH₂Cl₂ and CCl₄. Our main interest is to gain an atomistic understanding of how specific solvent–solute interactions (symmetric or not) break the transient symmetry of the anion. Here by symmetry we mean the position of the bridging proton between two fluorine atoms (*D*_{∞h} for the central position, *C*_{∞v} for the asymmetric linear position and *C*_s for asymmetric non-linear one). We aim to analyse the ensemble of solvatomers and corresponding distribution of spectroscopic parameters (NMR and IR) in condensed medium.⁴⁹ The main source of the solvent–solute interactions is expected to be the interaction of the fluorine lone pairs with the CH protons (for CH₂Cl₂) and with the sigma-holes on the halogen atoms (for CH₂Cl₂ and CCl₄). The counterion effects are not considered in this paper. Small cations such as K⁺ or Na⁺ would strongly interact with the anion, perturb the solvation shell and mask the specific solvent–solute non-covalent interactions. Large bulky counterions used in experiments (pyridinium,³⁶ tetrabutylammonium,³⁵ and even larger systems⁵⁰) are less active, but the perturbation of the solvation shell would also break the potential symmetry of the solvation shell.

Computational details

Ab initio MD simulations of the complexes were performed using the CP2K⁵¹ simulation package. We chose GPW⁵² method, the



BLYP-D2^{53–55} DFT functional, together with a DZVP-MOLOPT-GTH^{56,57} basis sets for all atoms. The simulations were performed in an *NVT* ensemble at 300 K using a global CSV thermostat⁵⁸ with 500 fs time constant. All hydrogen atoms were simulated as deuterium atoms, which allowed us to increase the time step to 1 fs, but throughout the paper we will refer to them as to protons. The selected time step is at least 10 times shorter than the period of the expected highest-frequency nuclear vibrational motion in the system (CD stretching), which satisfies the usual criterion proposed for the Born–Oppenheimer MD.⁵⁹ The employed SCF convergence was 10^{-6} a.u. and plane wave cutoff was set to 450 Ry. The molecular dynamics was done in a cubic periodic box with a side length of 15 Å. We have run three trajectories: for a FHF[−] in vacuum, in dichloromethane (CH₂Cl₂) and in tetrachloromethane (CCl₄). For the trajectories in condensed phase the solvent cells were previously equilibrated (energy minimization followed by 6 ps AIMD run). Then the complexes were inserted into the solvent box by calculating the molecular volume of the overlapping van der Waals radii of its atoms and removing the equivalent volume of solvent molecules calculated in the same way. This resulted in a box containing 33 CH₂Cl₂ molecules and FHF[−] at a density 1.4 g cm^{−3} and 22 CCl₄ molecules at a density 1.68 g cm^{−3}. The systems were equilibrated for 5 ps, and then the simulation continued for another 11 ps (vacuum) or 25 ps (CH₂Cl₂ and CCl₄) which were used for data sampling. We used VMD⁶⁰ and TRAVIS^{61,62} for trajectory analysis.

Chemical shifts were calculated in CP2K with the all-electron GAPW^{63,64} method and PBE0⁶⁵ functional, employing locally dense basis sets: pcSseg-2^{66–68} basis set on hydrogen and fluorine atoms and 6-31G* basis set for carbon and chlorine atoms. A number of random snapshots were extracted from every

trajectory (30 for FHF[−] in vacuum, 100 for FHF[−] in CH₂Cl₂ and CCl₄). For the solvated systems all solvent molecules were included in calculations. Isotropic magnetic shielding constants for ¹H and ¹⁹F were referenced to tetramethylsilane and CFCl₃ in vacuum, respectively.

Results

While the detailed description of the results of *ab initio* MD simulations concerning the solvation shell structure will be given in Discussion, here we present general information about the structure of the FHF[−] anion itself, according to the calculated trajectories. In all cases – in vacuum or dissolved in an aprotic solvent – FHF[−] anion exhibits strong and short hydrogen bond, that does not break during the simulation. Geometric parameters of the FHF[−] anion fluctuate around equilibrium values and the characteristics of these fluctuations depend on the medium. For convenience, we introduce here linear combinations of interatomic distances for the description of FHF[−] hydrogen bond as $q_1 = 1/2(r_{\text{FH}} - r_{\text{HF}})$ and $q_2 = r_{\text{FH}} + r_{\text{HF}}$. For a linear hydrogen bond these parameters have a clear physical meaning: q_1 represents the shift of the proton from the centre of the hydrogen bond and q_2 represents its overall length. The change of the q_1 sign corresponds to proton crossing the centre of the H-bond (the center of the F...F distance). Note that the sign of q_1 value is defined by the numbering of fluorine atoms, which in our case was chosen arbitrary and kept consistently during the analysis.

In Fig. 1–3 the data for FHF[−] in vacuum, dissolved in CH₂Cl₂ and dissolved in CCl₄ are given, respectively. The following characteristic are plotted: (a) the time dependence of the

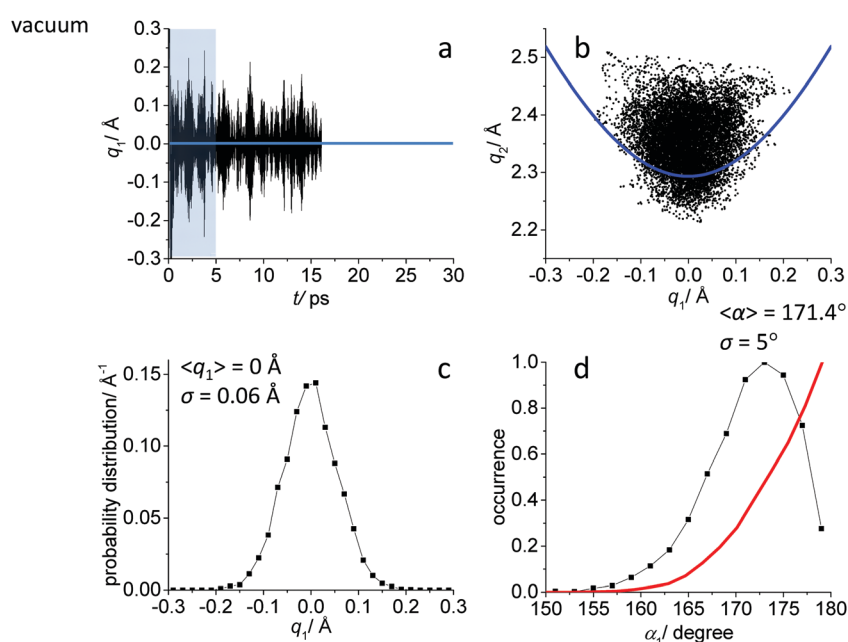


Fig. 1 *Ab initio* MD trajectory analysis: geometry of FHF[−] anion in vacuum. (a) The time dependence of $q_1 = 1/2(r_{\text{FH}} - r_{\text{HF}})$. (b) The interdependence of q_1 and $q_2 = r_{\text{FH}} + r_{\text{HF}}$. (c) The probability distribution of q_1 values. (d) The occurrence of different FHF angles α with cone correction (red curve) and without it (black curve). For more details see text.



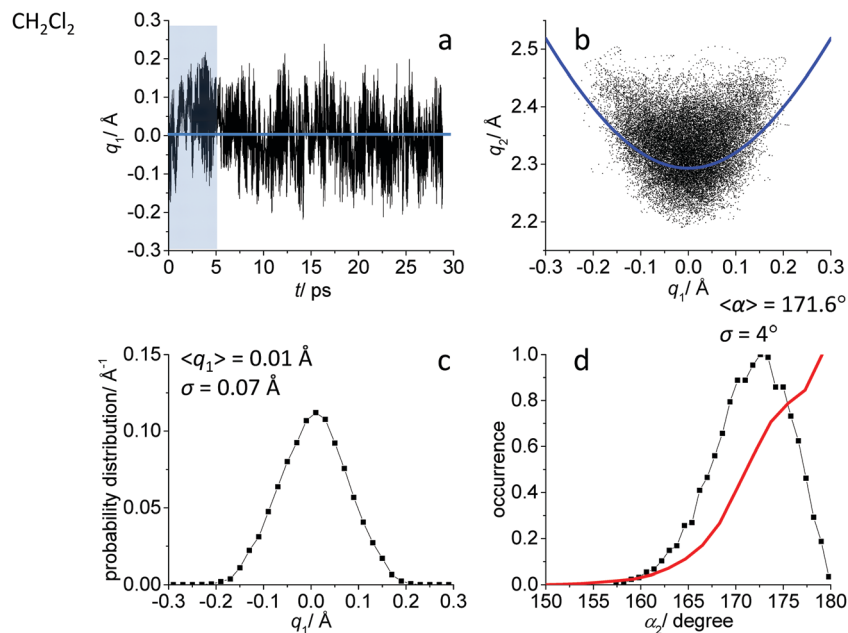


Fig. 2 *Ab initio* MD trajectory analysis: geometry of FHF⁻ anion dissolved in CH₂Cl₂. (a) The time dependence of $q_1 = 1/2(r_{\text{FH}} - r_{\text{HF}})$. (b) The interdependence of q_1 and $q_2 = r_{\text{FH}} + r_{\text{HF}}$. (c) The probability distribution of q_1 values. (d) The occurrence of different FHF angles α with cone correction (red curve) and without it (black curve). For more details see text.

hydrogen bond asymmetry parameter q_1 ; (b) the interdependence of q_1 and the overall hydrogen bond length parameter q_2 ; (c) the probability distribution of q_1 values and (d) the occurrence of different FHF angles with cone correction (red curve) and without it (black curve).

Fig. 1a, 2a and 3a show that in all cases the bridging particle crosses the midpoint of the hydrogen bridge ($q_1 = 0 \text{ \AA}$) many

times during the simulation. In Fig. 1b, 2b and 3b we show the interdependence of q_1 and q_2 parameters, which is barely noticeable in Fig. 1b and becomes progressively more apparent in Fig. 2b and 3b. For future reference, we have added to the Fig. 1b, 2b and 3b a curve, corresponding to the previously established q_1 - q_2 correlation. This correlation represents FHF⁻ geometry changes along the proton transfer reaction pathway

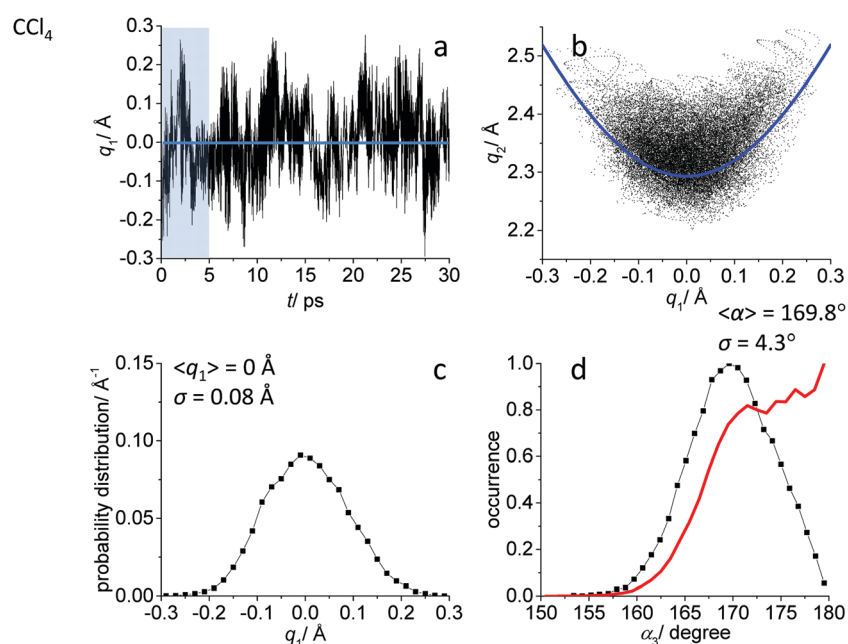


Fig. 3 *Ab initio* MD trajectory analysis: geometry of FHF⁻ anion dissolved in CCl₄. (a) The time dependence of $q_1 = 1/2(r_{\text{FH}} - r_{\text{HF}})$. (b) The interdependence of q_1 and $q_2 = r_{\text{FH}} + r_{\text{HF}}$. (c) The probability distribution of q_1 values. (d) The occurrence of different FHF angles α with cone correction (red curve) and without it (black curve). For more details see text.



in vacuum. The curve was constructed according to ref. 69 and stems from the so-called valence bond order model of hydrogen bonded complexes:^{70–72}

$$p_1 + p_2 = 1, p_1 = \exp(-(r_{\text{FH}} - r^0)/b); p_2 = \exp(-(r_{\text{HF}} - r^0)/b), \quad (1)$$

where p_1 and p_2 are called bond orders, $r^0 = 0.897 \text{ \AA}$ and $b = 0.36 \text{ \AA}$. The parameter r^0 has the meaning of the $\text{F} \cdots \text{H}$ distance in a hypothetical free FH molecule, while b describes how rapidly the FH bond order falls with the $\text{F} \cdots \text{H}$ distance (in other words, the parameter b is chosen in such a way that the equation $p_1 + p_2 = 1$ is better fulfilled). From eqn (1) one can derive that

$$q_2 = 2r^0 + 2q_1 + 2b \ln(1 + \exp(-2q_1/b)). \quad (2)$$

The probability distributions of q_1 values are shown in Fig. 1c, 2c and 3c (see also the distribution of $\text{F} \cdots \text{H}$ distances in Fig. S1 in ESI†). Quite expectedly, considering the symmetry of the system, these distributions are centred at $q_1 = 0 \text{ \AA}$, which corresponds to the central-symmetric anion. The reasons why there are changes in the widths and general shapes of distributions will be given in Discussion. The probability distributions of q_2 and $\text{F} \cdots \text{F}$ distance r_{FF} for all three studied systems are shown in Fig. S1 in ESI.† For three systems (FHF^- in vacuum, in CH_2Cl_2 and in CCl_4 medium) these distributions for each parameter are qualitatively similar. However, there are some changes in the shapes, which will be discussed below.

Finally, in Fig. 1d, 2d and 3d we demonstrate that the average structure of FHF^- anion is linear in vacuum and in solution. This topic deserves some comments. The bent structures are progressively less and less energetically favoured when FHF angle α deviates from linearity. Nevertheless, the statistical weight of the bent structures increases proportionally to the $\sin(\alpha)$. As a result, the distributions of angles start to show maxima at $\alpha < 180^\circ$. In other words, the most probable structure of the FHF^- anion is bent, even in vacuum. For example, the most probable angle α equals to 171.4° for FHF^- in vacuum, 171.6° in CH_2Cl_2 and 169.8° in CCl_4 (these values are close to each other, suggesting that there is not really a difference in the stability of the bent geometries). However, if one performs so called cone correction, which takes into account the statistical weight of each value of the angle α , one obtains the distribution functions as shown in Fig. 1d, 2d and 3d as red curves. In all cases the cone-corrected most probable (most energetically favoured) FHF angle α is 180° .

The dependencies of ^1H and ^{19}F NMR chemical shifts on q_1 values for the studied systems are given in Fig. 4–6. The average values of chemical shifts are added to the figures and also collected in Table 1. The average values for fluorine atoms $^{19}\text{F}_a$ and $^{19}\text{F}_b$ coincide within a couple of ppm, indicating that the set of snapshots used to calculate the average is a sufficiently representative one.

The $\delta^1\text{H}$ values for three systems (Fig. 4a, 5a and 6a) behave in a qualitatively similar fashion: a symmetric bell-shaped dependence on q_1 with the maximum corresponding to $q_1 = 0 \text{ \AA}$, which is typical for formally symmetric hydrogen bonds of

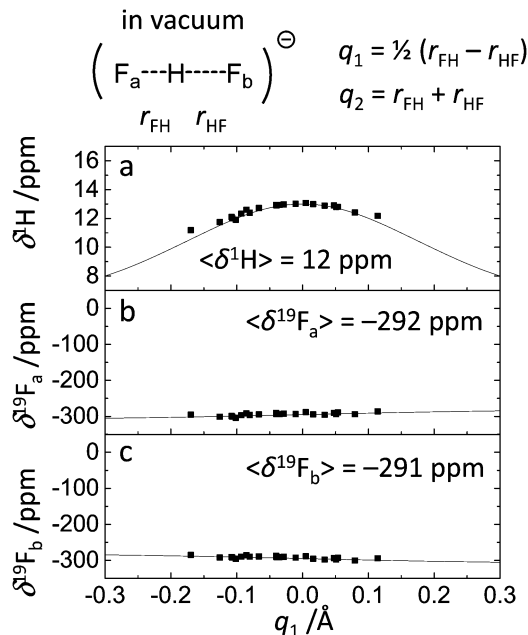


Fig. 4 ^1H and ^{19}F NMR chemical shifts for FHF^- in vacuum vs. q_1 for 30 random snapshots of the trajectory. Fitted curves correspond to eqn (3) and (4) with parameters listed in Table 2. $\langle \delta^1\text{H} \rangle$ and $\langle \delta^{19}\text{F}_{a,b} \rangle$ stand for the values of chemical shifts averaged over the given set of points.

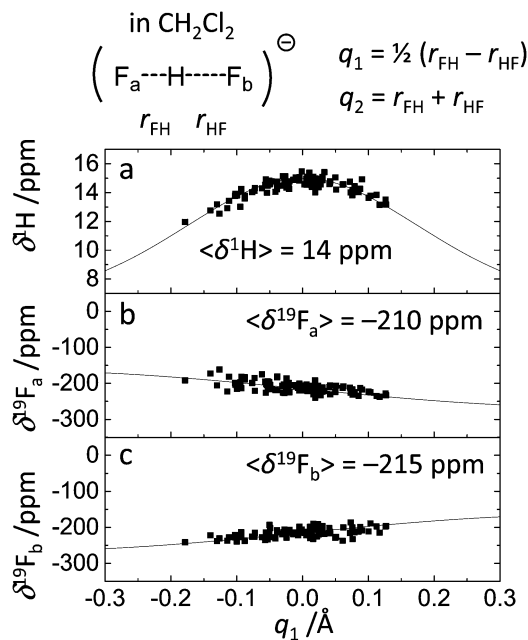


Fig. 5 ^1H and ^{19}F NMR chemical shifts for FHF^- in CH_2Cl_2 vs. q_1 for 100 random snapshots of the trajectory. Fitted curves correspond to eqn (3) and (4) with parameters listed in Table 2. $\langle \delta^1\text{H} \rangle$ and $\langle \delta^{19}\text{F}_{a,b} \rangle$ stand for the values of chemical shifts averaged over the given set of points.

various types.^{19,67,70} Following the approach outlined in ref. 67, we have attempted to fit these points using the equation

$$\delta^1\text{H} = \delta(\text{FH}) + \Delta \cdot (4p_1 \cdot p_2)^2, \quad (3)$$



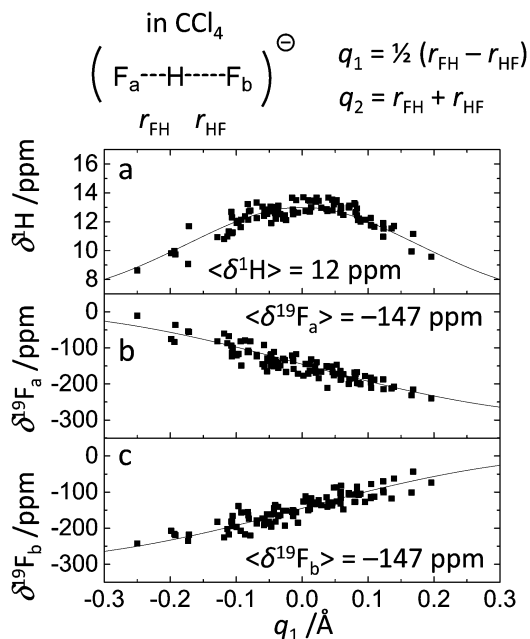


Fig. 6 ^1H and ^{19}F NMR chemical shifts for FHF^- in CCl_4 vs. q_1 for 100 random snapshots of the trajectory. Fitted curves correspond to eqn (3) and (4) with parameters listed in Table 2. $\langle \delta^1\text{H} \rangle$ and $\langle \delta^{19}\text{F}_{a,b} \rangle$ stand for the values of chemical shifts averaged over the given set of points.

Table 1 The values of average ^1H and ^{19}F NMR chemical shifts for the FHF^- anion in vacuum, dissolved in CH_2Cl_2 and dissolved in CCl_4 (see also Fig. 4–6). The labelling of fluorine atoms (a and b) was done arbitrarily and kept consistent during the analysis

System	$\langle \delta^1\text{H} \rangle$, ppm	$\langle \delta^{19}\text{F}_a \rangle$, ppm	$\langle \delta^{19}\text{F}_b \rangle$, ppm
FHF^- in vacuum	12	-292	-291
FHF^- in CH_2Cl_2	14	-210	-215
FHF^- in CCl_4	12	-147	-147

where p_1 and p_2 are q_1 -dependent bond orders from eqn (1), $\delta(\text{FH})$ is the proton chemical shift of a hypothetical free FH molecule and Δ is the excess chemical shift, which determines the maximum value $\delta^1\text{H}$ reaches at $q_1 = 0 \text{ \AA}$. The dependences of $\delta^{19}\text{F}$ values on q_1 for two fluorine atoms (Fig. 4b, c, 5b, c and 6b, c) are essentially the same, only the sign of q_1 is reversed. On the first glance, these dependencies look linear. However, they can be fit using an equation similar to the one reported in ref. 67:

$$\delta^{19}\text{F} = \delta(\text{FH}) \cdot p_1 + \delta(\text{F}^-) \cdot p_2, \quad (4)$$

where $\delta(\text{FH})$ and $\delta(\text{F}^-)$ are fluorine chemical shifts of hypothetical free FH molecule and F^- anion, respectively. The fitted curves are depicted in Fig. 4–6 as black traces and the parameters are given in Table 2. The spread of the data points does not allow one to obtain the precise values of the limiting chemical shifts, so the values given in Table 2 serve as rough estimates. Nevertheless, it might be concluded that the sensitivity of the $\delta(\text{FH})$ to the medium is much larger than that of $\delta(\text{F}^-)$. It would be interesting to explicitly calculate these values by performing *ab initio* MD simulations of isolated FH and F^-

Table 2 The values of the fitted parameters of eqn (3) and (4) used to plot black traces in Fig. 4–6

System	$\delta(\text{FH})$, ppm	Δ , ppm	$\delta(\text{FH})$, ppm	$\delta(\text{F}^-)$, ppm
FHF^- in vacuum	6	7	-310	-280
FHF^- in CH_2Cl_2	6	9	-150	-280
FHF^- in CCl_4	6	7	+30	-320

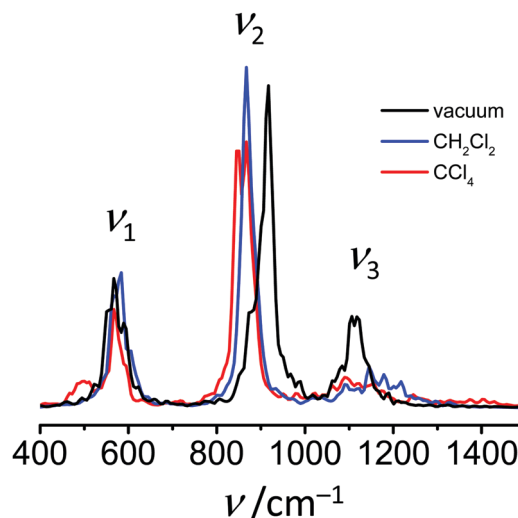


Fig. 7 Power spectra of FHF^- in vacuum (black line), in CH_2Cl_2 (blue line) and in CCl_4 (red line).

in vacuum and in the medium. However, this task was beyond the scope of this work.

Finally, in Fig. 7 we plot the power spectra, *i.e.* Fourier transformed velocity autocorrelation function of FHF^- atoms. In each case three maxima can be observed at *ca.* 570 cm^{-1} , around 900 cm^{-1} and slightly above 1100 cm^{-1} . We remind here that in order to increase the time step of the simulations all hydrogens were simulated with double mass (as deuterons), which affects the vibrational frequencies. The assignment of these maxima to normal modes of the anion can be done either by comparison with the previously reported experimentally measured or computed values of FDF^- vibrational frequencies,^{26,39} or by performing the normal mode analysis implemented in TRAVIS software package.⁷³ The results of the two approaches coincide and give the following assignment in the order of increasing frequencies: symmetric stretch, bending and asymmetric stretch.

Discussion

FHF^- in vacuum

The structural and spectroscopic features of FHF^- anion are presented in Fig. 1 and 4 and were briefly described in the Results section. The widths of q_1 and q_2 distributions and the width of FHF angle α distribution serve us as a starting point for the discussion of the solvent effects below. Nevertheless, it is interesting to compare our results with the results of PIMD simulation of FHF^- and FDF^- anions in vacuum (MP2/6-31++G**),



published by Suzuki *et al.*⁴⁸ In ref. 48 authors find that “nuclear quantum effects stretch the FH and FF distances due to potential anharmonicity”. Despite the differences in the level of theory, the average bond lengths and angles agree rather well (for FDF⁻ PIMD and this study, respectively: average F··D

distances are 1.163 Å and 1.178 Å; average F··F distances are 2.324 Å and 2.349 Å; average angles α are 169.6° and 171.4°). Quantum effects also lead to a wider distribution of bond lengths. This effect is more pronounced for hydrogens as compared to deuterons. For example, the root mean square

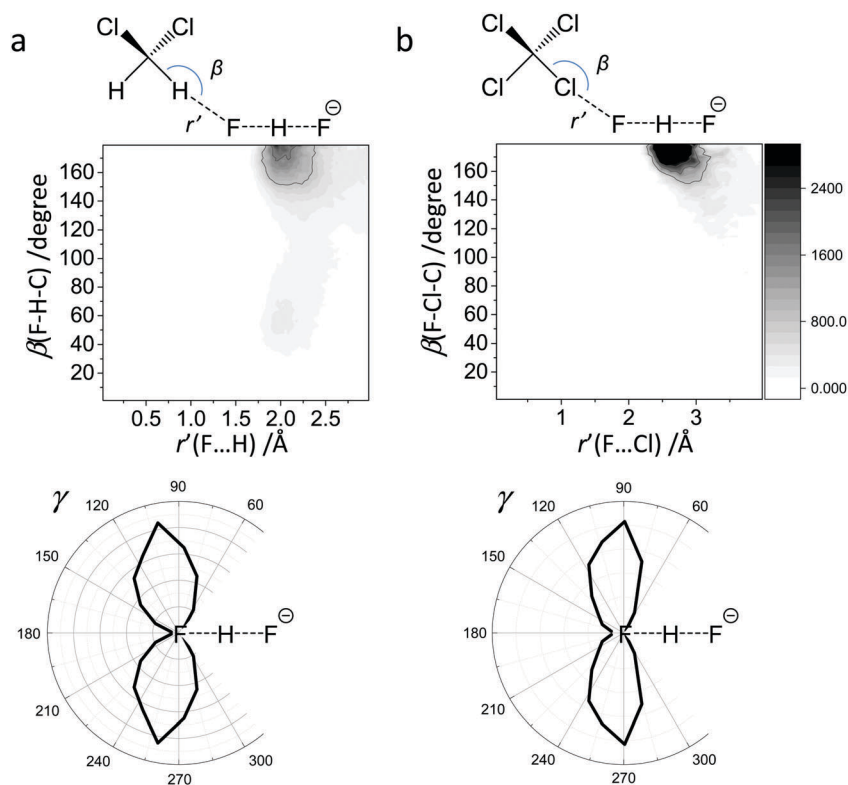


Fig. 8 The directionality of the intermolecular solvent-solute interactions: correlations between the intermolecular distance r' and the bond angle β . (a) FHF⁻ in CH₂Cl₂ (CH···F hydrogen bond). (b) FHF⁻ in CCl₄ (Cl···F halogen bond).

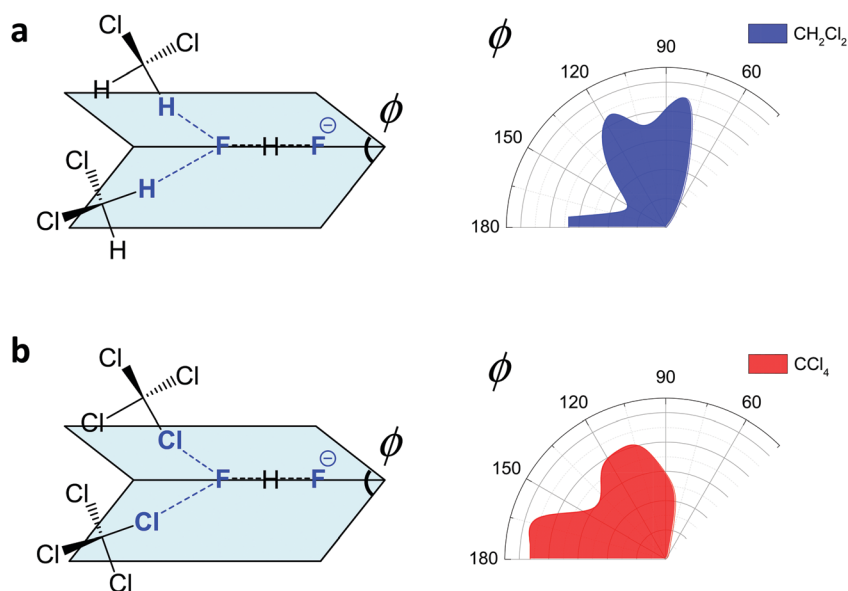


Fig. 9 The distribution of dihedral angles (see schemes in the left part of the figure; atoms defining the dihedral angle are marked blue) in case of two or more molecules interacting with one fluorine atom of FHF⁻. (a) CH₂Cl₂ solvent; (b) CCl₄ solvent.



deviation for $F \cdots D$ distance in PIMD is 0.097 Å and in our Born–Oppenheimer MD simulation it equals to 0.063 Å. In general, nuclear quantum effects are without a question important for a neat description of strong H-bond parameter distribution,^{21–24} however in this paper we focus on solvent–solute interactions and comparisons of different types of specific interactions in condensed phase.

Note, that the distribution of spectroscopic parameters is rather broad even without the influence of fluctuating solvent molecules in the solvation shell. For example, the ^1H NMR chemical shifts cover the range from 9 ppm to 13 ppm (Fig. 4a), while ^{19}F chemical shift are spread over *ca.* 20 ppm region (Fig. 4b and c).

FHF[−] dissolved in CH₂Cl₂

For FHF[−] in CH₂Cl₂ the solvent–solute interactions lead to the spread of the data points in q_1 – q_2 plot (Fig. 2b): the cloud of points starts to “smear” along the solid “equilibrium” curve. The corresponding distribution of q_1 values broadens ($\sigma = 0.07$ Å), as compared to FHF[−] in vacuum, while the average $F \cdots F$ distance shortened. It means that the correlation between the proton position and the overall length of the bridge continues to be fulfilled, but there are factors which compress the anion as a whole and also lead to a larger asymmetrization of the anion. The nature of the asymmetrization could be elucidated, considering that along the trajectory, close to each fluorine atom there are one, two, three or even more CH groups of solvent molecules, some of which are forming weak $\text{CH} \cdots \text{F}$ hydrogen bonds. One of such molecules is shown at the top of Fig. 8a (see also the definitions of the distance $r'(\text{F} \cdots \text{H})$ and the angle $\beta(\text{F}–\text{H}–\text{C})$). These $\text{CH} \cdots \text{F}$ bonds are essentially linear and *ca.* 2.0 Å in length, as evidenced by the correlation plot of r' and β . The $\text{F}–\text{F}–\text{H}$ angles γ are distributed around 100° (see Fig. 8a, bottom). This is what one would expect assuming that the interaction occurs with one of the lone pairs of F nucleus. In this case one would expect up to three solvent molecules per fluorine. However, it might be that the maximum number of interacting solvent molecules is dictated primarily by the steric factors.⁷⁴ In order to check this, in Fig. 9a we plot the distribution of $\text{F}–\text{F}–\text{H}–\text{H}$ dihedral angles ϕ (four atoms defining the angle are marked blue in the figure) for the cases when there are two and more $\text{CH} \cdots \text{F}$ bonds at the fluorine ($r' < 2.5$ Å and $150^\circ < \beta < 180^\circ$ criteria were used). In the majority of cases there are two solvent molecules bound to fluorine and these molecules preferentially occupy the positions at $\phi = 90$ – 120° , which is expected if the bonding occurs primarily *via* the sp^3 -hybridized lone pairs of fluorine. In case of pure steric repulsion of CH₂Cl₂ molecules the most abundant angle ϕ would be 180°.

The NMR parameters change significantly: firstly, the average $\delta^1\text{H}$ value grows by 2 ppm: secondly, the scattering of the $\delta^{19}\text{F}_{\text{a,b}}$ points dramatically increases and the limiting value, corresponding to the “free” FH molecule, changes from −310 to −150 ppm. (As the other limiting value for “free” F[−] changes much less, the average $\delta^{19}\text{F}$ changes by *ca.* 80 ppm.) It is difficult to compare directly the absolute values of computed average chemical shifts with the experimental ones, which are collected in Table S1 (ESI[†]), primarily because in the experiments the conditions are never the

same as in our calculations (presence on the counterion, usage of different solvents, in some cases at different temperature). Nevertheless, one can say that admitting a systematic computational error of about 1 ppm, the average $\delta^1\text{H}$ value of 14 ppm is very close to the experimental value of 16.6 ppm, reported for $\text{Bu}_4\text{N}^+\text{FHF}^-$ dissolved in $\text{CDF}_3/\text{CDF}_2\text{Cl}$ mixture at low temperature.³⁵ This holds even more when comparing with the usual range of proton NMR chemical shifts, *e.g.* 5 ppm for liquid water and about 1 ppm for isolated water.

FHF[−] dissolved in CCl₄

The CCl₄ solvent is often viewed as an inert one, influencing the dissolved complexes to a minimal degree. However, this is not the case for FHF[−] in CCl₄. Here the tendencies described in the previous subsection (FHF[−] in CH₂Cl₂) continue to develop: the q_1 – q_2 dependence is more clearly stretched along the

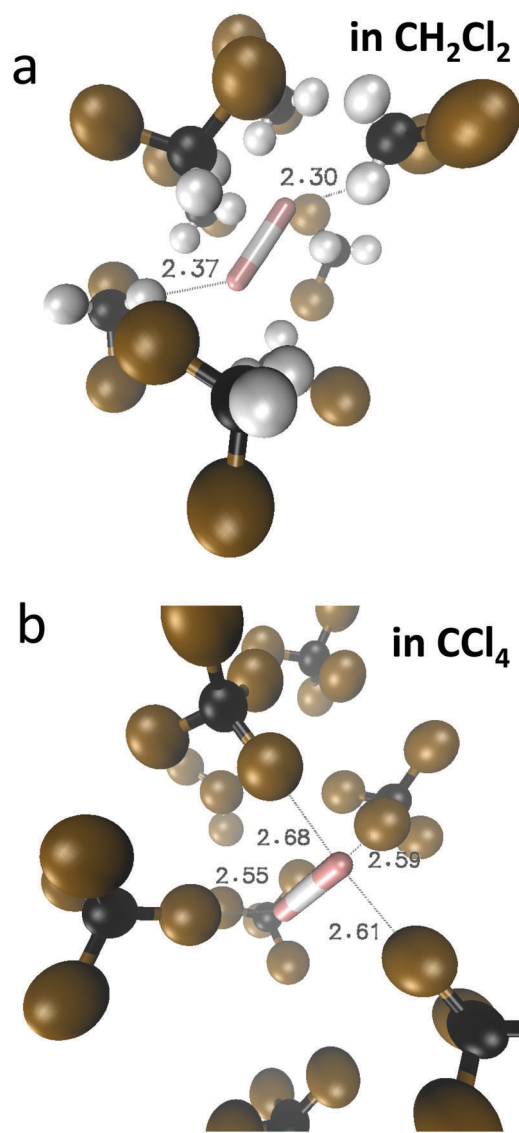


Fig. 10 Typical snapshots of the trajectory, showing the approximate structure of the first solvation shell around FHF[−] anion. (a) CH₂Cl₂ solvent; (b) CCl₄ solvent.



equilibrium line (Fig. 3b), gradually approaching the situation when intermolecular interactions with the solvent would break the symmetry of the complex and lead to formation of an effective double-well potential curve for proton motion. The distribution of q_1 values is also broader (Fig. 3c). This is the evidence for the stronger intermolecular interaction between the solvent and the solute, which in this case is the halogen bonding between the lone pairs of fluorines and the σ -holes of chlorines. From Fig. 8b it is apparent that distributions of the F...Cl interatomic distances r' and of the halogen bond angles β (F-Cl-C) are quite narrow. The r' distances are shorter than 3 Å, which is smaller than the sum of van der Waals radii of the atoms involved⁷⁵ and the β angle is close to linearity ($>160^\circ$). The F-F-Cl angles γ (Fig. 8b, bottom) are clustered around 90 – 110° , quite close to the directions of the lone pairs of fluorines. Note however, that there are occasions when CH approaches FHF⁻ at 90° to its axis, possibly indicating the steric repulsion between the solvent molecules. Interestingly, for CH₂Cl₂ no halogen bonding to the lone pairs of fluorines has been observed in the trajectory (which is linked to the smaller σ -hole in CH₂Cl₂ and its substantial proton-donating ability). The mutual orientation of CCl₄ molecules around the fluorine atom is analysed in Fig. 9b, where the distribution of F-F-Cl-Cl angles is shown. Similar to the results obtained for CH₂Cl₂, for CCl₄ the most abundant configurations have two solvent molecules at fluorine atom ($r' < 3.1$ Å; $150^\circ < \beta < 180^\circ$) and these molecules occupy the relative positions at $\phi = 110$ – 130° , fitting to the directions of fluorine lone pairs.

For CCl₄ the limiting values of ¹⁹F chemical shifts have also changed significantly: $\delta(\text{FH})$ has increased from -150 ppm (for CH₂Cl₂) to $+50$ ppm (for CCl₄), while $\delta(\text{F}^-)$ has changed much less (from -280 ppm for CH₂Cl₂ to -320 ppm for CCl₄). The difference between the limiting fluorine chemical shifts is 370 ppm and subsequently, the data points in Fig. 6b and c are noticeably scattered. The exceptionally high sensitivity of ¹⁹F NMR chemical shifts of FHF⁻ anion to the hydrogen bond geometry is not surprising, as the shieldings are usually

extremely sensitive even to sub-picometer fluctuations in bond lengths. However, the overall solvent sensitivity, *i.e.* the span of the $\delta^{19}\text{F}$ values in CH₂Cl₂ and CCl₄, is surprising and noteworthy in itself, as the experimentally measured ¹⁹F chemical shifts values reported previously in the literature for different environments lie relatively close to each other, covering a narrow range from -141 to -155 ppm (see Table S1 in ESI†). At the moment it is hard to attribute this sensitivity of computed ¹⁹F chemical shifts to any physical or dynamical parameter of the system, though it seems that the $\delta(\text{FH})$ values are mostly solvent-dependent.

The calculated power spectra (Fig. 7) are not intended to simulate the experimental IR spectra and considered here in a more qualitative way. In the power spectra the difference between the two solvents can be seen (Fig. 7; see also Table S2 in ESI†). Band positions of bending (ν_2) and asymmetric stretching (ν_3) vibrations in liquids are shifted noticeably in comparison to vacuum, while relative differences between CH₂Cl₂ and CCl₄ are somewhat less pronounced. The bending vibration shifts towards lower frequencies upon dissolution, while the frequency of the asymmetric stretching increases. The interpretation of these changes can be done considering that the average F...F distance shortens in the condensed medium, but increases again with increasing solvent-solute interaction (2.32 Å in CH₂Cl₂, 2.33 Å in CCl₄ and 2.35 Å in vacuum). The shortening of the F...F distance “flattens” the potential energy surface along the bending coordinate,⁴⁰ which decreases the vibrational frequency. In contrast, the asymmetric stretching potential becomes less flat⁴⁶ and the corresponding vibrational frequency increases.

Solvation shell structure. Hydrogen/halogen bond cooperativity

In Fig. 10 we show as an example rather typical snapshots of the solvent structure around the FHF⁻ anion. One can see that in the cases of CH₂Cl₂ and CCl₄ the solvation shell contains a small number of solvent molecules many of which form non-covalent interactions with the fluorine atoms. There is always at least one solvent molecule close to each of the fluorine atoms,

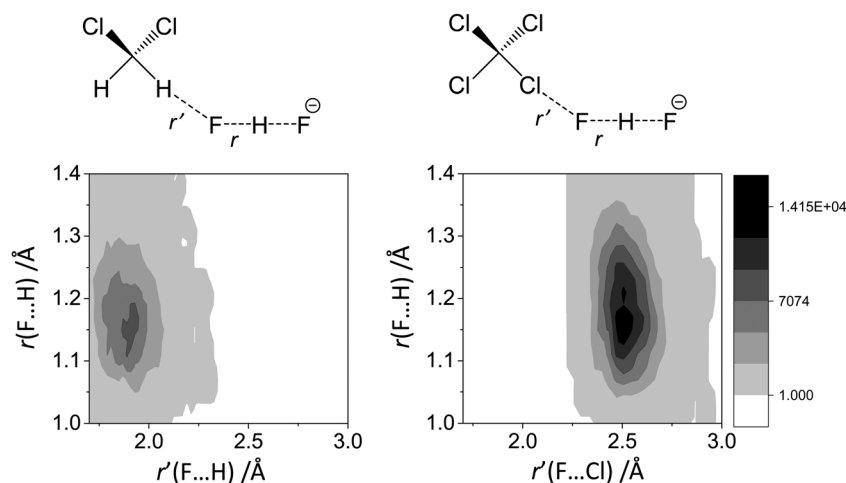


Fig. 11 The interdependence between the bridging proton position $r(\text{F}\cdots\text{H})$ distance and the intermolecular distance r' to the closest neighbour solvent molecule. (a) FHF⁻ in CH₂Cl₂. (b) FHF⁻ in CCl₄.



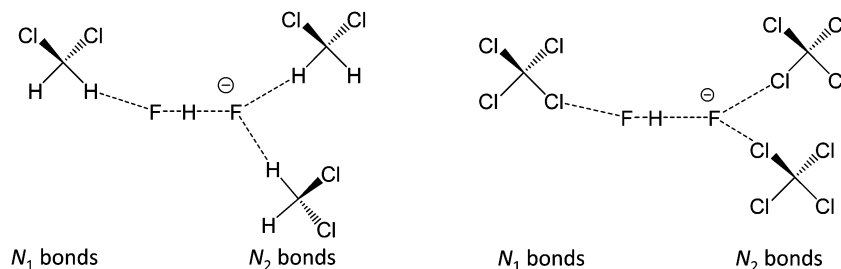


Fig. 12 The scheme introducing the numbers N_1 and N_2 of solvent molecules interacting with FHF^- anion. Left: FHF^- in CH_2Cl_2 ($r' < 2.5 \text{ \AA}$; $150^\circ < \beta < 180^\circ$); right: FHF^- in CCl_4 ($r' < 3.1 \text{ \AA}$; $150^\circ < \beta < 180^\circ$). For the definitions of r' and β see Fig. 8, top.

as could be seen from Fig. 11, where the joint distribution of the proton position ($\text{F}\cdots\text{H}$ distance within the FHF^- anion) and the distance to the closest solvent molecule ($\text{F}\cdots\text{HC}$ or $\text{F}\cdots\text{ClC}$ distances for hydrogen and halogen bond, respectively) are shown. Note, however, that the position of the closest solvent molecule does not determine the bridging proton position in FHF^- anion (in both cases the $\text{F}\cdots\text{H}$ distances cover the similar range from 1.05 to 1.25 \AA). This is because there could be two, three or even more solvent molecules interacting simultaneously with the lone pairs of each fluorine atom. In Fig. 12 the number of molecules interacting with F_a and F_b is denoted N_1 and N_2 , respectively. In order to determine the number of interacting solvent molecules we have chosen the same criteria, as mentioned above: for hydrogen bonds the $\text{F}\cdots\text{HC}$ distance

should be shorter than 2.5 \AA , for halogen bond the $\text{F}\cdots\text{ClC}$ bond should be shorter than 3.1 \AA , while in both cases the angle β (see Fig. 8) should lie within the range $150^\circ < \beta < 180^\circ$. At many occasions N_1 and N_2 values do not match, making the solvation shell asymmetric and causing the asymmetric bridging proton position within the FHF^- anion. In other words, it is the balance between the local solvations of one and of the other fluorine atoms that determines the proton position in the FHF^- bridge. The diagram showing the number of solvent molecules on either side of FHF^- anion is presented in Fig. 13. Clearly, the non-equal numbers of solvent-solute interactions is a quite common occurrence during the simulation. In order to demonstrate that the asymmetry in the solvation shell is linked to the asymmetric proton position, we have introduced the number $D = N_1 - N_2$. Positive D values mean that F_a is better solvated, while negative D values mean that F_b is better solvated.

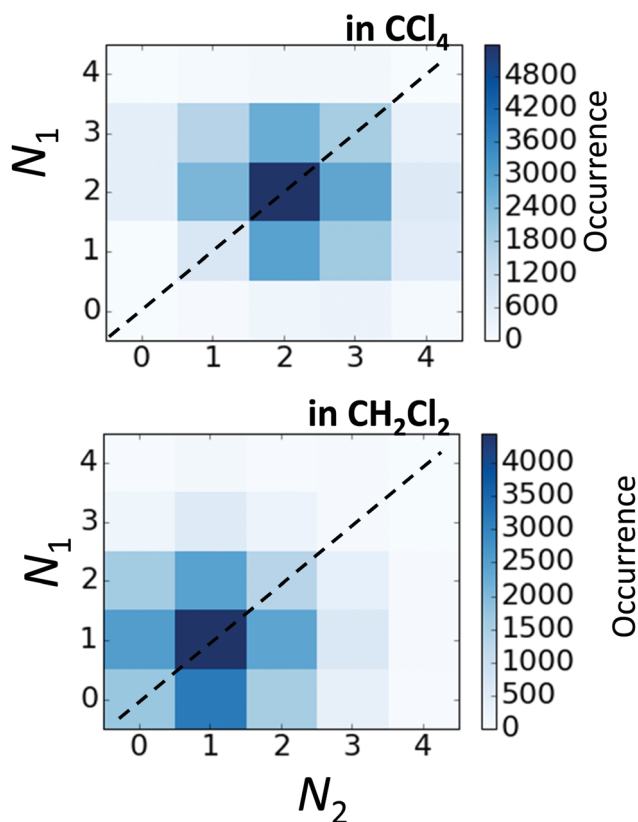


Fig. 13 The correlation between N_1 and N_2 values (defined in Fig. 12) for FHF^- in CH_2Cl_2 (top) and in CCl_4 (bottom).

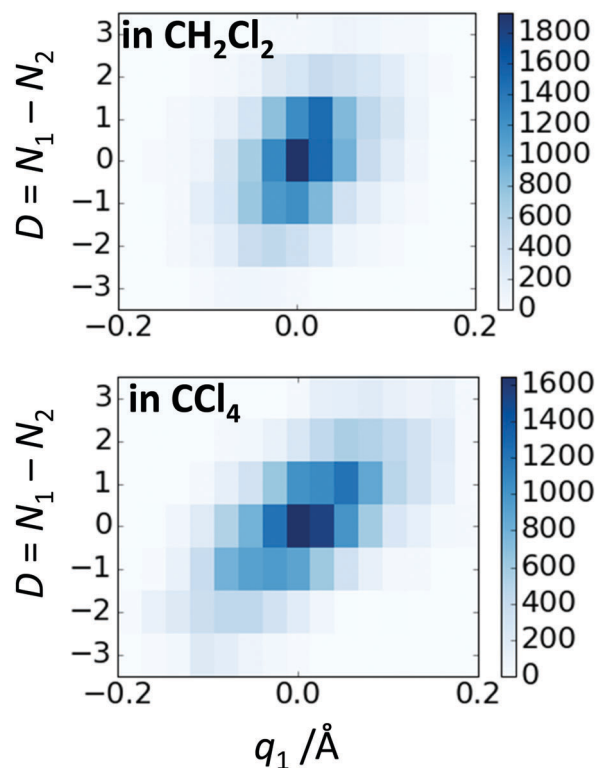


Fig. 14 The correlation between $D = N_1 - N_2$ and q_1 values for FHF^- in CH_2Cl_2 (top) and in CCl_4 (bottom).



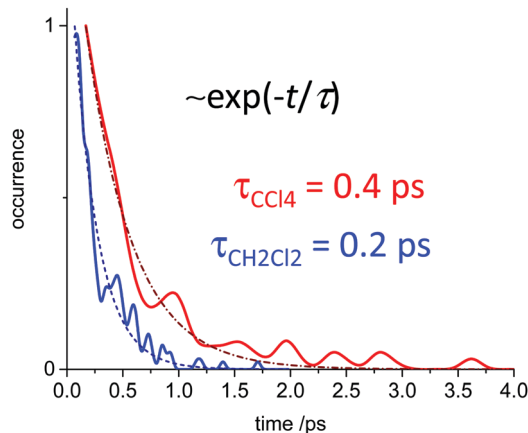


Fig. 15 The distribution of solvent–solute interaction lifetimes, *i.e.* the residence times of solvent molecules fulfilling the criteria for non-covalent interaction. Blue trace: FHF[−] in CH₂Cl₂ ($r' < 2.5$ Å; $150^\circ < \beta < 180^\circ$). Red trace: FHF[−] in CCl₄ ($r' < 3.1$ Å; $150^\circ < \beta < 180^\circ$). For the definitions of r' and β see Fig. 8, top.

In Fig. 14 we plot the correlation between D and q_1 values. If there would be no interdependence, the $q_1 < 0$ Å and $q_1 > 0$ Å parts of plot would look the same. However, in our case the data is stretched along the diagonal. This correlation is pronounced weaker in case of CH₂Cl₂, which does not break significantly the symmetry of the FHF[−] anion, and the correlation is pronounced stronger in case of CCl₄. As mentioned before, for us the stronger interaction of FHF[−] with CCl₄ was an unexpected result. In Fig. 15 we plot the distribution of the solvent–solute bond's lifetimes, confirming that this lifetime for CCl₄ molecules is twice longer than for CH₂Cl₂ molecules.

Conclusions

For FHF[−] in vacuum, dissolved in CH₂Cl₂ or CCl₄ the average $D_{\infty h}$ symmetry is retained, but there are differences in transient symmetry, which depends on the specific intermolecular interaction with the solvent. In case of CH₂Cl₂ is appeared to be CH \cdots F hydrogen bonding (no halogen bonds were formed during the simulation), while in case of CCl₄ it is halogen bonding. Both types of intermolecular interactions are preferentially aligned with the lone pairs of fluorine atoms of FHF[−]. The cause of the proton displacement in FHF[−] seems to be asymmetric solvation, primarily the different number of solvent molecules, non-covalently bonded to fluorine atoms. The stronger the interaction with the solvent, the broader is the q_1 distribution.

It could be speculated that even stronger specific interaction with the solvent would eventually break the symmetry of FHF[−] completely and led to the situation better described by a two-state proton tautomerism:⁷⁶ elongated F \cdots F distance and bimodal distribution of asymmetric proton positions. This transition from a “single-well” to a “double-well” situation could be done in a smooth continuous way (the process previously considered hypothetically for the increased bond length for both symmetric hydrogen⁴⁶ and symmetric halogen bonds⁷⁷).

NMR chemical shift appear to be sensitive markers for the spectral diagnostic of the hydrogen bond geometry, responding sensitively to the bridging proton position and to the medium itself. There is a huge solvent effect on average $\delta^{19}\text{F}$, mainly because the limiting chemical shift of FH is strongly solvent-dependent (the chemical shift of F[−] anion is much less sensitive). The power spectrum (the autocorrelation function of the atom's velocities), constructed on the basis of computed trajectory, shows the high sensitivity to the average F \cdots F distance.

Conflicts of interest

There are no conflicts to declare.

Acknowledgements

Ab initio MD simulations were performed within the framework of a grant from the Deutsche Forschungsgemeinschaft Se1008/11-1. The analysis of the trajectory, solvent–solute interactions and calculations of the spectroscopic parameters were performed within the framework of the RFBR grant 17-03-00497. We thank Prof. Dr Gleb S. Denisov for valuable discussions of the project and Prof. Dr Hans-Heinrich Limbach for the inspiration of studying hydrogen bond symmetry and the interest in FHF[−] anion.

References

- (a) E. Puig, M. Garcia-Viloca, A. González-Lafont and J. M. Lluch, On the ionization state of the substrate in the active site of glutamate racemase. A QM/MM study about the importance of being zwitterionic, *J. Phys. Chem. A*, 2006, **110**, 717–725; (b) P. Deb, T. Haldar, S. M. Kashid, S. Banerjee, S. Chakrabarty and S. Bagchi, Correlating Nitrile IR Frequencies to Local Electrostatics Quantifies Noncovalent Interactions of Peptides and Proteins, *J. Phys. Chem. B*, 2016, **120**, 4034–4046.
- S. J. Grabowski, [FHF][−] – The Strongest Hydrogen Bond under the Influence of External Interactions, *Crystals*, 2016, **6**, 3/1–17.
- Y. Mori and Y. Masuda, Effect of solvent on proton location and dynamic behavior in short intramolecular hydrogen bonds studied by molecular dynamics simulations and NMR experiments, *Chem. Phys.*, 2015, **458**, 18–29.
- M. Garcia-Viloca, A. Gonzalez-Lafont and J. M. Lluch, Asymmetry of the Hydrogen Bond of Hydrogen Phthalate Anion in Solution. A QM/MM Study, *J. Am. Chem. Soc.*, 1999, **121**, 9198–9207.
- T. Yamashita and K. Takatsuka, Hydrogen-bond assisted enormous broadening of infrared spectra of phenol-water cationic cluster: An *ab initio* mixed quantum-classical study, *J. Chem. Phys.*, 2007, **126**, 074304/1–15.
- F. Dahms, R. Costard, E. Pines, B. P. Fingerhut, E. T. J. Nibbering and T. Elsaesser, The Hydrated Excess Proton in the Zundel Cation H₅O₂(+): The Role of Ultrafast Solvent Fluctuations, *Angew. Chem., Int. Ed.*, 2016, **55**, 10600–10605.



- 7 C. L. Perrin and J. S. Lau, Hydrogen-Bond Symmetry in Zwitterionic Phthalate Anions: Symmetry Breaking by Solvation, *J. Am. Chem. Soc.*, 2006, **128**, 11820–11824.
- 8 C. L. Perrin, Are Short, Low-Barrier Hydrogen Bonds Unusually Strong?, *Acc. Chem. Res.*, 2010, **43**, 1550–1557.
- 9 C. L. Perrin and B. K. Ohta, Symmetry of NHN hydrogen bonds in solution, *J. Mol. Struct.*, 2002, **644**, 1–12.
- 10 C. L. Perrin and B. K. Ohta, Symmetry of O–H–O and N–H–N Hydrogen Bonds in 6-Hydroxy-2-formylfulvene and 6-Amino-fulvene-2-aldehydes, *Bioorg. Chem.*, 2002, **30**, 3–15.
- 11 C. L. Perrin and B. K. Ohta, Symmetry of N–H–N Hydrogen Bonds in 1,8-Bis(dimethylamino)naphthalene-H⁺ and 2,7-Dimethoxy-1,8-bis(dimethylamino)naphthalene-H⁺, *J. Am. Chem. Soc.*, 2001, **123**, 6520–6526.
- 12 P. M. Tolstoy, B. Koeppe, G. S. Denisov and H.-H. Limbach, Combined NMR/UV-Vis Spectroscopy in the Liquid State: Study of the Geometries of Strong OHO Hydrogen Bonds of Phenols with Carboxylic Acids, *Angew. Chem., Int. Ed.*, 2009, **48**, 5745–5747.
- 13 S. Pylaeva, C. Allolio, B. Koeppe, G. S. Denisov, H.-H. Limbach, D. Sebastiani and P. M. Tolstoy, Proton transfer in a short hydrogen bonded complex caused by solvation shell fluctuations: an *ab initio* MD and NMR/UV study of an (OHO)-bonded system, *Phys. Chem. Chem. Phys.*, 2015, **17**, 4634–4644.
- 14 B. Koeppe, J. Guo, P. M. Tolstoy, G. S. Denisov and H.-H. Limbach, Solvent and H/D Isotope Effects on the Proton Transfer Pathways in Heteroconjugated Hydrogen-Bonded Phenol-Carboxylic Acid Anions Observed by Combined UV-vis and NMR Spectroscopy, *J. Am. Chem. Soc.*, 2013, **135**, 7553–7566.
- 15 B. Koeppe, S. A. Pylaeva, C. Allolio, D. Sebastiani, E. T. J. Nibbering, G. S. Denisov, H.-H. Limbach and P. M. Tolstoy, Polar solvent fluctuations drive proton transfer in hydrogen bonded complexes of carboxylic acid with pyridines: NMR, IR and *ab initio* MD study, *Phys. Chem. Chem. Phys.*, 2017, **19**, 1010–1028.
- 16 P. M. Tolstoy, S. N. Smirnov, I. G. Shenderovich, N. S. Golubev, G. S. Denisov and H.-H. Limbach, NMR studies of solid state – solvent and H/D isotope effects on hydrogen bond geometries of 1:1 complexes of collidine with carboxylic acids, *J. Mol. Struct.*, 2004, **700**, 19–27.
- 17 B. C. K. Ip, I. G. Shenderovich, P. M. Tolstoy, J. Frydel, G. S. Denisov, G. Buntkowsky and H.-H. Limbach, NMR Studies of H/D Isotope and Phase Effects on 4-Methylpyridine-Pentachlorophenol Complexes and Implications for the Shapes of Hydrogen-bonded Protons in the Solid and the Liquid State, *J. Phys. Chem. A*, 2012, **116**, 11370–11387.
- 18 S. B. Lesnichin, P. M. Tolstoy, H. H. Limbach and I. G. Shenderovich, Counteranion-dependent mechanisms of intramolecular proton transfer in aprotic solution, *Phys. Chem. Chem. Phys.*, 2010, **12**, 10373–10379.
- 19 M. Pietrzak, J. P. Wehling, S. Kong, P. M. Tolstoy, I. G. Shenderovich, C. Lopez, R. M. Claramunt, J. Elguero, G. S. Denisov and H.-H. Limbach, Symmetrization of Cationic Hydrogen Bridges of Protonated Sponges Induced by Solvent and Counteranion Interactions as Revealed by NMR Spectroscopy, *Chem. – Eur. J.*, 2010, **16**, 1679–1690.
- 20 Y. Masuda, Y. Mori and K. Sakurai, Effects of Counterion and Solvent on Proton Location and Proton Transfer Dynamics of N–H···N Hydrogen Bond of Monoprotonated 1,8-Bis(dimethylamino)naphthalene, *J. Phys. Chem. A*, 2013, **117**, 10576–10587.
- 21 P. Durlak and Z. Latajka, *Ab initio* molecular dynamics study of the very short O–H···O hydrogen bonds in the condensed phases, *J. Theor. Chem. Comput.*, 2013, **1**, 65–72.
- 22 P. Durlak, K. Mierzwicki and Z. Latajka, Investigations of the very short hydrogen bond in the crystal of nitromalonamide *via* Car-Parrinello and path integral molecular dynamics, *J. Phys. Chem. B*, 2013, **117**, 5430–5440.
- 23 A. Jezierska-Mazzarello, R. Vuilleumier, J. J. Panek and G. Ciccotti, Molecular Property Investigations of an ortho-Hydroxy Schiff Base Type Compound with the First-Principle Molecular Dynamics Approach, *J. Phys. Chem. B*, 2010, **114**(1), 242–253.
- 24 (a) L. Wang, S. D. Fried, S. G. Boxer and T. E. Markland, Quantum delocalization of protons in the hydrogen-bond network of an enzyme active site, *Proc. Natl. Acad. Sci. U. S. A.*, 2014, **111**, 18454–18459; (b) S. Sappati, A. Hassanali, R. Gebauer and P. Ghosh, Nuclear quantum effects in a HIV/cancer inhibitor: The case of ellipticine, *J. Chem. Phys.*, 2016, **145**, 205102.
- 25 (a) P. G. Wenthold and R. R. Squires, Bond Dissociation Energies of F₂[−] and HF₂[−]. A Gas-Phase Experimental and G2 Theoretical Study, *J. Phys. Chem.*, 1995, **99**, 2002–2005; (b) C. Stein, R. Oswald, P. Sebald, P. Botschwina, H. Stoll and K. A. Peterson, Accurate bond dissociation energies (D-0) for FHF[−] isotopologues, *Mol. Phys.*, 2013, **111**, 2647–2652.
- 26 K. Kawaguchi and E. Hirota, Infrared diode laser study of the hydrogen bifluoride anion: FHF[−] and FDF[−], *J. Chem. Phys.*, 1986, **84**, 2953–2960.
- 27 K. Kawaguchi and E. Hirota, Diode laser spectroscopy of the ν_3 and ν_2 bands of FHF[−] in 1300 cm^{−1} region, *J. Chem. Phys.*, 1987, **87**, 6838–6841.
- 28 K. Kawaguchi and E. Hirota, Infrared diode laser spectroscopy of FDF[−], *J. Mol. Struct.*, 1995, **352-353**, 389–394.
- 29 J. Almlöf, Hydrogen bond studies. 71. *Ab initio* calculation of the vibrational structure and equilibrium geometry in HF₂[−] and DF₂[−], *Chem. Phys. Lett.*, 1972, **17**, 49–52.
- 30 A. R. Ubbelohde, Structure and Thermal Properties Associated with Some Hydrogen Bonds in Crystals. III. Further Examples of the Isotope Effect, *Proc. R. Soc. A*, 1939, **173**, 417–427.
- 31 X.-Z. Li, B. Walker and A. Michaelides, Quantum nature of the hydrogen bond, *Proc. Natl. Acad. Sci. U. S. A.*, 2011, **108**, 6369–6373.
- 32 (a) R. D. Hunt and L. J. Andrews, FTIR spectra of the HF₂[−] and H₂F₃[−] anions isolated in solid argon and neon, *J. Chem. Phys.*, 1987, **87**, 6819–6823; (b) S. A. McDonald and L. J. Andrews, Infrared spectrum and structure of the isolated HF₂[−] ion in solid argon, *Chem. Phys.*, 1979, **70**, 3134–3136; (c) B. S. Ault, *J. Phys. Chem.*, 1979, **83**, 837–844.



- 33 P. Dawson, Spectroscopic detection of the hydrogen bond isotope effect in KHF_2 , *J. Chem. Soc., Faraday Trans. 2*, 1972, **68**, 1448–1451.
- 34 P. Schah-Mohammadi, I. G. Shenderovich, C. Detering, H.-H. Limbach, P. M. Tolstoy, S. N. Smirnov, G. S. Denisov and N. S. Golubev, Hydrogen/Deuterium Isotope Effects on NMR Chemical Shifts of Formally Symmetric Complexes with a Strong Intermolecular Hydrogen Bond in Liquid Solutions at 100–150 K, *J. Am. Chem. Soc.*, 2000, **122**, 12878–12879.
- 35 I. Shenderovich, S. Smirnov, G. S. Denisov, V. Gindin, N. S. Golubev, A. Dunger, R. Reibke, S. Kirpekar, O. L. Malkina and H. H. Limbach, Nuclear Magnetic Resonance of Hydrogen Bonded Clusters between F^- and $(\text{HF})_n^-$: Experiment and Theory, *Ber. Bunsenges. Phys. Chem.*, 1998, **102**, 422–428.
- 36 I. G. Shenderovich, P. M. Tolstoy, N. S. Golubev, S. N. Smirnov, G. S. Denisov and H.-H. Limbach, Low-Temperature NMR Studies of the Structure and Dynamics of a Novel Series of Acid-Base Complexes of HF with Collidine Exhibiting Scalar Couplings Across Hydrogen Bonds, *J. Am. Chem. Soc.*, 2003, **125**, 11710–11720.
- 37 Y. Cornaton and R. Marquardt, A Global Analytical Representation of the Potential Energy Surface of the FHF^- Anion, *J. Phys. Chem. A*, 2016, **120**, 5959–5968.
- 38 P. Sebald, A. Bargholz, R. Oswald, C. Stein and P. Botschwina, FHF^- Isotopologues: Highly Anharmonic Hydrogen-Bonded Systems with Strong Coriolis Interaction, *J. Phys. Chem. A*, 2013, **117**, 9695–9703.
- 39 N. Elghobashi and L. Gonzalez, A theoretical anharmonic study of the infrared absorption spectra of FHF^- , FDF^- , OHF^- , and ODF^- anions, *J. Chem. Phys.*, 2006, **124**, 174308/1–12.
- 40 G. Perez-Hernandez, J. Gonzalez-Vazquez and L. Gonzalez, IR Spectrum of FHF^- and FDF^- Revisited Using a Spectral Method in Four Dimensions, *J. Phys. Chem. A*, 2012, **116**, 11361–11369.
- 41 S. Hirata, K. Yagi, S. A. Perera, S. Yamazaki and K. Hirao, Anharmonic vibrational frequencies and vibrationally averaged structures and nuclear magnetic resonance parameters of FHF^- , *J. Chem. Phys.*, 2008, **128**, 214305.
- 42 J. Li, X. Li and S. S. Iyengar, Vibrational Properties of Hydrogen-Bonded Systems Using the Multireference Generalization to the “On-the-Fly” Electronic Structure within Quantum Wavepacket *ab Initio* Molecular Dynamics (QWAIMD), *J. Chem. Theory Comput.*, 2014, **10**, 2265–2280.
- 43 A. M. Panich, NMR study of the $\text{F-H}\cdots\text{F}$ hydrogen bond. Relation between hydrogen atom position and $\text{F-H}\cdots\text{F}$ bond length, *Chem. Phys.*, 1995, **196**, 511–519.
- 44 J. Guo, P. M. Tolstoy, B. Koeppel, N. S. Golubev, G. S. Denisov, S. N. Smirnov and H.-H. Limbach, Hydrogen Bond Geometries and Proton Tautomerism of Homo-Conjugated Anions of Carboxylic Acids Studied *via* H/D Isotope Effects on ^{13}C NMR Chemical Shifts, *J. Phys. Chem. A*, 2012, **116**, 11180–11188.
- 45 (a) J. E. Del Bene, I. Alkorta and J. Elguero, A systematic comparison of second-order polarization propagator approximation (SOPPA) and equation-of-motion coupled cluster singles and doubles (EOM-CCSD) spin-spin coupling constants for selected singly bonded molecules, and the Hydrides NH_3 , H_2O , and HF and their protonated and deprotonated ions and hydrogen-bonded complexes, *J. Chem. Theory Comput.*, 2008, **4**, 967–973; (b) J. E. Del Bene, M. J. T. Jordan, S. A. Perera and R. J. Bartlett, Vibrational effects on the F-F spin-spin coupling constant ($^{2h}J(\text{F-F})$) in FHF^- and FDF^- , *J. Phys. Chem. A*, 2001, **105**, 8399–8402.
- 46 N. S. Golubev, S. M. Melikova, D. N. Shchepkin, I. G. Shenderovich, P. M. Tolstoy and G. S. Denisov, Interpretation of Hydrogen/Deuterium Isotope Effects on NMR Chemical Shifts of $[\text{FHF}]^-$ Ion Based on Calculations of Nuclear Magnetic Shielding Tensor Surface, *Z. Phys. Chem.*, 2003, **217**, 1549–1563.
- 47 N. S. Golubev, I. G. Shenderovich, P. M. Tolstoy and D. N. Shchepkin, Solvent induced temperature dependencies of NMR parameters of hydrogen bonded anionic clusters, *J. Mol. Struct.*, 2004, **697**, 9–15.
- 48 K. Suzuki, H. Ishibashi, K. Yagi, M. Shiga and M. Tachikawa, *Ab Initio* Path Integral Molecular Dynamics Simulations of F_2H^- and F_2H_3^+ , in *Quantum Systems in Chemistry and Physics*, ed. Nishikawa *et al.*, Springer Science, 2012, ch. 10, vol. 26.
- 49 T. Murakhtina, J. Heuft, E. J. Meijer and D. Sebastiani, First Principles and Experimental ^1H NMR Signatures of Solvated Ions: The Case of $\text{HCl}_{(\text{aq})}$, *ChemPhysChem*, 2006, **7**, 2578–2584.
- 50 S. O. Kang, D. Powell, V. W. Day and K. Bowman-James, Trapped Bifluoride, *Angew. Chem., Int. Ed.*, 2006, **45**, 1921–1925.
- 51 C. Mundy, F. Mohamed, F. Schiffman, G. Tabacchi, H. Forbert, W. Kuo, J. Hutter, M. Krack, M. Iannuzzi and M. McGrath, <http://www.cp2k.org/2000>.
- 52 G. Lippert, M. Parrinello and J. Hutter, A hybrid Gaussian and plane wave density functional scheme, *Mol. Phys.*, 1997, **92**, 477–488.
- 53 S. Grimme, Semiempirical GGA-type density functional constructed with a long-range dispersion correction, *J. Comput. Chem.*, 2006, **27**, 1787–1799.
- 54 A. D. Becke, Density-functional exchange-energy approximation with correct asymptotic behavior, *Phys. Rev. A: At., Mol., Opt. Phys.*, 1988, **38**, 3098–3100.
- 55 C. Lee, W. Yang and R. G. Parr, Development of the Colle-Salvetti correlation-energy formula into a functional of the electron density, *Phys. Rev. B: Condens. Matter Mater. Phys.*, 1988, **37**, 785–789.
- 56 J. VandeVondele and J. Hutter, Gaussian basis sets for accurate calculations on molecular systems in gas and condensed phases, *J. Chem. Phys.*, 2007, **127**, 114105.
- 57 S. Goedecker, M. Teter and J. Hutter, Separable dual-space Gaussian pseudopotentials, *Phys. Rev. B: Condens. Matter Mater. Phys.*, 1996, **54**, 1703–1710.
- 58 G. Bussi, D. Donadio and M. Parrinello, Canonical sampling through velocity rescaling, *J. Chem. Phys.*, 2007, **126**, 014101/1.
- 59 D. Marx and J. Hutter, in *Modern Methods and Algorithms of Quantum Chemistry*, ed. J. Grotendorst, NIC Series, 2000, vol. 1, p. 328.
- 60 W. Humphrey, A. Dalke and K. Schulten, VMD: Visual molecular dynamics, *J. Mol. Graphics*, 1996, **14**, 33–38.



- 61 M. Brehm and B. Kirchner, TRAVIS – A Free Analyzer and Visualizer for Monte Carlo and Molecular Dynamics Trajectories, *J. Chem. Inf. Model.*, 2011, **51**, 2007–2023.
- 62 M. Thomas, M. Brehm, R. Fligg, P. Voehringer and B. Kirchner, Computing vibrational spectra from *ab initio* molecular dynamics, *Phys. Chem. Chem. Phys.*, 2013, **15**, 6608–6622.
- 63 G. Lippert, J. Hutter and M. Parrinello, The Gaussian and augmented-plane-wave density functional method for *ab initio* molecular dynamics simulations, *Theor. Chem. Acc.*, 1999, **103**, 124–140.
- 64 V. Weber, M. Iannuzzi, S. Giani, J. Hutter, R. Declerck and M. Waroquier, Magnetic linear response properties calculations with the Gaussian and augmented-plane-wave method, *J. Chem. Phys.*, 2009, **131**, 014106.
- 65 C. Adamo and V. Barone, Toward reliable density functional methods without adjustable parameters: The PBE0 model, *J. Chem. Phys.*, 1999, **110**, 6158–6170.
- 66 K. L. Schuchardt, B. T. Didier, T. Elsethagen, L. Sun, V. Gurumoorthi, J. Chase, J. Li and T. L. Windus, Basis Set Exchange: A Community Database for Computational Sciences, *J. Chem. Inf. Model.*, 2007, **47**, 1045–1052.
- 67 D. Feller, The role of databases in support of computational chemistry calculations, *J. Comput. Chem.*, 1996, **17**, 1571–1586.
- 68 W. Kutzelnigg, U. Fleischer and M. Schindler, *Deuterium and Shift Calculation*, Springer, Berlin, Heidelberg, 1991, vol. 23, p. 165.
- 69 I. G. Shenderovich, H.-H. Limbach, S. N. Smirnov, P. M. Tolstoy, G. S. Denisov and N. S. Golubev, H/D Isotope Effects on the Low-Temperature NMR Parameters and Hydrogen Bond Geometries of $(\text{FH})_2\text{F}^-$ and $(\text{FH})_3\text{F}^-$ dissolved in $\text{CDF}_3/\text{CDF}_2\text{Cl}$, *Phys. Chem. Chem. Phys.*, 2002, **4**, 5488–5497.
- 70 T. Steiner, Lengthening of the Covalent X-H Bond in Heteronuclear Hydrogen Bonds Quantified from Organic and Organometallic Neutron Crystal Structures, *J. Phys. Chem. A*, 1998, **102**, 7041–7052.
- 71 H.-H. Limbach, M. Pietrzak, H. Benedict, P. M. Tolstoy, N. S. Golubev and G. S. Denisov, Empirical corrections for anharmonic zero-point vibrations of hydrogen and deuterium in geometric hydrogen bond correlations, *J. Mol. Struct.*, 2004, **706**, 115–119.
- 72 H.-H. Limbach, P. M. Tolstoy, N. Perez-Hernandez, J. Guo, I. G. Shenderovich and G. S. Denisov, OHO Hydrogen Bond Geometries and NMR Chemical Shifts: From Equilibrium Structures to Geometric H/D Isotope Effects with Applications for Water, Protonated Water and Compressed Ice, *Israel J. Chem.*, 2009, **49**, 199–216.
- 73 M. Thomas, M. Brehm, O. Hollóczki, Z. Kelemen, L. Nyulászi, T. Pasinszki and B. Kirchner, Simulating the vibrational spectra of ionic liquid systems: 1-ethyl-3-methylimidazolium acetate and its mixtures, *J. Chem. Phys.*, 2014, **141**, 024510.
- 74 S. Y. Kucherov, S. F. Bureiko and G. S. Denisov, Anti-cooperativity of FHF hydrogen bonds in clusters of the type $\text{F}^- \times (\text{HF})_n$, $\text{RF} \times (\text{HF})_n$ and $\text{XF} \times (\text{HF})_n$, R = alkyl and X = H, Br, Cl, F, *J. Mol. Struct.*, 2016, **1105**, 246–255.
- 75 (a) R. S. Rowland and R. Taylor, Intermolecular Nonbonded Contact Distances in Organic Crystal Structures: Comparison with Distances Expected from van der Waals Radii, *J. Phys. Chem.*, 1996, **100**, 7384–7391; (b) A. Bondi, van der Waals Volumes and Radii, *J. Phys. Chem.*, 1964, **68**, 441–451.
- 76 H.-H. Limbach, G. S. Denisov, I. G. Shenderovich and P. M. Tolstoy, Proton Tautomerism in Systems of Increasing Complexity: Examples from Organic Molecules to Enzymes, in *Tautomerism: Concepts and Applications in Science and Technology*, ed. L. Antonov, John Wiley and Sons, 2016.
- 77 S. B. Hakkert and M. Erdelyi, Halogen bond symmetry: the N–X–N bond, *J. Phys. Org. Chem.*, 2015, **28**, 226–233.



Molecular mechanism of Overhauser Dynamic Nuclear Polarization in
insulating solids

S. Pylaeva, K. L. Ivanov, M. Baldus, D. Sebastiani, and H. Elgabarty, *The Journal of Physical Chemistry Letters*, 2017, **8**, 2137.

Reprinted with permission from *J. Phys. Chem. Lett.*, 2017, 8 (10), pp 2137–2142. Copyright 2017 American Chemical Society.

DOI: 10.1021/acs.jpcllett.7b00561

Molecular Mechanism of Overhauser Dynamic Nuclear Polarization in Insulating Solids

Svetlana Pylaeva,[†] Konstantin L. Ivanov,^{‡,¶,§} Marc Baldus,[§] Daniel Sebastiani,[†] and Hossam Elgabarty^{*,†,ⓑ}

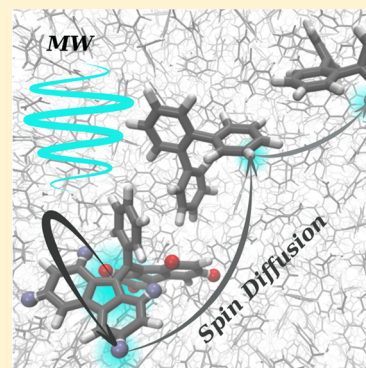
[†]Chemistry Department, MLU Halle–Wittenberg, 06120 Halle (Saale), Germany

[‡]International Tomography Center SB RAS, Novosibirsk 630090, Russia

[¶]Novosibirsk State University, Novosibirsk 630090, Russia

[§]NMR Spectroscopy, Bijvoet Center for Biomolecular Research, Utrecht University, 3584 CH Utrecht, The Netherlands

ABSTRACT: Dynamic nuclear polarization (DNP), a technique that significantly enhances NMR signals, is experiencing a renaissance owing to enormous methodological developments. In the heart of DNP is a polarization transfer mechanism that endows nuclei with much larger electronic spin polarization. Polarization transfer via the Overhauser effect (OE) is traditionally known to be operative only in liquids and conducting solids. Very recently, surprisingly strong OE-DNP in insulating solids has been reported, with a DNP efficiency that increases with the magnetic field strength. Here we offer an explanation for these perplexing observations using a combination of molecular dynamics and spin dynamics simulations. Our approach elucidates the underlying molecular stochastic motion, provides cross-relaxation rates, explains the observed sign of the NMR enhancement, and estimates the role of nuclear spin diffusion. The presented theoretical description opens the door for rational design of novel polarizing agents for OE-DNP in insulating solids.



Dynamic nuclear polarization (DNP) is a powerful method to overcome one of the major drawbacks of NMR spectroscopy—its low sensitivity.^{1–6} At the core of any DNP technique is a mechanism that transfers the much higher electronic spin polarization to a nuclear spin, thus hyperpolarizing the latter. The resulting NMR enhancements can be very high, ideally reaching the value $\epsilon_{\max} = \gamma_e/\gamma_N$ equal to the ratio of the electronic and nuclear gyromagnetic ratios, which is about 660 for protons and even higher for other nuclei. Particularly in the past decade, DNP-based nuclear hyperpolarization has seen revolutionary advances, which have given rise to a number of new applications.⁷ This renaissance of the technique has naturally invoked intense efforts into the theory of DNP,^{8–16} with the general aim of improving the technique, designing more efficient polarizing agents, and extending its scope to higher magnetic fields and temperatures.

Solid-state DNP has mostly relied on either the solid-effect^{9,17} or the cross-effect^{10,18,19} as the hyperpolarization mechanism. Both effects are known to scale unfavorably with increasing strength of the external magnetic field and also to decrease upon increasing temperature, most likely due to the decrease in electronic relaxation times. DNP-NMR is usually performed at temperatures of around 100 K, although DNP measurements at lower temperatures (down to 10 K)^{20,21} and at high temperatures²² are also feasible.

Another polarization transfer mechanism, which is actually the only one operative in liquid-state DNP, is the Overhauser effect (OE).^{23–25} Although the possibility of OE-DNP in insulating solids was discussed very early by Abragam,²⁶ the mechanism was conventionally deemed important only in low-

viscosity liquids. However, recently, Can et al.²⁷ have reported OE-DNP effects operative in insulating solids. The authors have investigated DNP with both deuterated and protonated BDPA (Figure 1) (α,γ -bisdiphenylene- β -phenylallyl) radical

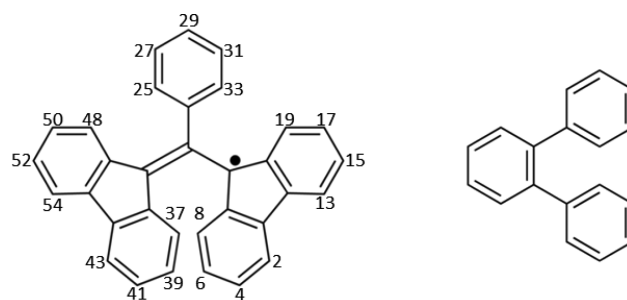


Figure 1. Structural formulas of the BDPA radical (left) and of OTP (right). Hydrogen atoms are omitted for clarity, and labels correspond to hydrogen atoms.

and the trityl OX063 radical embedded in a polystyrene matrix; the OE-DNP enhancement has been found only for BDPA and was shown to scale favorably with the magnetic field strength, that is, DNP enhancement increases in stronger magnetic fields. Lelli et al.²² further investigated this phenomenon for the BDPA radical in *ortho*-terphenyl (OTP, Figure 1) and

Received: March 7, 2017

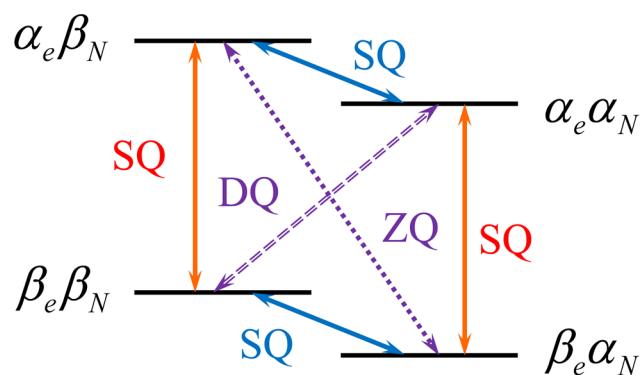
Accepted: April 26, 2017

Published: April 26, 2017

tetrachloroethane glassy matrix in a wide range of temperatures. Their findings revealed that a significant enhancement is preserved at temperatures as high as 240 K and that the enhancement is solvent-dependent. In fact, with OE enhancement, Lelli et al.²² obtained the largest DNP enhancement at high field (18.8 T) recorded to date.

The OE relies on a difference in rates of electron–nuclear zero-quantum (ZQ; flip–flip) and double-quantum (DQ; flip–flip) relaxation pathways (Scheme 1). Both types of

Scheme 1. Schematic Diagram of the OE in a Model System Comprised of an Electronic Spin Coupled to a Nuclear Spin^a



^aThe four-state spin system is represented as a direct product of the electronic and nuclear spin states: $\alpha_e, \beta_e, \alpha_N, \beta_N$. The four single-quantum (SQ) transitions are the allowed NMR and EPR transitions, while the ZQ and DQ cross-relaxation transitions are the ones responsible for OE.

cross-relaxation transitions are mediated by a fluctuating hyperfine interaction; the scalar hyperfine coupling (HFC) causes the ZQ transition (leading to a positive OE-DNP enhancement), whereas the dipolar HFC can cause both transitions (in the case of dipolar relaxation, the rates of the two transitions are different, usually leading to a negative OE-DNP enhancement). Thus, the relevant time correlation functions giving rise to the OE are those of the HFC

$$G_{l,m}(\tau) = \langle Y_{l,m}(t) Y_{l,m}^*(t + \tau) \rangle$$

$$J_{l,m}(\omega) = \int_{-\infty}^{+\infty} G_{l,m}(\tau) e^{i\omega\tau} d\tau$$

where the $Y_{l,m}$ are the spherical components of the HFC tensor, which is composed of a rank-zero part (the scalar coupling) and a rank-two part (the dipolar coupling).

For the fluctuations in the hyperfine tensor to be OE operative (i.e., to induce mutual relaxation transitions), they should exhibit time-dependent oscillations on a time scale comparable to $(\omega_e \pm \omega_N)^{-1} \approx \omega_e^{-1}$, where the ω 's are the Larmor frequencies of the electron and the hyperfine-coupled nucleus. The latter condition means that ideally the correlation time should be on the order of 10^{-11} to 10^{-12} seconds. In noninsulating solids, the conduction electrons provide the fast dynamics that facilitate OE. In insulating solids, however, molecular motion is almost never that fast and OE is usually deemed insignificant. To the best of our knowledge, the origin of the cross-relaxation mechanism responsible for the OE observed with BDPA in insulating solids remains unknown. Likewise, it is not clear which radical systems would provide

significant OE-DNP. The increased DNP enhancement upon increasing field has not been explained either. For all of these reasons, there is no rational strategy available for optimizing OE-DNP in solids to improve its performance.

Here, we present a theoretical investigation of OE-DNP in insulating solids. We have addressed this problem by a combination of computer simulation methods: classical and ab initio molecular dynamics (MD) simulations combined with spin dynamics (SD) simulations. Specifically, our aims were (1) to identify the molecular motion(s) responsible for the time dependence in the HFC and hence OE-DNP and (2) to pinpoint the particular structural properties of the BDPA radical that facilitate OE in contrast to other radicals where no effect was observed, for example, trityl radicals. As we demonstrate in this Letter, the origin of the observed OE-DNP lies in the low-frequency modes of BDPA and their couplings to the solvent bath. Specifically, these geometric fluctuations cause corresponding fluctuations in a spin density that is spread over a conjugated aromatic system. Importantly, such vibrational fluctuations are operative even in a solid matrix at low temperature, making solid-state OE-DNP feasible. SD simulations based on the spectral density extracted from MD trajectories show that the obtained estimates of the cross-relaxation rates are consistent, allowing us to simulate polarization of local nuclei as well as polarization of remote “bulk” nuclei, polarized by means of spin diffusion.

Altogether, we are able to model the phenomenon of OE-DNP in insulating solids using a joint approach combining molecular dynamics simulations with SD-based estimates of DNP enhancements. Analysis of the MD results paves the way to understanding which structural features to incorporate when designing new radicals suitable for OE-DNP in solids.

As already mentioned, in the heart of any OE-mediated DNP, there must be a fluctuation of the HFC with a correlation time on the order of the reciprocal of the electronic Larmor frequency. Moreover, the experimentally observed nuclear polarization requires a HFC that is not vanishingly small. MD-averaged proton HFC tensor components are presented in Table 1 for both cases: in vacuum (from ab initio MD) and in a frozen OTP glassy matrix (force field MD). We have partitioned the BDPA protons in six groups in a manner such as to maximize the correspondence with the six HFCs that were obtained from line shape simulations of the liquid-state

Table 1. MD-Averaged Proton HFC Tensor Components^a

group/ color	A , Exp. (MHz)	A , vacuum (MHz)	A , OTP (MHz)	D , vacuum (MHz)	D , OTP (MHz)	H number
A (red)	-5.54	-4.35	-4.49	0.84	1.06	4,8,15,19
B (blue)	-5.29	-4.17	-5.61	0.81	1.25	37,41,48,52
C	1.38	0.71	0.94	0.27	0.28	2,6,13,17
D	1.09	0.68	0.86	0.27	0.34	39,43,50,54
E	-0.5	0.33	0.88	0.42	0.50	25,29,33
F	-0.15	0.2	-0.12	0.14	0.17	27,31

^aVariables: A : isotropic coupling; D : one fifth of the Frobenius norm of the rank-two spherical tensor. Vacuum values were sampled from the an ab initio MD trajectory, while values from frozen OTP glass were obtained from the classical MD trajectory, as detailed in the Methods section. The A/B (red/blue) protons are marked in Figure 2a, and the proton positions are enumerated in Figure 1. Experimental values were taken from Can et al.²⁷

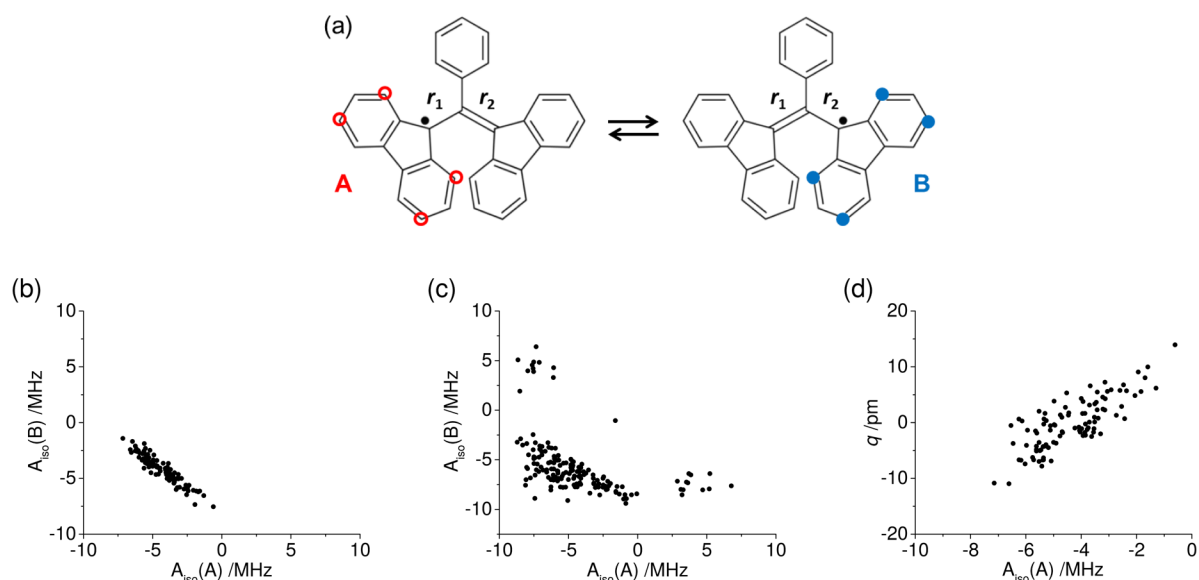


Figure 2. (a) Two *inequivalent* BDPA structures; only proton positions with the highest values of the isotropic HFC (corresponding to groups A and B in Table 1) are marked. (b,c) Interdependence of isotropic HFC constants of A and B groups in vacuum (b) and in the frozen OTP matrix (c). (d) Correlation between the reaction coordinate $q = r_1 - r_2$ and the isotropic HFCs of group A protons in vacuum.

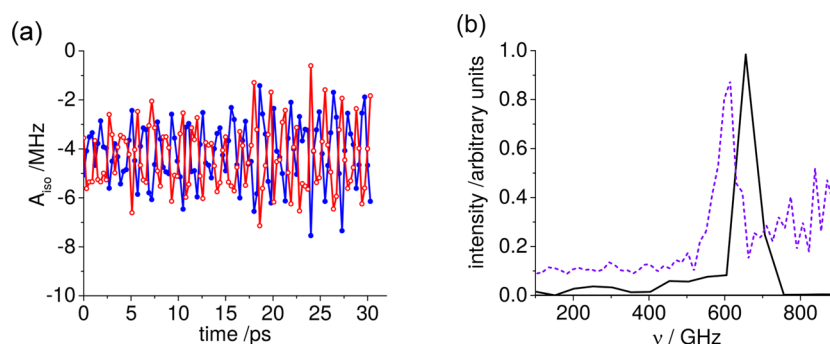


Figure 3. (a) Time evolution of the average isotropic HFC constants of the protons in groups A (red, open circles) and B (blue, solid circles) along the trajectory in vacuum (cf. Figure 2a). (b) Frequency spectrum of the asymmetry parameter $q = r_1 - r_2$ fluctuations. The black line is from the vacuum ab initio MD trajectory, and the purple dotted line is from the classical MD trajectory (frozen OTP matrix). Note that the dotted line is not shifted; the intensity in the range of 100–500 GHz depicts a broadened signal.

EPR spectrum of BDPA.²⁷ While this partitioning is not fully unambiguous, it provides good grounds for discussing the results, and as we will show later, it is consistent with the fluctuation patterns revealed by MD simulations.

By far, the strongest HFCs reside on the protons at the 1, 3, 6, and 8 positions of the fluorene moieties in BDPA (groups A/B in Table 1). These atoms are marked with red/blue in Figure 2a and occupy identical positions on the opposite fluorene groups. It is also clear from the table that in these two groups of protons the average of any component of the anisotropic HFC tensor is much weaker than the isotropic component. The time evolution of the average isotropic HFC of each of the two groups of protons in vacuum is depicted in Figure 3a. It is notable that the fluctuations exhibited by the scalar HFCs in each moiety are perfectly out of phase with those in the other one. Moreover, we found that in vacuum a negative linear correlation between couplings of both groups is very apparent (Figure 2b). In frozen OTP, the general correlation trend is preserved (Figure 2c), and expectedly, the correlation is noisier and exhibits some outliers with positive isotropic HFCs.

The out-of-phase fluctuations in the isotropic HFC constants imply an out-of-phase fluctuation in the spin density at these A/

B protons on the opposing fluorene moieties as well. Already, the periodicity of the fluctuations suggests an underlying vibrational mode in BDPA. Indeed, these spin density fluctuations can be best understood in terms of structural fluctuations between the two structures depicted in Figure 2a. This structural fluctuation can be captured in the dynamics of a single coordinate $q = r_1 - r_2$, where r_1 and r_2 are the bond lengths connecting the central carbon atom to the fluorene moieties. The fluctuations in q can be pictorially described as fluctuations between two alternating structures with a flipping in the bond orders. It should be noted that these two structures *are not* resonance structures as the geometry of BDPA is never planar. Plotting q against the scalar couplings of group A (or equivalently group B) protons indeed confirms the relationship (Figure 2d).

The large amplitude of the fluctuations in the HFC in response to small fluctuations in q (linear regression gives a slope of 0.12 MHz/pm) is a consequence of the delocalized electron density distribution at the two diphenylene moieties of BDPA and of the allylic bridge between them. Moreover, frequency analysis of the fluctuations of q in vacuum reveals that they are in the GHz range, with a maximal intensity at circa

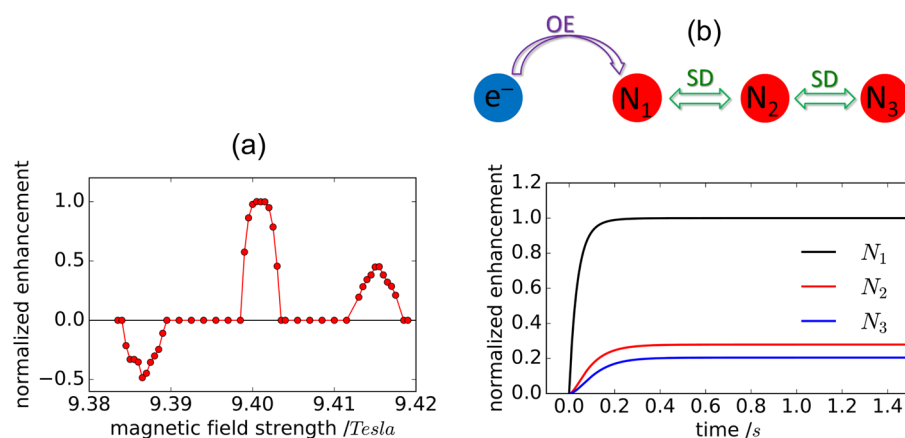


Figure 4. (a) Calculated magnetic field dependence of the DNP effect for $\omega_{\text{MW}} = 263.5$ GHz upon a sweep of the external magnetic field. The outer components in the “DNP spectrum” come from the solid-effect contribution, whereas the central component is due to OE-DNP. Parameters of the calculation are given in the [Methods](#) section. (b) Simulation of spin diffusion in OE-DNP; the time dependence of nuclear polarization of nuclei is shown. The spin system consists of one electron spin and three nuclear spins; OE-DNP is operative only for the N_1 nucleus nearest to the electron, whereas the N_2 and N_3 nuclei are polarized by spin diffusion. The field is tuned to the central component of the DNP spectrum. Other parameters of the calculation are given in the [Methods](#) section.

650 GHz (Figure 3b). In the frozen OTP matrix, the peak shifts to ~ 600 GHz, with the appearance of a nonvanishing spectral density in the 100–500 GHz range as well. Notably, ω_e falls into the same range: 140 GHz for 5 T, 263 GHz for 9.4 T, 395 GHz for 14.1 T, and 527 GHz for 18.8 T with the NMR spectrometer. Thus, our simulations reveal that there is indeed a sizable spectral density of the fluctuating HFC in the required range, facilitating DQ and ZQ cross-relaxation transitions. The vibrational nature of the oscillation in q means that it is active even at very low temperatures. Interestingly, fluctuations of the q peak at higher frequencies, which can offer an explanation for the experimentally observed increase in OE-DNP efficiency in this system at higher fields.²⁷ The stronger amplitude of the fluctuating scalar interactions (in contrast to dipolar couplings) also provides favorable conditions for OE-DNP at high fields because scalar HFC can only induce the ZQ relaxation process and not the SQ processes, that is, nuclear T_1 relaxation. An enhancement of the latter would reduce the resulting DNP efficiency. This is also in agreement with experimental findings, where a *positive* enhancement was found with protonated BDPA, but a *weaker and negative* enhancement was found in the case of deuterated BDPA.

For the simplest two-spin model depicted in [Scheme 1](#) (one electron and one nucleus), we have used SD simulations to calculate the DNP efficiency for a field sweep around 9.4 GHz at a fixed MW frequency of 263.5 GHz. The resulting field dependence of the enhancement, that is, the “DNP spectrum”, exhibits three features (Figure 4a). The two outer features (a negative and a positive one) come from solid-effect DNP; these features emerge upon pumping the forbidden EPR transitions and are shifted by the nuclear Larmor frequency ω_N from the center of the spectrum. The feature in the center emerging upon pumping on EPR resonance comes from OE-DNP. This feature is positive as only the ZQ relaxation was taken into account (which is the case for fluctuating scalar HFC). The DNP spectrum pattern agrees with that reported earlier (e.g., Figure S1 in ref 22).

We have also simulated effects of spin diffusion. Such a consideration is critical as OE-DNP acts exclusively on local nuclei of BDPA, whereas only bulk nuclei can be observed in NMR experiments (and are in fact the intended target of the

enhancement). These distant nuclei are not coupled directly to the electron and thus can be polarized solely indirectly by polarization transfer from local nuclei, that is, by nuclear spin diffusion. To model spin diffusion, we have considered a system with three nuclei: one nucleus is coupled to the electron and is polarized directly, and the other two acquire polarization via dipole–dipole interactions. We located four spins on a chain and assumed that each spin is coupled to only its nearest neighbors, as depicted in [Figure 4b](#). As expected, polarization of the local nucleus is the strongest at all times. However, other nuclei still acquire some nonthermal polarization by spin diffusion. Again, this is in agreement with the reported NMR experiments where sizable OE-DNP enhancements for bulk nuclei have been reported.²²

To summarize, we have revealed the molecular origin of the recently reported OE-DNP in insulating solids. Unlike liquid OE-DNP where fluctuations in the HFC are due to solvent dynamics, here the fluctuations have their origin in a superposition of local low-frequency modes in the radical itself and their coupling and broadening due to a solvent bath. These geometric fluctuations in turn cause corresponding fluctuations in the spin density at the radical’s protons. Both effects can be traced back to specific structural features: the two conjugated diphenylene moieties with their delocalized spin densities, the oscillating allylic bridge joining them, and of course the presence of structural protons in BDPA. The trytil radical, which failed to exhibit OE-DNP, has neither protons nor this strong dependence of the spin density on structural fluctuations. These findings already suggest a rationale for structural modifications that would render BDPA a more efficient DNP polarization agent. One approach would be to reduce the peak frequency of the structural fluctuations by increasing the masses of the fluorene moieties, for example, using massive substituents at the 2, 4, 5, or 7 positions of the fluorene (thus leaving intact the set of strong hyperfine-coupled protons). Electron-donating substituents could possibly offer an additional advantage by enhancing the spin density.

The conclusions based on this model and the ensuing spectral density are consistent with the reported experimental findings. The relative magnitudes of the scalar vs dipolar HFCs reveal that the former is dominant, as found experimentally.

The importance of structural protons in BDPA is also explained, and the frequency dependence of the spectral density suggests a possible explanation for the OE-DNP field dependence. SD calculations predict sizable OE-DNP originating from ZQ cross-relaxation and estimate the role of nuclear spin diffusion from structural BDPA protons to bulk protons.

METHODS

Molecular Dynamics. Classical MD Simulations. Classical molecular dynamics simulations were performed using GROMACS 5.11²⁸ employing the Gromos53a6 force field.²⁹ Starting parameters for BDPA were downloaded from the ATB repository.³⁰ We reparametrized the stretching and torsional terms involving the central carbon by fitting to BLYP-D3 DFT calculations (setup described below). Simulations of a 32 mM solution of BDPA in OTP were done under the *NPT* ensemble in a cubic periodic box containing one molecule of BDPA. The system was simulated at room temperature (300 K) and pressure for 75 ns. Following this, the system was annealed down to 240 K over 1.1 ns, followed by 500 ps production for sampling the HFC tensors. Sequential snapshots were extracted from the production segment every 0.3 ps for calculation of HFC tensors.

Ab Initio Molecular Dynamics Simulations. A single BDPA molecule was simulated in a cubic periodic box with a side length of 27 Å, using the Gaussian-and-plane-waves method GPW³¹ and the BLYP-D3 density functional,^{32,33} a 400 Ry energy cutoff, combined with an accurate triple- ζ basis set with two sets of polarization functions,^{34,35} with a time step of 0.4 fs. All ab initio simulations were performed using CP2K.³⁶ The initial 6 ps were run under massive thermostating using the Nosé–Hoover³⁷ thermostat and a coupling time of 30 fs. The production part of the trajectory was run without thermostating (*NVE* ensemble) with a total length of 31 ps. Snapshots were extracted every 0.3 ps and used to calculate the HFC.

Calculation of Hyperfine Coupling Tensors. Trajectory snapshots for calculating the HFC tensors were extracted regularly every 0.3 ps from the production segment of each trajectory (both the annealed classical trajectory and the ab initio trajectory). Calculations were performed in CP2K using the all-electron GAPW method,^{38,39} at a plane wave cutoff of 400 Ry, and the BLYP exchange correlation functional. A locally dense basis set was employed, with the EPR-III basis⁴⁰ for the hydrogen atoms and the Pople 6-31G* basis for carbon atoms.

Spin Dynamics. To gain insight into the mechanism of OE-DNP formation, we supported molecular dynamics by SD calculations. For these reasons, a program developed by some of us¹⁵ was modified for modeling DNP under magic angle spinning (MAS) conditions. We considered a spin system comprising an electron and up to three spin-1/2 nuclei. The Hamiltonian of such a system in the MW-rotating frame is as follows:

$$\hat{H}(t) = (\omega_e - \omega_{\text{MW}})\hat{S}_z + \omega_1\hat{S}_x - \omega_N \sum_k \hat{I}_{kz} + \sum_k \hat{S}\hat{A}_k\hat{I}_k + \sum_{k<m} \hat{I}_k\hat{D}_{km}\hat{I}_m \quad (1)$$

where ω_e is the Zeeman interaction of the electron spin, ω_{MW} is the MW frequency, ω_1 is the MW field strength, ω_N is the nuclear Zeeman interaction, \hat{A}_k is the hyperfine interaction tensor for the k th nucleus, and \hat{D}_{km} is the dipolar interaction

tensor for the k th and m th spins. As usual, \hat{S} and \hat{I}_k stand for the spin operators of the electron and nuclei. The Hamiltonian is time-dependent due to sample spinning and orientation-dependent ω_e , \hat{A}_k , and \hat{D}_{km} . Consequently, the MW pumping is not performed continuously on resonance but is rather occurring during “rotor events” at the instants of time when $\omega_e \approx \omega_{\text{MW}}$.²⁷ This leads to partial excitation of the EPR transition and to a shift of the electron spin magnetization away from equilibrium. Solid-effect DNP occurs at rotor events when $\omega_e \pm \omega_N \approx \omega_{\text{MW}}$ and forbidden EPR transitions are excited. Polarization transfer during rotor events is explicitly taken into account in our treatment. We considered polarization transfer between nuclei–spin diffusion, which is due to nuclear dipole–dipole interactions. Because relaxation effects are crucial for DNP formation, we took into account the electronic longitudinal and transverse relaxation (the corresponding relaxation times are denoted as T_{1e} and T_{2e}), cross-relaxation occurring at rates $1/T_{\text{ZQ}}$ and $1/T_{\text{DQ}}$ (for the ZQ and DQ transitions, respectively), and nuclear longitudinal relaxation with the time T_{1N} . The cross-relaxation rates were estimated from MD results as product $|A|^2 J(\omega)$; here, A is the matrix element of the fluctuating Hamiltonian for the corresponding transition and $J(\omega)$ is the spectral density at the transition frequency ω . In our SD calculations, we computed the evolution superoperator for the density matrix of the spin system, which describes the spin evolution over one MAS period, $T_{\text{MAS}} = 1/\nu_{\text{MAS}}$. After that, the density matrix was propagated over subsequent rotor periods until steady state was reached. We also performed averaging over different orientations of the radical with respect to the rotor-fixed frame.⁴¹ Typical parameters used in the simulation were as follows: MW frequency $\omega_{\text{MW}} = 2\pi \cdot 263.5$ GHz, MW field strength $\omega_1 = 2\pi \cdot 1$ MHz, isotropic g -factor 2.0026, g -anisotropy 0.005, isotropic HFC constant $A_{\text{iso}} = 2\pi \cdot 4$ MHz, dipolar HFC constant $A_{zz} = 2\pi \cdot 1$ MHz, and MAS frequency $\omega_{\text{MAS}} = 2\pi \cdot 10$ kHz. In all simulations, all nuclei were protons. Relaxation parameters were $T_{1e} = 10^{-3}$ s; $T_{2e} = 4 \times 10^{-6}$ s; $T_{1N} = 0.1$ s; $T_{2N} = 2 \times 10^{-4}$ s; $1/T_{\text{ZQ}} = 10$ s⁻¹; and $1/T_{\text{DQ}} = 0$. The estimate for T_{ZQ} follows the MD results; it has been taken to be equal to the product of $\langle A \rangle^2$ and the noise spectral density at the EPR frequency, $J(\omega_{\text{MW}})$. Here, $\langle A \rangle$ is the typical value of the scalar HFC of the red and blue groups of BDPA’s protons; see Table 1. To model spin diffusion, we assumed that the electron spin and nuclear spins are positioned on a line and set the distance between the nuclei equal to 3 Å, corresponding to a nuclear dipolar interaction of 4.4 kHz.

AUTHOR INFORMATION

Corresponding Author

*E-mail: hossam.elgabarty@chemie.uni-halle.de.

ORCID

Hossam Elgabarty: 0000-0002-4945-1481

Notes

The authors declare no competing financial interest.

ACKNOWLEDGMENTS

K.L.I. acknowledges support from the Russian Science Foundation (Grant No. 15-13-20035); S.P., H.E., and D.S. acknowledge support from DFG (Grant Se1008/12-1); and M.B. gratefully acknowledges financial support by an NWO VICI grant (Grant Number 700.100.443). The authors thank

Dr. Andrey Gurinov for support in running SD simulations and fruitful discussions.

REFERENCES

- (1) Maly, T.; Debelouchina, G. T.; Bajaj, V. S.; Hu, K.-N.; Joo, C.-G.; Mak-Jurkauskas, M. L.; Sirigiri, J. R.; van der Wel, P. C. A.; Herzfeld, J.; Temkin, R. J.; et al. Dynamic Nuclear Polarization at High Magnetic Fields. *J. Chem. Phys.* **2008**, *128*, 052211.
- (2) Griffin, R. G.; Prisner, T. F. High Field Dynamic Nuclear Polarization—the Renaissance. *Phys. Chem. Chem. Phys.* **2010**, *12*, 5737.
- (3) Ni, Q. Z.; Daviso, E.; Can, T. V.; Markhasin, E.; Jawla, S. K.; Swager, T. M.; Temkin, R. J.; Herzfeld, J.; Griffin, R. G. High Frequency Dynamic Nuclear Polarization. *Acc. Chem. Res.* **2013**, *46*, 1933–1941.
- (4) Ardenkjaer-Larsen, J. H.; Fridlund, B.; Gram, A.; Hansson, G.; Hansson, L.; Lerche, M. H.; Servin, R.; Thaning, M.; Golman, K. Increase in Signal-to-noise Ratio of > 10,000 Times in Liquid-state NMR. *Proc. Natl. Acad. Sci. U. S. A.* **2003**, *100*, 10158–10163.
- (5) Gajan, D.; Bornet, A.; Vuichoud, B.; Milani, J.; Melzi, R.; van Kalker, H. A.; Veyre, L.; Thieuleux, C.; Conley, M. P.; Grüning, W. R.; et al. Hybrid Polarizing Solids for Pure Hyperpolarized Liquids through Dissolution Dynamic Nuclear Polarization. *Proc. Natl. Acad. Sci. U. S. A.* **2014**, *111*, 14693–14697.
- (6) Chen, H. Y.; Ragavan, M.; Hilty, C. Protein Folding Studied by Dissolution Dynamic Nuclear Polarization. *Angew. Chem., Int. Ed.* **2013**, *52*, 9192–9195.
- (7) Jeschke, G.; Frydman, L. Nuclear Hyperpolarization Comes of Age. *J. Magn. Reson.* **2016**, *264*, 1–2.
- (8) Farrar, C. T.; Hall, D. A.; Gerfen, G. J.; Inati, S. J.; Griffin, R. G. Mechanism of Dynamic Nuclear Polarization in High Magnetic Fields. *J. Chem. Phys.* **2001**, *114*, 4922–4933.
- (9) Hovav, Y.; Feintuch, A.; Vega, S. Theoretical Aspects of Dynamic Nuclear Polarization in the Solid State - The Solid Effect. *J. Magn. Reson.* **2010**, *207*, 176–189.
- (10) Hovav, Y.; Feintuch, A.; Vega, S. Theoretical Aspects of Dynamic Nuclear Polarization in the Solid State - The Cross Effect. *J. Magn. Reson.* **2012**, *214*, 29–41.
- (11) Hu, K.-N.; Debelouchina, G. T.; Smith, A. A.; Griffin, R. G. Quantum Mechanical Theory of Dynamic Nuclear Polarization in Solid Dielectrics. *J. Chem. Phys.* **2011**, *134*, 125105.
- (12) Mentink-Vigier, F.; Akbey, Ü.; Hovav, Y.; Vega, S.; Oschkinat, H.; Feintuch, A. Fast Passage Dynamic Nuclear Polarization on Rotating Solids. *J. Magn. Reson.* **2012**, *224*, 13–21.
- (13) Thurber, K. R.; Tycko, R. Theory for Cross Effect Dynamic Nuclear Polarization under Magic-angle Spinning in Solid State Nuclear Magnetic Resonance: The Importance of Level Crossings. *J. Chem. Phys.* **2012**, *137*, 084508.
- (14) Thurber, K. R.; Tycko, R. On Mechanisms of Dynamic Nuclear Polarization in Solids. *Isr. J. Chem.* **2014**, *54*, 39–46.
- (15) Mance, D.; Gast, P.; Huber, M.; Baldus, M.; Ivanov, K. L. The Magnetic Field Dependence of Cross-effect Dynamic Nuclear Polarization under Magic Angle Spinning. *J. Chem. Phys.* **2015**, *142*, 234201.
- (16) Mentink-Vigier, F.; Akbey, Ü.; Oschkinat, H.; Vega, S.; Feintuch, A. Theoretical Aspects of Magic Angle Spinning - Dynamic Nuclear Polarization. *J. Magn. Reson.* **2015**, *258*, 102–120.
- (17) Jeffries, C. D. Polarization of Nuclei by Resonance Saturation in Paramagnetic Crystals. *Phys. Rev.* **1957**, *106*, 164–165.
- (18) Hwang, F.; Hill, D. A. Phenomenological Model for the New Effect in Dynamic Polarization. *Phys. Rev. Lett.* **1967**, *19*, 1011.
- (19) Hu, K.-N.; Yu, H.-h.; Swager, T. M.; Griffin, R. G. Dynamic Nuclear Polarization with Biradicals. *J. Am. Chem. Soc.* **2004**, *126*, 10844–10845.
- (20) Matsuki, Y.; Idehara, T.; Fukazawa, J.; Fujiwara, T. Advanced Instrumentation for DNP-enhanced MAS NMR for Higher Magnetic Fields and Lower Temperatures. *J. Magn. Reson.* **2016**, *264*, 107–115.
- (21) Bouleau, E.; Saint-Bonnet, P.; Mentink-Vigier, F.; Takahashi, H.; Jacquot, J.-F.; Bardet, M.; Aussenac, F.; Pureau, A.; Engelke, F.; Hediger, S.; et al. Pushing NMR Sensitivity Limits Using Dynamic Nuclear Polarization with Closed-loop Cryogenic Helium Sample Spinning. *Chem. Sci.* **2015**, *6*, 6806–6812.
- (22) Lelli, M.; Chaudhari, S. R.; Gajan, D.; Casano, G.; Rossini, A. J.; Ouari, O.; Tordo, P.; Lesage, A.; Emsley, L. Solid-State Dynamic Nuclear Polarization at 9.4 and 18.8 T from 100 K to Room Temperature. *J. Am. Chem. Soc.* **2015**, *137*, 14558–14561.
- (23) Hauser, K.; Stehlik, D. *Advances in Magnetic Resonance*; Elsevier BV, 1968; Vol. 3; pp 79–139.
- (24) Loening, N. M.; Rosay, M.; Weis, V.; Griffin, R. G. Solution-State Dynamic Nuclear Polarization at High Magnetic Field. *J. Am. Chem. Soc.* **2002**, *124*, 8808–8809.
- (25) Griesinger, C.; Bennati, M.; Vieth, H.; Luchinat, C.; Parigi, G.; Höfer, P.; Engelke, F.; Glaser, S.; Denysenkov, V.; Prisner, T. Dynamic Nuclear Polarization at High Magnetic Fields in Liquids. *Prog. Nucl. Magn. Reson. Spectrosc.* **2012**, *64*, 4–28.
- (26) Abragam, A. Overhauser Effect in Nonmetals. *Phys. Rev.* **1955**, *98*, 1729–1735.
- (27) Can, T. V.; Caporini, M. A.; Mentink-Vigier, F.; Corzilius, B.; Walsh, J. J.; Rosay, M.; Maas, W. E.; Baldus, M.; Vega, S.; Swager, T. M.; et al. Overhauser Effects in Insulating Solids. *J. Chem. Phys.* **2014**, *141*, 064202.
- (28) Abraham, M. J.; Murtola, T.; Schulz, R.; Páll, S.; Smith, J. C.; Hess, B.; Lindahl, E. GROMACS: High Performance Molecular Simulations through Multi-level Parallelism from Laptops to Supercomputers. *SoftwareX* **2015**, *1–2*, 19–25.
- (29) Oostenbrink, C.; Villa, A.; Mark, A. E.; Van Gunsteren, W. F. A Biomolecular Force Field Based on the Free Enthalpy of Hydration and Solvation: The GROMOS Force-Field Parameter Sets 53A5 and 53A6. *J. Comput. Chem.* **2004**, *25*, 1656–1676.
- (30) Malde, A. K.; Zuo, L.; Breeze, M.; Stroet, M.; Poger, D.; Nair, P. C.; Oostenbrink, C.; Mark, A. E. An Automated Force Field Topology Builder (ATB) and Repository: Version 1.0. *J. Chem. Theory Comput.* **2011**, *7*, 4026–4037.
- (31) Lippert, G.; Hutter, J.; Parrinello, M. A hybrid Gaussian and Plane Wave Density Functional Scheme. *Mol. Phys.* **1997**, *92*, 477–488.
- (32) Grimme, S.; Antony, J.; Ehrlich, S.; Krieg, H. a Consistent and Accurate Ab Initio Parametrization of Density Functional Dispersion Correction (dft-d) for the 94 Elements H-Pu. *J. Chem. Phys.* **2010**, *132*, 154104.
- (33) Becke, A. D. Density-functional Exchange-energy Approximation with Correct Asymptotic Behavior. *Phys. Rev. A: At, Mol., Opt. Phys.* **1988**, *38*, 3098–3100.
- (34) Goedecker, S.; Teter, M.; Hutter, J. Separable Dual-space Gaussian Pseudopotentials. *Phys. Rev. B: Condens. Matter Mater. Phys.* **1996**, *54*, 1703–1710.
- (35) VandeVondele, J.; Hutter, J. Gaussian Basis Sets for Accurate Calculations on Molecular Systems in Gas and Condensed Phases. *J. Chem. Phys.* **2007**, *127*, 114105.
- (36) Hutter, J.; Iannuzzi, M.; Schiffrmann, F.; VandeVondele, J. cp2k: Atomistic Simulations of Condensed Matter Systems. *WIREs Comput. Mol. Sci.* **2014**, *4*, 15–25.
- (37) Hoover, W. Canonical Dynamics: Equilibrium Phase-space Distributions. *Phys. Rev. A: At, Mol., Opt. Phys.* **1985**, *31*, 1695–1697.
- (38) Lippert, G.; Hutter, J.; Parrinello, M. The Gaussian and Augmented-plane-wave Density Functional Method for Ab Initio Molecular Dynamics Simulations. *Theor. Chem. Acc.* **1999**, *103*, 124–140.
- (39) Weber, V.; Iannuzzi, M.; Giani, S.; Hutter, J.; Declerck, R.; Waroquier, M. Magnetic Linear Response Properties Calculations with the Gaussian and Augmented-plane-wave Method. *J. Chem. Phys.* **2009**, *131*, 014106.
- (40) Barone, V. In *Recent Advances in Density Functional Methods (Part I)*; Chong, D. P., Ed.; Recent Advances in Computational Chemistry; World Scientific, 1995; pp 287–334.
- (41) Baldus, M. Correlation Experiments for Assignment and Structure Elucidation of Immobilized Polypeptides under Magic Angle Spinning. *Prog. Nucl. Magn. Reson. Spectrosc.* **2002**, *41*, 1–47.

Salt bridge in aqueous solution: strong structural motifs but weak enthalpic effect

S. Pylaeva, M. Brehm, and D. Sebastiani, *Scientific Reports*, 2018, **8**, 13626.

Copyright The Author(s) 2018.

This article is licensed under a Creative Commons Attribution 4.0 International License
<http://creativecommons.org/licenses/by/4.0/>

DOI:10.1038/s41598-018-31935-z

SCIENTIFIC REPORTS



OPEN

Salt Bridge in Aqueous Solution: Strong Structural Motifs but Weak Enthalpic Effect

Svetlana Pylaeva, Martin Brehm  & Daniel Sebastiani 

Salt bridges are elementary motifs of protein secondary and tertiary structure and are commonly associated with structural driving force that increases stability. Often found on the interface to the solvent, they are highly susceptible to solvent–solute interactions, primarily with water but also with other cosolvents (especially ions). We have investigated the interplay of an Arginine–Aspartic acid salt bridge with simple salt ions in aqueous solution by means of molecular dynamics simulations. Besides structural and dynamical features at equilibrium, we have computed the mean force along the dissociation pathway of the salt bridge. We demonstrate that solvated ions influence the behavior of the salt bridge in a very specific and local way, namely the formation of tight ionic pairs $\text{Li}^+/\text{Na}^+ - \text{Asp}^-$. Moreover, our findings show that the enthalpic relevance of the salt bridge is minor, regardless of the presence of solvated ions.

Salt bridges are interactions of amino acids with opposite charge where at least two heavy atoms lie within a hydrogen bonding distance^{1,2}. Often found in solvent exposed parts of proteins, they are susceptible to external interactions, primarily with water. The Coulomb attraction of opposite charges is then screened by polar water molecules, and an outcome ranges from a contact ion pair to separately solvated ionic groups. This indicates that the relative strength of a salt bridge usually assumed to be around a couple of $k_B T$ and strongly depends on the environment^{1,3,4}. The Lysine–Glutamine salt bridge was investigated computationally in vacuum and in water in an attempt to model hydrophobic environment in protein core versus solvent accessible position⁵. It was shown that in a hydrophobic environment, the peptide is in a molecular form³, while upon addition of water molecules it switches to zwitterionic form, forming a salt bridge. However, the salt bridge is significantly weakened upon further hydration.

If one considers a realistic environment of proteins in a living cell, it contains not only water but different co-solvents, ions. And free ions in solution can further influence salt bridges by extra shielding of charges (unspecific influence), and competing amino-acid–free ion pair formation (specific influence)^{6–13}.

A lot of research effort, both at the experimental and computational level, has been devoted to the understanding of the solvation processes and structures of large and small ions, the question of ion pairing and the indirect structural effects leading to effective interactions between proteins and dissolved salts. The most prominent topic in this context are the ‘salting in’ and ‘salting out’ phenomena that led to the Hoffmeister series of ions and their kosmotropic/chaotropic characters¹⁴. The commonly accepted causality chain was that the presence of ions changes the water structure which induces a change in the ability of water to interact with the protein surface. The corresponding terms kosmotropic and chaotropic indicate that a specific ion can make the hydrogen bond network more rigid–kosmotropic or more flexible–chaotropic. An interesting related ongoing debate is whether the properties of solvating water molecules determine the behavior of proteins or whether the properties of the protein surface determine the behavior of the surrounding water (‘enslaved water’ versus ‘enslaving water’)^{15–17}.

Ion specific influence on water structure was observed experimentally by means of NMR measurements and computationally on different levels of theory^{18–24}; the effect was shown to go beyond the first solvation shell, i.e. beyond water molecules in direct contact with ions. Authors^{25,26} described to which extent water dynamics depended on specific ions and their concentrations: at low salt concentration ion specific effects are present—either slowing down or speeding up water motion, at high salt concentrations the effect is unspecific due to increased viscosity—water dynamics is slowed down. Recently, some authors argued that specific influence of

Martin Luther University Halle–Wittenberg, Institute of Physical Chemistry, 06120, Halle, Saale, Germany. Correspondence and requests for materials should be addressed to D.S. (email: daniel.sebastiani@chemie.uni-halle.de)

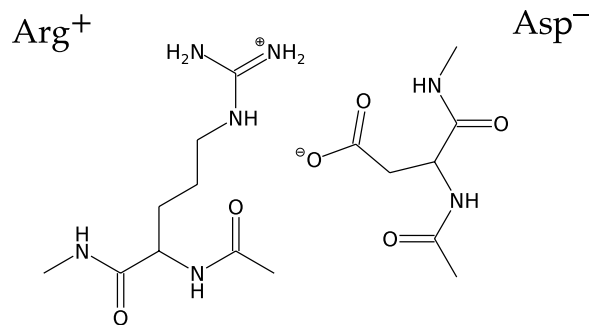


Figure 1. Structure of the studied salt bridge.

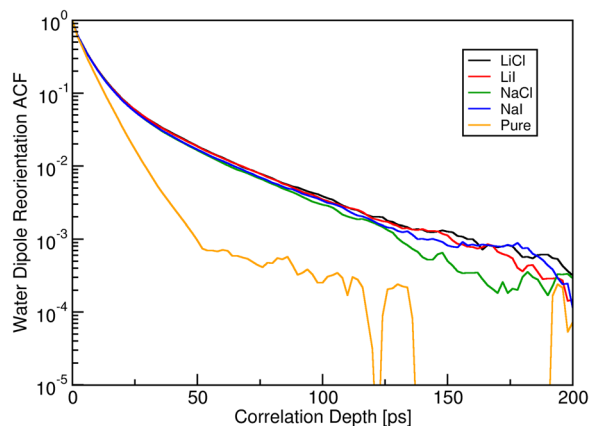


Figure 2. Vector autocorrelation functions of the dipole vector of water for all studied systems.

Hofmeister ions is dominant²⁷: only properties of species directly interacting with ions change, whereas properties of bulk solvent stay completely intact (see Zhang *et al.*²⁸ and papers cited therein).

In this work, we investigate a common salt bridge and quantify the effect of a series of solvated ions on both structure and dynamics as well as the consequent influence on thermodynamic properties. Do simple ions influence the salt bridge? Is this influence specific or unspecific? We have performed MD simulations of the Arginine-Aspartic acid dimer in aqueous solution, in a setup similar to the one chosen by Chong *et al.*²⁹. While being relatively simplistic, this model allows to enhance our focus on the interplay of water-ion-amino acid interactions, excluding other more subtle interactions in a protein. It is known that MD simulations are highly susceptible to minute changes in force fields^{29–31}. Interactions with ions require additional care to be able to account for polarization effects. This can be achieved either by employing polarizable force fields³² or scaling ion parameters^{33–35} to ensure that the results of the computer simulations reproduce specific experimental findings. For our study, we have chosen the latter option; we use Kirkwood-Buff-type force field ion parameters proposed for non-polarizable force fields by Gee *et al.*³⁵ together with force field parameters and water model relying on a benchmark study of the salt bridge by Chong *et al.*²⁹.

Results

We have investigated the effect of several ions from the Hofmeister series on the stability of a capped Arginine-Aspartic acid salt bridge (Fig. 1) in pure water and in 1 M aqueous solutions of NaCl, NaI, LiCl, and LiI. We have performed Umbrella pulling classical molecular dynamics simulations of those systems under ambient conditions (see Methods section for more details).

Water rotational dynamics. A good overall estimator for the stiffness of the hydrogen bond network of an aqueous system is the reorientation dynamics of the water molecules. We address this property via the vector autocorrelation function of the dipole vector of the ensemble of water molecules in our different systems: all water molecules of the simulation cell are taken into account in this analysis to avoid any ambiguity of a distance cutoff. The set of autocorrelation functions of the solvated salt bridge with and without additional salt ions is shown in Fig. 2. The decay for pure water (i.e. no additional solvated ions beyond the Arg⁺-Asp⁻ pair) is linear, representing a mono-exponential shape (note the logarithmic scale of the plot). This shows that only a single type of activated microscopic process is involved, which is expected for regular liquid water. As soon as further ions are added (all in 1 M concentration), the autocorrelation decay of the water is slowed down, and the shape is no longer linear. This illustrates a considerable stiffening of the hydrogen bond network and the existence of at least one more activated process for a sizeable subset of water molecules. Note that only a certain

System	O (Asp) ⁻ -H (Water)	H (Arg) ⁺ -O (Water)	O (Asp) ⁻ -Cation	H (Arg) ⁺ -Anion	O (Water)-Cation	H (Water)-Anion
LiCl	85	63	4412	141	161	43
LiI	89	62	4729	91	152	31
NaCl	89	62	591	159	117	42
NaI	84	55	689	85	116	31
Pure water	64	39	—	—	—	—

Table 1. Intermittent lifetimes of complexes (in ps).

percentage of water molecules is affected to yield the observed slowing down. It is also remarkable that all salt combinations exhibit virtually the same autocorrelation decay, pointing to a quite unspecific effect. The time constant of the exponentially decaying autocorrelation function at long correlation times (~100 ps) is about five times smaller than the time constant for pure water at shorter times, meaning that the reorientation rate of the water molecules affected by the solvated ions is significantly smaller than that of pure water. We have performed a similar analysis of the autocorrelation functions of the OH bond vectors, with similar results (see the supporting information for details).

Ion pair dissociation dynamics. Complementarily to the reorientation dynamics of the water, we determined directly the lifetimes of the ion-ion and ion-water aggregates. To this purpose, we computed the pairwise aggregate autocorrelation functions corresponding to each possible dimer (out of Arg⁺-A⁻/H₂O, Asp⁻-Me⁺/H₂O) via a suitable geometric criterion (see Methods section for details). Specifically, a good measure for such a statistically averaged lifetime is the total integral over the correlation function, which equals the exponential time constant in case of a mono-exponential decay.

We have summarized the resulting lifetimes for the most relevant ion-ion and ion-water dimers as function of the co-solvents in Table 1. The distribution of our computed values ranges from 30 ps to almost 5 ns, with a strong dependence on the nature of the involved ion and solvent composition. The most striking specific feature is the very long lifetime of the Li⁺ and also Na⁺ ions coordination to the Asp⁻ oxygen atoms, as opposed to all other combinations. This observation is consistent with the strongly kosmotropic nature of the Li⁺ ion, that is even more pronounced when its bonding partner is not neutral water but an anion. Nevertheless, the strength of the effect is surprising: the average lifetime is about fifty times longer than that of a water-Asp⁻ dimer.

Exchanging chloride against iodide results in a gradually weaker aggregation with both Arg⁺ and water molecules, which is consistent with the more chaotropic character of iodide. Note also the consistently stronger aggregation of the Cl⁻/I⁻ anions with the cationic sites of the amino acids, compared to the aggregation of Cl⁻/I⁻ with water molecules. This trend can be explained by the difference of a full elementary charge at Arg⁺ versus the dipole of the water molecules.

An interesting yet relatively small feature is that an unspecific effect is observed for water-Asp⁻/Arg⁺ hydrogen bonding: the presence of any type of additive ions in the solvent increases the stability of both water-Arg⁺ and water-Asp⁻ complexes by about 50%. This effect is stronger than expected, since the dissolved ions are not directly involved in the considered aggregates.

Our analysis of the dissociation dynamics of ion-ion and water-ion pairs thus illustrates the highly specific effect that solvated cations (especially Li⁺) have on the lifetime of complexes that they form with the Asp⁻ site; in turn, the lifetimes of the other possible complexes remain only modestly affected.

Coordination strength of the salt bridge. The significantly prolonged lifetime of complexes between the Li⁺ ions and the anionic amino acid site raises the question about the statistical relevance of this aggregate, i.e. how persistent such a Asp⁻-Li⁺ coordination is compared to the competing Asp⁻-water coordination and the complementary Arg⁺-Cl⁻/I⁻/water coordination complexes. To this purpose, we have computed the radial distribution functions (RDFs) of the corresponding sites, shown in Fig. 3.

We observe a striking difference in the coordination of the Asp⁻ with Li⁺/Na⁺ and water. The first peak in the Li⁺ RDFs is about twenty times higher than that of water, which correlates well with the findings related to the corresponding aggregate lifetimes. It should be noted though that one of the reasons this difference appears large is due to the normalization of the RDF to the overall concentration (which is lower for Li⁺ and Na⁺ ions than it is for H₂O molecules). Upon integration of the first peak in the RDF, it turns out that an Asp⁻-Li⁺ complex exists for about 50% of the time within our trajectory. This means that the interaction is enthalpically so favorable that it compensates the relatively low concentration of Li⁺ ions (compared to water molecules), resulting in an almost persistent structural feature. Note that the level of theory of our molecular dynamics simulation is not ideally suited for such strong interactions at the edge to a semi-covalent bond, a more accurate choice would be an ab initio based MD (presently ongoing). Nevertheless, the difference between Li⁺ and water coordination to Asp⁻ is very significant. Again, the Asp⁻-Na⁺ complex is much less prominent, which is consistent with the more bulky character of the sodium ion.

These findings correlate well with the average statistical ion density between the salt bridge charge groups, as illustrated in Figure S-18 (see the Supporting Information). The anions are generally repelled from the “salt bridge region” between Asp⁻ and Arg⁺, with the effect being much stronger for iodide than for chloride. For the cations, it differs. Lithium seems to be attracted to that region, with density ratios larger than 1. Sodium, however, seems to be slightly repelled, with density ratios slightly below 1.

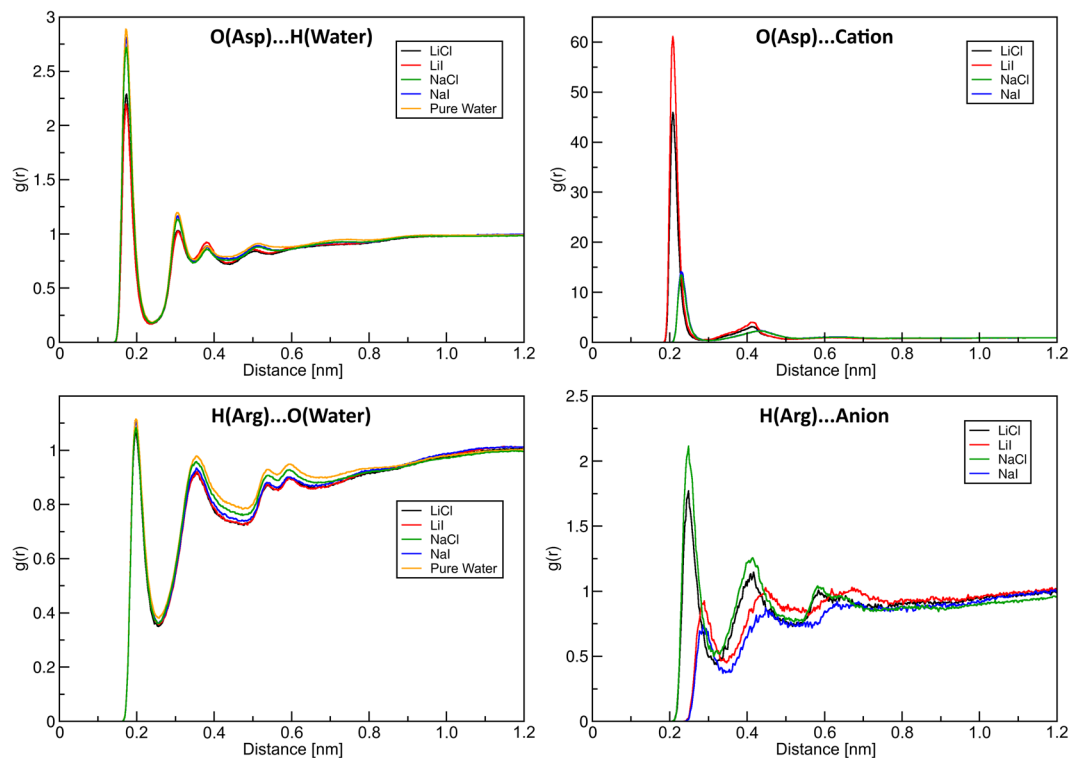


Figure 3. Radial distribution functions (RDF) between ion–ion and ion–water, analysis performed over all length of a corresponding trajectory.

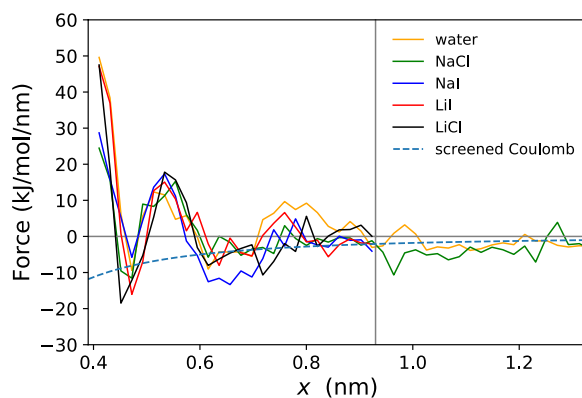


Figure 4. Mean force as a function of distance between guanidinium carbon - carboxylic carbon of the Arg-Asp salt bridge, together with screened Coulomb force ($\epsilon_r = 80$).

The coordination of the cationic amino acid to the anions turns out to be less spectacular. While the $\text{Arg}^+\text{-Cl}^-$ peak in the RDF in Fig. 3 is more than twice as strong as the $\text{Arg}^+\text{-I}^-$ counterpart, there is no visible effect of the solvated salt on the $\text{Arg}^+\text{-water}$ coordination. The integration of the first peak in the $\text{Arg}^+\text{-Cl}^-$ and $\text{Arg}^+\text{-I}^-$ radial distribution functions yields a low degree of persistence for the ionic coordination: an $\text{Arg}^+\text{-Cl}^-$ ion pair exists in only about 6% of the simulated time, and the probability for an $\text{Arg}^+\text{-I}^-$ complex is around 4%.

Mean force along salt bridge dissociation. We have computed the mean force between the anionic and cationic sites of the salt bridge in the different solutions during a forced dissociation event. The intermolecular force curve as a function of the distance between the carboxylic and guanidinium groups (i.e. the centers of charge) is shown in Fig. 4, along with the analytic screened Coulomb attraction between two elementary charges assuming a dielectric constant of $\epsilon_r = 80$. The force curve exhibits a repulsive nature for distances below the equilibrium value of about $x = 0.43$ nm, followed by an attractive regime in the range $0.43 \text{ nm} \leq x \leq 0.5$ nm and again a repulsive window at $0.5 \text{ nm} \leq x \leq 0.6$ nm. Beyond that distance, the force approximately follows a screened Coulomb attraction. While the magnitude of the inter-ionic forces is relatively small compared to the considerable noise, the coinciding positions for the zeros of the force (i.e. equilibrium distances) increase the reliability of

the ranges corresponding to attractive and repulsive regimes. It should be noted that the force curves for different salt additives do not exhibit any systematic differences above the noise level.

First, it is surprising that the width of attractive range (first minimum in Fig. 4) around $x = 0.46$ nm is comparable to the subsequent repulsive window (first maximum in Fig. 4). The magnitudes of the attractive/repulsive forces are about the same. Both observations indicate that there is actually little to no energetic preference for an intact salt bridge in solution, there is even a considerable energy barrier for its formation. Equally surprising is the missing dependence on either ion species for the additional salt in the solution. The very pronounced structural and dynamical features induced by the Li^+ and Na^+ ions have no visible effect on the energetic level. While the absence of any specific or unspecific effect can be explained for the anion (Cl^- and I^-) via the comparably weak complex formation preference, it is not obvious why a quasi persistent Li^+ coordination of the Asp^- oxygen atoms does not affect the inter-molecular forces on the amino acid residues. To a certain extent, geometric considerations based on the spatial distribution functions (see the supporting information) can help to understand this phenomenon: early during our simulations, Asp^- rotates so that only one of its carboxyl oxygen atoms is hydrogen-bonded to the Arg^+ guanidinium protons, leaving the remaining carboxyl oxygen atom free to bind to a Li^+ .

Discussion

We have investigated the influence of external constraints on a protein salt bridge, specifically the effect of simple salts on an Arginine–Aspartic acid dimer in aqueous solution, by means of molecular dynamics simulations. Besides structural and dynamical features at equilibrium, we have computed the mean force along the dissociation pathway of the salt bridge.

The analysis of our MD trajectories reveals a number of significant consequences of the presence of additional ions in the solution. The hydrogen bonding network of water becomes more rigid, reflected in the emergence of a slower rotational relaxation process (see Fig. 2): a closer analysis reveals that only those water molecules in direct contact with ions are affected. Such a behaviour was observed earlier experimentally by NMR measurements, where different clusters of solvatomers manifested themselves by an offset of the average chemical shift of water protons, as well as by a slowing down of their relaxation time^{18,23,24}. However, these effects remain local to the first solvation sphere of the ions and do not significantly change the bulk properties of the system²⁸. The same picture emerges for the different sets of ion pairs (Asp^- – Li^+ / Na^+ /water, Arg^+ – Cl^- / I^- /water): more kosmotropic ions Li^+ and Cl^- form longer-living complexes compared to more chaotropic Na^+ and I^- . Especially, the complex Li^+ – Asp^- is strikingly stable and persisted for ~50% of simulation time. Neither ion pair, however, induces structural or dynamical changes beyond its immediate vicinity. One can extrapolate these results to higher concentrations: with more ions added to the solution more and more water molecules will be participating in building up their solvation shells. This in turn will eventually lead to a slowing down of diffusion processes, indicating the formation of ‘stable’ water–ion aggregates, as was found in simulations of 9 M LiI aqueous solution²⁴.

In contrast to these findings, which are in agreement with both chemical intuition and literature, the shape of the intermolecular force along the dissociation coordinate of the salt bridge indicates that the commonly assumed function of a protein salt bridge as a structural driving force may need to be revised⁵. The weakness of the attractive interaction at equilibrium distance combined with the presence of the repulsive force of a similar magnitude at 0.55 nm illustrates that the thermodynamic relevance of a salt bridge in such environment is much smaller than normally assumed.

To summarize, we have shown that Hofmeister ions influence the behavior of a solvated salt bridge in a very local and specific manner, namely the formation of tight ionic pairs between Li^+ / Na^+ and Asp^- . Bulk properties, however, are almost unaffected. Moreover, our findings show that the enthalpic function of the solvated salt bridge is minor, regardless of the presence of solvated ions. Specifically, the Li^+ – Asp^- interaction clearly calls for a more in-depth investigation that should be carried out using ab initio molecular dynamics simulations that are able to capture the range of hydrogen bonding versus covalent/coordination bonding at a very high level of accuracy.

Methods

Classical Molecular Dynamic simulations were performed in GROMACS 2016.3^{36,37}. We have used the AMBER03ws force field together with the TIP4PEw water model²⁹. Ion parameters were taken from Gee *et al.*³⁵. We have used a CSVR thermostat³⁸ to keep 296 K temperature of the system together with Parrinello–Rahman barostat^{39,40} with $\tau_p = 1$ ps. We have simulated a capped arginine–glutamate salt bridge²⁹ in side-on conformation in 6/4/4 nm periodic box. The same setup was used in a paper by Chong *et al.*²⁹, where authors have benchmarked performance of different force-fields as well as different water models. The structure was first equilibrated, solvated and optimized in pure water. Then ions were added into the simulation cell. In our simulation we have used LiI, LiCl, NaI, NaCl with 1 M concentration (58 anions and 58 cations). Same starting geometries of the salt bridge were used as starting points for all salts. Distance between charge centers of two amino acids, namely carboxylic carbon of Asp^- and guanidinium carbon of Arg^+ , was chosen as a reaction coordinate for cz trajectories (discussed in the main article), as well as distance between the C_α carbons for ca trajectories (see Supporting Information). To check reproducibility, we have repeated a simulation for NaCl changing the simulation temperature by 0.1 K, labeled NaClcheck. The routine of a simulation was: energy minimization followed by 3 ns equilibration of solvent. Umbrella pulling trajectory was performed with pull speed 0.0002 nm/ns for 270 ns for all salts, except for NaCl (cz and ca), NaClcheck (cz) and water (cz and ca) where the simulation was ran for 600 ns. To summarize, we have performed a forced dissociation of the Arginine–Aspartic acid anion dimer by applying a harmonic constraint to the reaction coordinate, and then moving the minimum of the applied potential along the coordinate with a constant velocity: ‘Umbrella pulling’. Very slow pulling rate allowed us to sample all other

degrees of freedom of the system in a single trajectory. The mean force was projected onto the reaction coordinate for every timestep.

Analysis of trajectories was performed with VMD⁴¹. The RDFs, vector autocorrelation plots and lifetimes were computed with the TRAVIS program package⁴². The plots within this article have been created with Pyplot library in Python as well as with xmgrace⁴³.

A well-established way of investigating lifetimes of aggregates in a molecular dynamics trajectory is to define a geometric aggregation criterion and to autocorrelate the corresponding pair definition function for each possible bonding aggregate. The integral over the resulting autocorrelation function (ACF) can then be considered as the aggregate's lifetime. In this work, we use a simple distance criterion to define aggregates between aspartate, arginine, anions, cations, and water. The distance cutoff values were derived from the position of the first minimum in the corresponding RDFs. We selected 300 pm for the Cation–O(Asp) distance; 330 pm for the Anion–H(Arg), Anion–H(Water), and Cation–O(Water) distance; 250 pm for the H(Water)–O(Asp) and O(Water)–H(Arg) distance. Lifetimes have been computed by using the intermittent formalism from Rapaport⁴⁴, which allows aggregates to break and reform at a later time. These intermittent ACFs are much less prone to noise than the corresponding continuous functions, which do not permit for re-formation of aggregates. When considering intermittent ACFs, special care has to be taken in the case of finite-size systems. The functions will not fall to zero after very long correlation time, but to the *ensemble average* instead, which is the average probability of observing a hydrogen bond in one specific pair after very long simulation. This effect can be corrected by subtracting the ensemble average from the intermittent ACFs, which is called *ensemble average correction*. This correction was described in literature before⁴⁵ and is applied here.

The radial distribution function curves are normalized to uniform particle density, which means that a value of 1 depicts a probability of finding a certain particle in a certain distance which equals the probability of finding that particle at any random point in the simulation cell.

References

- Donald, J. E., Kulp, D. W. & DeGrado, W. F. Salt bridges: Geometrically specific, designable interactions. *Proteins: Struct. Funct. Bioinforma.* **79**, 898–915, <https://doi.org/10.1002/prot.22927> (2011).
- Bosshard, H. R., Marti, D. N. & Jelezarov, I. Protein stabilization by salt bridges: Concepts, experimental approaches and clarification of some misunderstandings. *J. Mol. Recognit.* **17**, 1–16, <https://doi.org/10.1002/jmr.657> (2004).
- Waldburger, C., Schildbach, J. & Sauer, R. T. Are buried salt bridges important for protein stability and conformational specificity? *Nat. Struct. Biol.* **2**, 122–8, PMID:7749916 (1995).
- Petrauskas, V., Maximowitsch, E. & Matulis, D. Thermodynamics of ion pair formations between charged poly(amino acid)s. *The J. Phys. Chem. B* **119**, 12164–12171, <https://doi.org/10.1021/acs.jpcc.5b05767>. PMID: 26317887 (2015).
- Pluhařová, E., Marsalek, O., Schmidt, B. & Jungwirth, P. Peptide salt bridge stability: From gas phase via microhydration to bulk water simulations. *The J. Chem. Phys.* **137**, 185101, <https://doi.org/10.1063/1.4765052> (2012).
- Draper, D. E. A guide to ions and rna structure. *RNA* **10**, 335–343, <https://doi.org/10.1261/rna.5205404> (2004).
- Smith, M. D. & Cruz, L. Effect of ionic aqueous environments on the structure and dynamics of the A_β_{21–30} fragment: A molecular-dynamics study. *The J. Phys. Chem. B* **117**, 6614–6624, <https://doi.org/10.1021/jp312653h>. PMID: 23675877 (2013).
- Fox, J. M. *et al.* Interactions between hofmeister anions and the binding pocket of a protein. *J. Am. Chem. Soc.* **137**, 3859–3866, <https://doi.org/10.1021/jacs.5b00187>. PMID: 25738615 (2015).
- Smith, M. D. & Cruz, L. Changes to the structure and dynamics in mutations of A_β_{21–30} caused by ions in solution. *J. Phys. Chem. B* **131**, 121094906005, <https://doi.org/10.1021/jp408579v> (2013).
- Liao, Q., Owen, M. C., Bali, S., Barz, B. & Strodel, B. A_β under stress: the effects of acidosis, Cu²⁺-binding, and oxidation on amyloid- β peptide dimers. *Chem. Commun.* <https://doi.org/10.1039/C8CC02263A> (2018).
- Bye, J. W. & Falconer, R. J. Thermal stability of lysozyme as a function of ion concentration: A reappraisal of the relationship between the hofmeister series and protein stability. *Protein Sci.* **22**, 1563–1570, <https://doi.org/10.1002/pro.2355> (2013).
- Pegram, L. M. *et al.* Why hofmeister effects of many salts favor protein folding but not dna helix formation. *Proc. Natl. Acad. Sci.* **107**, 7716–7721, <https://doi.org/10.1073/pnas.0913376107> (2010).
- Senske, M. *et al.* The temperature dependence of the hofmeister series: thermodynamic fingerprints of cosolute-protein interactions. *Phys. Chem. Chem. Phys.* **18**, 29698–29708, <https://doi.org/10.1039/C6CP05080H> (2016).
- Hofmeister, F. Zur lehre von der wirkung der salze. *Arch. fuer experimentelle Pathol. und Pharmakologie* **24**, 247–260, <https://doi.org/10.1007/BF01918191> (1888).
- Rinne, K. F., Schulz, J. C. F. & Netz, R. R. Impact of secondary structure and hydration water on the dielectric spectrum of poly-alanine and possible relation to the debate on slaved versus slaving water. *The J. Chem. Phys.* **142**, 215104, <https://doi.org/10.1063/1.4921777> (2015).
- Fenimore, P. W., Frauenfelder, H., McMahon, B. H. & Parak, F. G. Slaving: Solvent fluctuations dominate protein dynamics and functions. *Proc. Natl. Acad. Sci.* **99**, 16047–16051, <https://doi.org/10.1073/pnas.212637899> (2002).
- Daldrop, J. O. *et al.* Orientation of non-spherical protonated water clusters revealed by infrared absorption dichroism. *Nat. Commun.* **9**, 311 (2018).
- Boisson, J., Stirnemann, G., Laage, D. & Hynes, J. T. Water reorientation dynamics in the first hydration shells of F⁻ and I⁻. *Phys. Chem. Chem. Phys.* **13**, 19895, <https://doi.org/10.1039/c1cp21834d> (2011).
- Geiger, A. & Hertz, H. G. Proton magnetic relaxation study of water orientation around I⁻ and Li⁺. *J. Solut. Chem.* **5**, 365–388, <https://doi.org/10.1007/bf00646412> (1976).
- Langer, H. & Hertz, H. The Structure of the First Hydration Sphere of Ions in Electrolyte Solutions A Nuclear Magnetic Relaxation Study. *Ber. Bunsenges. Phys. Chem.* **81**, 478–490, <https://doi.org/10.1002/bbpc.19770810506> (1977).
- Mazitov, R., Mueller, K. J. & Hertz, H. G. Determination of Water Orientation in the Hydration Sphere of Li⁺ by the Nuclear Magnetic Relaxation Method. *Z. Phys. Chem.* **140**, 55–70, <https://doi.org/10.1524/zpch.1984.140.1.055> (1984).
- Sacco, A. Structure and dynamics of electrolyte solutions. A NMR relaxation approach. *Chem. Soc. Rev.* **23**, 129, <https://doi.org/10.1039/cs9942300129> (1994).
- Kim, J. S., Wu, Z., Morrow, A. R., Yethiraj, A. & Yethiraj, A. Self-Diffusion and Viscosity in Electrolyte Solutions. *J. Phys. Chem. B* **116**, 12007–12013, <https://doi.org/10.1021/jp306847t> (2012).
- Allolio, C., Salas-Illanes, N., Desmukh, Y. S., Hansen, M. R. & Sebastiani, D. H-bonding competition and clustering in aqueous lii. *The J. Phys. Chem. B* **117**, 9939–9946, <https://doi.org/10.1021/jp4033468>. PMID: 23909514 (2013).
- Stirnemann, G., Wernersson, E., Jungwirth, P. & Laage, D. Mechanisms of Acceleration and Retardation of Water Dynamics by Ions. *J. Am. Chem. Soc.* **135**, 11824–11831, <https://doi.org/10.1021/ja405201s> (2013).
- Lyubartsev, A. P. & Laaksonen, A. Concentration Effects in Aqueous NaCl Solutions. A Molecular Dynamics Simulation. *J. Phys. Chem.* **100**, 16410–16418, <https://doi.org/10.1021/jp961317h> (1996).

27. Okur, H. I. *et al.* Beyond the hofmeister series: Ion-specific effects on proteins and their biological functions. *The J. Phys. Chem. B* **121**, 1997–2014, <https://doi.org/10.1021/acs.jpcc.6b10797>. PMID: 28094985 (2017).
28. Zhang, Y. & Cremer, P. S. Interactions between macromolecules and ions: the hofmeister series. *Curr. Opin. Chem. Biol.* **10**, 658–663, <https://doi.org/10.1016/j.cbpa.2006.09.020>. Model systems/Biopolymers (2006).
29. Debiec, K. T., Gronenborn, A. M. & Chong, L. T. Evaluating the strength of salt bridges: A comparison of current biomolecular force fields. *The J. Phys. Chem. B* **118**, 6561–6569, <https://doi.org/10.1021/jp500958r>. PMID: 24702709 (2014).
30. Piana, S., Lindorff-Larsen, K. & Shaw, D. E. How robust are protein folding simulations with respect to force field parameterization? *Biophys. J.* **100**, L47–L49, <https://doi.org/10.1016/j.bpj.2011.03.051> (2011).
31. Rauscher, S. *et al.* Structural ensembles of intrinsically disordered proteins depend strongly on force field: A comparison to experiment. *J. Chem. Theory Comput.* **11**, 5513–5524, <https://doi.org/10.1021/acs.jctc.5b00736> (2015).
32. Huang, J., Lopes, P. E. M., Roux, B. & MacKerell, A. D. Recent advances in polarizable force fields for macromolecules: Microsecond simulations of proteins using the classical drude oscillator model. *The J. Phys. Chem. Lett.* **5**, 3144–3150, <https://doi.org/10.1021/jz501315h>. PMID: 25247054 (2014).
33. Luo, Y., Jiang, W., Yu, H., MacKerell, A. D. & Roux, B. Simulation study of ion pairing in concentrated aqueous salt solutions with a polarizable force field. *Faraday Discuss.* **160**, 135–149, <https://doi.org/10.1039/C2FD20068F> (2013).
34. Fyta, M. & Netz, R. R. Ionic force field optimization based on single-ion and ion-pair solvation properties: Going beyond standard mixing rules. *The J. Chem. Phys.* **136**, 124103, <https://doi.org/10.1063/1.3693330> (2012).
35. Gee, M. B. *et al.* A kirkwood-buff derived force field for aqueous alkali halides. *J. Chem. Theory Comput.* **7**, 1369–1380, <https://doi.org/10.1021/ct100517z>. PMID: 21789033 (2011).
36. Abraham, M. J. *et al.* GROMACS: High performance molecular simulations through multi-level parallelism from laptops to supercomputers. *Software X* **1–2**, 19–25, <https://doi.org/10.1016/j.softx.2015.06.001> (2015).
37. Essmann, U. *et al.* A smooth particle mesh ewald method. *The J. Chem. Phys.* **103**, 8577–8593, <https://doi.org/10.1063/1.470117> (1995).
38. Bussi, G., Donadio, D. & Parrinello, M. Canonical sampling through velocity rescaling. *J. Chem. Phys.* **126**, 014101, <https://doi.org/10.1063/1.2408420> (2007).
39. Parrinello, M. & Rahman, A. Polymorphic transitions in single crystals: A new molecular dynamics method. *J. Appl. Phys.* **52**, 7182–7190, <https://doi.org/10.1063/1.328693> (1981).
40. Parrinello, M. & Rahman, A. Crystal structure and pair potentials: A molecular-dynamics study. *Phys. Rev. Lett.* **45**, 1196–1199, <https://doi.org/10.1103/PhysRevLett.45.1196> (1980).
41. Humphrey, W., Dalke, A. & Schulten, K. VMD—Visual Molecular Dynamics. *J. Mol. Graph.* **14**, 33–38 (1996).
42. Brehm, M. & Kirchner, B. Travis—a free analyzer and visualizer for monte carlo and molecular dynamics trajectories. *J. Chem. Inf. Model.* **51**, 2007–2023 (2011).
43. Grace, (c) 1996–2008 grace development team, see <http://plasma-gate.weizmann.ac.il/grace>.
44. Rapaport, D. Hydrogen bonds in water. *Mol. Phys.* **50**, 1151–1162, <https://doi.org/10.1080/00268978300102931> (1983).
45. Gehrke, S. *et al.* Structure and lifetimes in ionic liquids and their mixtures. *Faraday Discuss.* **206**, 219–245, <https://doi.org/10.1039/C7FD00166E> (2017).

Acknowledgements

The authors thank Deutsche Forschungsgemeinschaft (DFG, SFB-TRR 102 project A09) for funding this work. M.B. acknowledges financial support by the DFG through project Br 5494/1-1. S.P. thanks Dr. Hossam Elgabarty for fruitful discussions.

Author Contributions

D.S. conceived and supervised the project and the simulations, S.P. and M.B. conducted the simulations and the data analysis. All authors reviewed the manuscript.

Additional Information

Supplementary information accompanies this paper at <https://doi.org/10.1038/s41598-018-31935-z>.

Competing Interests: The authors declare no competing interests.

Publisher's note: Springer Nature remains neutral with regard to jurisdictional claims in published maps and institutional affiliations.



Open Access This article is licensed under a Creative Commons Attribution 4.0 International License, which permits use, sharing, adaptation, distribution and reproduction in any medium or format, as long as you give appropriate credit to the original author(s) and the source, provide a link to the Creative Commons license, and indicate if changes were made. The images or other third party material in this article are included in the article's Creative Commons license, unless indicated otherwise in a credit line to the material. If material is not included in the article's Creative Commons license and your intended use is not permitted by statutory regulation or exceeds the permitted use, you will need to obtain permission directly from the copyright holder. To view a copy of this license, visit <http://creativecommons.org/licenses/by/4.0/>.

© The Author(s) 2018

The conformational ensemble of Polyglutamine-14 chains: specific influences
of solubility tail and chromophores

S. Pylaeva, A. Böker, H. Elgabarty, W. Paul, and D. Sebastiani, *ChemPhysChem*, 2018, **19**, 2931.

Reprinted with permission. Copyright 2018 Wiley-VCH Verlag GmbH & Co. KGaA, Weinheim

DOI: 10.1002/cphc.201800551

The Conformational Ensemble of Polyglutamine-14 Chains: Specific Influences of Solubility Tail and Chromophores

Svetlana Pylaeva,^[a] Arne Böker,^[b] Hossam Elgabarty,^[a] Wolfgang Paul,^[b] and Daniel Sebastiani^{*[a]}

We address polyglutamine-14 in aqueous solution with specific chromophores and a solubility chain by means of a multiscale simulation approach, combining atomistic molecular dynamics simulations and coarse-grained Monte-Carlo conformational sampling. Despite the intrinsically disordered nature of the amyloidogenic polyglutamine, we observe transient character-

istic structural motifs which exhibit a specific hydrogen bonding pattern. We illustrate the relationship between structure pattern and the distance distribution of a pair of chromophores attached to the peptide termini, in light of specific influence of a short solubility tail and the chromophores themselves on the conformational ensemble.

1. Introduction

Polyglutamines (PolyQs) belong to a large family of intrinsically disordered proteins, which means that they do not have a well-defined secondary structure under physiological conditions. PolyQs were shown to aggregate and form fibrils.^[1] The mature fibrils display a regular cross- β structure, typical for amyloid forming proteins and peptides, which is well investigated experimentally.^[2,3] These PolyQ repeats are supposed to be the fibril generating part of the huntingtin protein, related to Huntington's disease.^[4] However, the structure of oligomers, small molecular aggregates, as well as PolyQ monomers has not been fully understood yet, despite the significant interest in this topic^[1,5] due to their expected role in fibril formation. Miettinen et al.^[6] report stable PolyQ dimers containing a β -hairpin motif, while α -helices which are stable as monomers lack kinetic stability to support oligomerization. Dimers of steric-zipper, β -nanotube or β -pseudohelix are argued to be too short lived for further aggregation.^[7,8]

Due to its expected importance for the understanding of the amyloid aggregation pathways of PolyQs, the exploration of the structural properties of these chains has received much attention in computer simulation studies. Vitalis et al.^[9] have examined the amount of β content in polyglutamine monomers with 5, 15, 30 and 45 glutamines using a Markov Chain Metropolis Monte Carlo simulations of a chemically realistic model in implicit solvent. They show that β -sheet rich phases are rather attributes of high molecular weight aggregates than of monomers or oligomers. The authors^[10] have argued earlier that at room temperature polyQs adopt collapsed disordered

structures to maximize self-interactions and minimize unfavorable solute-solvent interface. This is in agreement with experimental fluorescence correlation spectroscopy data^[11] where globular configurations were shown to dominate.

Kar et al.^[12] introduced β -hairpin forming motifs into the polyQ sequence, this resulted in faster aggregation. However, the fibril structure was almost unchanged from native polyQs. The authors also noted that β -structure content was not enhanced for monomers. β -turn creation is argued to be an important step in the nucleation mechanism.

A recent review^[1] states that the concept of a "toxic monomer" is an elusive but feasible hypothesis. Even though it was previously argued that disordered globules can provide a nucleus for aggregation,^[10] the investigation of transiently stable secondary structure motifs in monomers which can facilitate further aggregation continues. Wang et al.^[13] have performed classical MD simulations with extensive phase space sampling of Q₅ and Q₁₅. The authors show that Q₁₅ can adopt β -sheet structures, though they are thermodynamically unfavorable. Nakano et al.^[14] have performed replica exchange molecular dynamics (REMD) simulations of Q₁₅, and they reported that the monomer can adopt various configurations due to formation of sidechain-backbone hydrogen bonds and has two different basins of structures: random coil and α -helix together with β -hairpin structures. Punihaole et al.^[15] have run a classical MD simulation of polyglutamine-10. They have used well tempered metadynamics simulations with a root mean square displacement (RMSD) of the Q₁₀ structure relative to the ideal α -helix, β -hairpin and PPII as the reaction coordinate. The free energy landscape they obtained is very frustrated. However, the authors see some deeper minima and attribute them to the structural motifs mentioned above.

A common technique used to investigate protein structure is Förster Resonance Energy Transfer (FRET) spectroscopy, which was successfully applied together with MD simulations for IDPs.^[16,17] Zerze et al.^[18] demonstrated that FRET chromophores have only modest influence on the structure of disordered peptides. However, to investigate PolyQ chains in solution a

[a] S. Pylaeva, H. Elgabarty, D. Sebastiani
Chemistry Department, MLU Halle-Wittenberg,
06120, Halle (Saale), Germany
E-mail: Daniel.sebastiani@chemie.uni-halle.de

[b] A. Böker, W. Paul
Physics Department, MLU Halle-Wittenberg, 06120, Halle (Saale), Germany

Supporting information for this article is available on the WWW under <https://doi.org/10.1002/cphc.201800551>

special amino acid sequence of some hydrophilic residues needs to be added to increase solubility.^[1,19]

We address this issue by investigating PolyQ with 14 sequential glutamine residues enclosed by grafted chromophores and followed by a suitable solubility tail, hence choosing a setup used in some experiments (see Table 1).^[19–21]

MD	DNB–(Gln) ₁₄ –(Ala + AMCA) –Ser–Arg–Ser–Arg–Gly	WQ ₁₄ W + tail
MC	Trp–(Gln) ₁₄ –Trp–Ser–Arg– Ser–Arg–Gly	WQ ₁₄ W + tail
MC	Trp–(Gln) ₁₄ –Trp	WQ ₁₄ W
MC	(Gln) ₁₆	Q ₁₆

We employ a combination of classical MD simulations in complete chemical detail and Stochastic Approximation Monte Carlo simulations of an intermediate-resolution protein model.

2. Computational Details

Classical molecular dynamics simulations were performed using Hamiltonian Replica Exchange with solute tempering 2 (REST2)^[22,23] in the PLUMED^[24] implementation^[25] in GROMACS 4.7.^[26,27] The CHARMM22*^[28–30] force field was used together with the TIP3P water model, and chromophore parameters were obtained from the SwissParam library.^[31] The chromophores grafted to the protein were dinitrobenzene (DNB) to the N-terminus and 7-amino-4-methyl-3-coumarinylacetic acid derivative (AMCA–H) was attached right after the 14-th Q via a modified alanine. Serine, arginine, serine, arginine and glycine were then added to the sequence forming a solubility tail. The C-terminus was furthermore amidated. Two Cl[–] atoms were added to neutralize charge. As computer simulations started from a fully extended conformation, the side length of a cubic simulation box size was chosen to be 8.85 nm. Simulations were run in the NVT ensemble under periodic boundary conditions. We used the Canonical Sampling through Velocity Rescaling (CSVR) thermostat^[32] with time constant of 0.3 ps. All covalent bonds to hydrogen atoms were constrained via a 4th order Linear Constraint Solver (LINCS)^[33] algorithm which allowed us to use a 1 fs time step. 12 replicas were run simultaneously over a temperature range from 296 K to 600 K. The exchange probability between neighboring replicas ranged from 0.2 to 0.3. Simulations were performed for 232 ns per replica, and the first 50 ns were not used for data analysis. Further analysis of the data was performed with MDTraj^[34] and VMD.^[35]

The PRIME20^[36] model is an intermediate resolution protein model, first published in 2010 as an extension to PRIME (Protein Intermediate-Resolution Model),^[37] developed by the same group in 2001. PRIME was first used to model polyalanine and later adapted to polyglutamine simulation.^[38,39] PRIME20 extends PRIME to include all 20 proteinogenic amino acids. Each amino acid is represented by four beads or “united atoms”, one

each for the backbone amino group (N), the alpha carbon (C_α), the carboxyl group (C), and the side chain (R). Bonds between these beads fluctuate freely within a narrow range around their ideal length. Bond angles, L-isomerization of amino acids and trans configuration of the peptide bond are imposed by pseudo-bonds with the same characteristics between next neighbors as well as between two neighboring C_α beads. All non-bonded beads interact via hard-sphere repulsion. Side chain beads have an additional square-well interaction whose strength depends on the interacting types. This interaction is a potential of mean force, implicitly parametrizing various types of residue-residue as well as residue-solvent interactions. To limit parameter space, the 20 different side chains are classified into 14 groups depending on their properties such as polarity, charge, or the capability to form hydrogen bonds. This way, the model only requires 19 energy parameters (i.e. well depths) compared to up to 171 if each pair of side chains (discounting Glycine) were assigned one parameter. Backbone (N–C) hydrogen bonds are modeled as a square well with additional restraints: the involved N–H–O and C–O–H angles (H and O positions are determined on demand) must be sufficiently straight, neither partner may be part of another hydrogen bond, and they must be separated by at least 3 intervening amino acids. If all these criteria are met, a hydrogen bond is formed with a well depth $O_{HB} = -1$, which dominates the energy function as all side chain energy parameters are between -0.585 (Cys-Cys interaction) and $+0.253$ (repulsion of charged side chains). In the sequences considered here, side chain well depths range from -0.205 to $+0.015$. The parameters of this model were determined by optimizing the structural agreement in the folded state with a set of 711 structures from the protein data base versus about 2 million decoys.^[36] Because the aforementioned chromophores are not part of the set of proteinogenic amino acids and therefore not parametrized by PRIME20, we replaced them with Tryptophans in our simulations.

Simulations of this model were performed using Stochastic Approximation Monte Carlo (SAMC). The SAMC algorithm^[40] belongs to the class of Flat Histogram Monte Carlo methods,^[41,42] which determine the density of states of a given system iteratively. From this, the method allows to calculate thermodynamic and structural properties of a given system over the complete temperature range (for technical details see^[41,42]).

3. Results and Discussion

As discussed above, we have applied two complementary computational approaches: atomistic molecular dynamics simulations and moderately coarse-grained Monte Carlo sampling, in order to combine an optimal conformational equilibration (via MC) with an accurate local structural resolution (via MD). Specifically, we have performed Replica Exchange MD with Solute Tempering 2 and Stochastic Approximation MC simulations with explicit and implicit aqueous solvation, respectively, on a polyglutamine-14 sequence with grafted FRET chromo-

phores as well as a 5 aminoacid residue solubility tail: labeled $WQ_{14}W$ +tail. Such a setup has been used experimentally before.^[20,21] We have used the distance d between the chromophores as the key structural variable, since the distribution of this distance can be probed experimentally via FRET measurements.^[19] In MD simulation the distance between the centers of mass of the chromophores was calculated; for MC the center of mass of a side-chain bead was used.

As a first probe, the correlation between the distance d and radius of gyration $R_g = \sqrt{\frac{1}{M} \sum_{i=1}^N m_i (\vec{r}_i - \vec{R}_{cm})^2}$ is plotted in Figure 1. Here, $\vec{R}_{cm} = \frac{1}{M} \sum_{i=1}^N m_i \vec{r}_i$ denotes the center of mass.

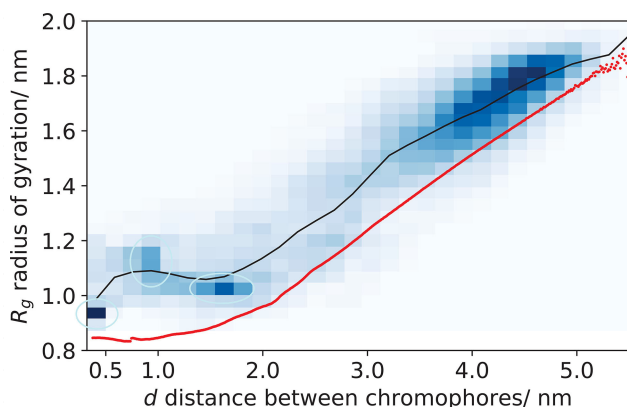


Figure 1. Correlation of radius of gyration R_g with distance between chromophores d . The shading indicates a height plot of a 2D histogram determined from MD, red points correspond to average values from SAMC runs and the black solid line describes average MD values. We have calculated the average curve by averaging over the vertical axis.

For reasons of visual clarity only the data from the MD simulation is plotted in the form of a color-coded 2D distribution in addition to the average behavior, while the data from the MC simulation is displayed in averaged form. There is a very good agreement between the two methods. The approximately constant offset of 0.2 nm can be attributed to the different structural resolution (atomistic/coarse-grained especially regarding the side chains) and corresponding differences in the mass distribution from which R_g is determined. The correlation between R_g and d is approximately linear for the region $d > 2$ nm, while R_g is almost constant for $d < 2$ nm (fluctuations within 0.1 nm).

In addition to the gyration radius of the peptide, we have analyzed the relative shape anisotropy κ^2 , which is a widely used descriptor of macromolecular shape in polymer physics.^[43,44] It is defined as $\kappa^2 = 1 - 3 \frac{L_1 L_2 + L_2 L_3 + L_3 L_1}{(L_1 + L_2 + L_3)^2}$, where L_{1-3} are the eigenvalues of the gyration tensor. κ^2 will be close to one for linear, rod-like arrangements, around one quarter for disc-shaped and zero for spherical or highly symmetric configurations. Figure 2 shows the correlation between κ^2 and the chromophore distance d . Again, there is an excellent agreement between the two computational methods, with a notable exception at $d = 1$ nm, where MD yields $\kappa^2 = 0.35$ and MC has $\kappa^2 = 0.2$. This deviation illustrates that for some specific

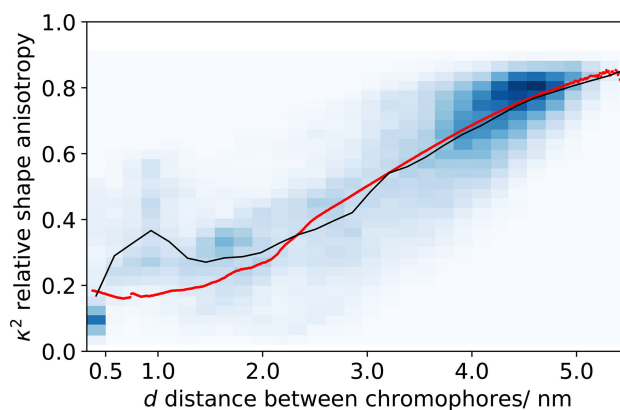


Figure 2. Correlation between fractional anisotropy κ^2 with the distance between chromophores d . The 2D histogram presents MD results, the red points correspond to average values from SAMC runs and the black solid line describes average MD values. We have calculated the average curve by averaging over the vertical axis.

conformational features the representation is different between atomistic and coarse-grained descriptions. Nevertheless, the overall shape of the curve agrees between the methods. Figure 2 shows that there is a considerable contribution from a rod-like configuration for the $WQ_{14}W$ +tail system ($d \approx 4.5$ nm). An equally relevant contribution stems from disc-shaped conformations, covering a wide range of chromophore distances (0.5–3 nm). For the latter ensemble of conformations there is no clear correlation between shape anisotropy κ^2 and the chromophore distance d . It should be noted also, however, that no sizable contribution from highly symmetric contributions is found ($\kappa^2 \approx 0$). The structures closest to a globular conformation are obtained in the MD trajectory for chromophores in direct contact ($d = 0.5$ nm). The features at $d = 1$ nm and $\kappa^2 \approx 0.4$ as well as $d = 1.6$ nm and $\kappa^2 \approx 0.35$ (see also Figure 1), hint at the existence of more ordered conformations, corresponding to a narrow window of chromophore distances which are consistent with β -turn arrangements. The wide overall distribution of κ^2 values confirms the findings of previous studies, that showed PolyQs tendency to be highly disordered.^[15]

In order to address the specific structural features more closely, we have plotted the average number of H-Bonds n_{HB} from both MD and MC simulations in Figure 3. Since the model used in MC only features an energetic contribution from hydrogen bonds between backbone beads (BB), not between backbone and side chain (BS), the latter are also left out of the MD data shown in the red curve, but included in the blue dotted line for comparison. For high d , both simulation approaches agree very well. The average number of BB H-bonds is below 1, indicating elongated random structures. MD results indicate an average of 2 BS H-Bonds in these random structures. For shorter distances around 1 nm, the MC simulation reaches up to 5 BB H-bonds while their number in MD structures only rarely exceeds 2 (see Figure in SI). However, the total number of H-bonds (i.e. BB and BS) reaches average values up to 6 also in MD. This means that while the general low- d features agree between our models, the choice of

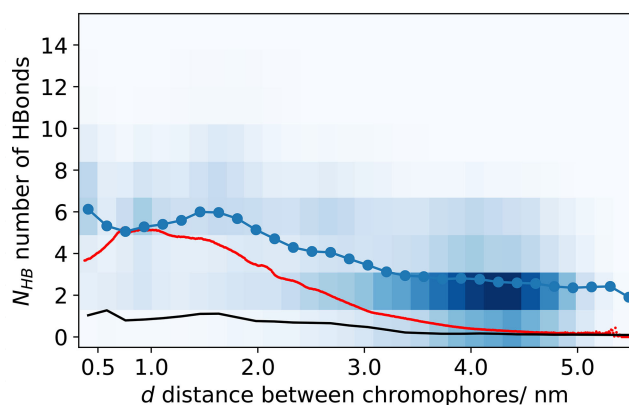


Figure 3. Correlation between average number of peptide-peptide hydrogen bonds with the distance between chromophores d . The 2D histogram presents MD results, the blue dotted line their average over the vertical axis. The red points correspond to average values from SAMC runs and the black solid line describes average MD values including only backbone H-Bonds like the MC model. We have calculated the average curve by averaging over the vertical axis.

interactions used to stabilize structures differs. The structures in the atomistic representation are largely supported by BS hydrogen bonds while the PRIME20 model, which was optimized without an energy parameter for these bonds, relies solely on BB H-Bonds.

We now switch from the distribution functions to an analysis of actual structures found in the MD trajectories. First, we analyzed representative structures responsible for the peak at $d = 0.5$ nm in Figure 1, whose $\kappa^2 = 0.1$ (see Figure 2) indicates globular structures (a DSSP analysis of structures in this cluster can be found in the SI in Figure S1a). The majority of conformations within the given chromophore distance corresponds to an unstructured loop as is shown in Figure 4 on

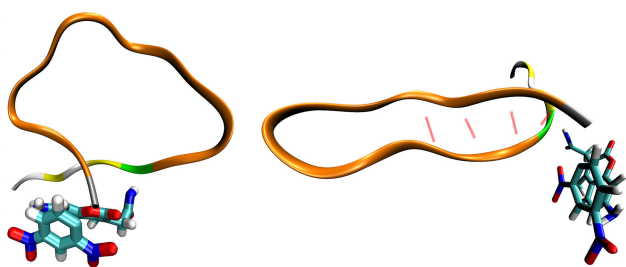


Figure 4. Representative structure of WQ₁₄W-tail with chromophores in direct contact (left); structure with stable β -hairpin motif (right). Structures are from MD simulations, chromophores are grafted to the chain. The DSSP analysis of structures with chromophores in direct contact can be found in the SI in Figure S1a.

the left side. A further analysis of the trajectory revealed the existence of β hairpin like structures (Figure 4 right). However, the probability of such structures is low (only $\sim 1\%$ in our trajectories).

Secondly, we analyzed the feature at $d = 1$ nm. Here a clearer structural preference is found. At this particular chromophore distance the majority of conformations corre-

sponds to structures with a turn in positions Q5 to Q8 (Figure 5 left, a DSSP analysis of structures in this cluster can be found in



Figure 5. Representative structures corresponding to maxima on the distribution in Figure 1. Structures are from MD simulations, and chromophores are bound to the chain. H-Bonds are depicted with red dashed lines. A DSSP analysis of structures in those clusters can be found in the SI in figures S1b and S1c, respectively.

the SI in Figure S1b). The third feature at $d = 1.6$ nm corresponds to structures that exhibit a turn in positions Q8 to Q11 (Figure 5 right, a DSSP analysis of structures in this cluster can be found in the SI in Figure S1c). In summary, our MD trajectories reveal several characteristic β -turn like conformations at characteristic chromophore distances with an accumulated probability of 3%. This finding agrees well with previous studies of PolyQs, where authors have found sizable content of β structures.^[9,13–15] It should be noted that the conformations corresponding to $d = 1.6$ nm (Figure 5 right) are stabilized by three H-Bonds between the backbone of the main PolyQ chain and the backbone of the solubility tail. This aspect limits the relevance of this particular sub-set of conformations when considering pure PolyQ moieties. On average these β -turns have 3 to 4 backbone to backbone H-Bonds, so that the majority of amino groups remain available for possible H-Bonding to additional peptides, which is necessary for amyloid fibril formation. Such motifs were earlier investigated by Kar et. al.^[12] and were argued to be an important step in nucleation.

In order to further elucidate the influence of chromophores and the solubility tail, we have performed a comparative conformational study at SAMC level for Q₁₄ including chromophores and solubility tail (WQ₁₄W + tail) versus Q₁₄ including chromophores only (WQ₁₄W), versus Q₁₆.

In Figure 6, we compare the radius of gyration R_g and the relative shape anisotropy κ^2 of the three molecules. Both the R_g/d and κ^2/d correlations for WQ₁₄W and Q₁₆ are almost identical as long as the chromophores are out of contact, only at low d minor differences become recognizable. The inclusion of the solubility tail (WQ₁₄W + tail) has a minor influence on the κ^2/d correlation while the radius of gyration R_g increases by about 0.1 nm at distances $d > 3$ nm. Those relatively modest deviations, which can safely be attributed to the mere change in chain length, validate the use of the modified PolyQ (WQ₁₄W + tail) for the corresponding native sequence (such as Q₁₆).

However, special care should be applied as soon as direct interactions of the solubility tail with the main chain are involved (structures like in Figure 5 right). While such structures manifest little overall influence on global properties of PolyQ, such as R_g and κ^2 , they do have a considerable impact on more local features, such as the number of backbone-backbone H-Bonds at a given chromophore distance. This phenomenon is

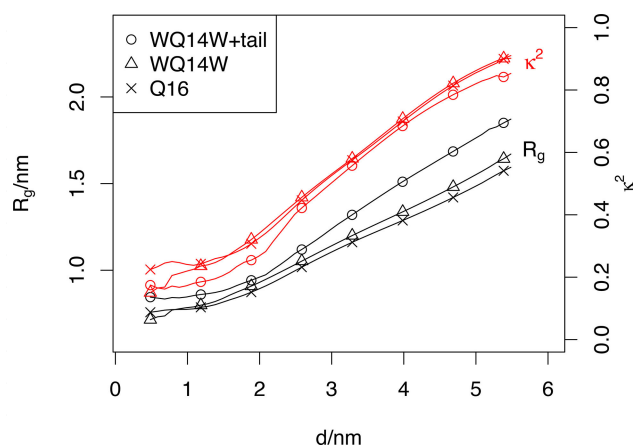


Figure 6. R_g and κ^2 of three systems as a function of distance between chromophores: open circles – WQ₁₄W + tail, open triangles – WQ₁₄W, crosses Q₁₆. Black lines stand for, red lines for κ^2 results.

illustrated in Figure 7, which shows that the inclusion of the solubility tail effectively doubles the number of backbone-

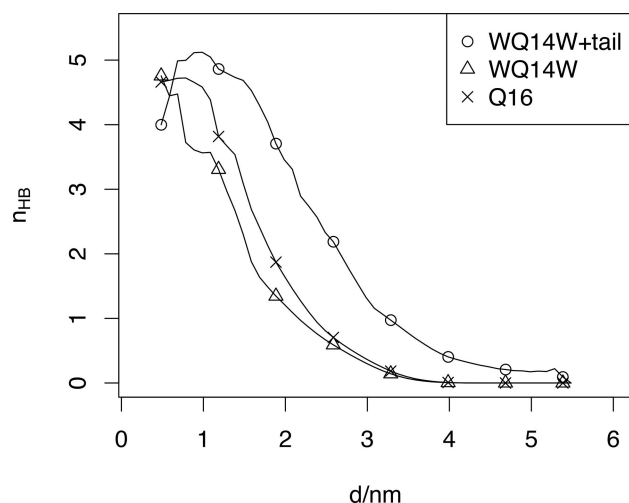


Figure 7. Correlation of the average number of backbone-backbone hydrogen bonds with the distance between chromophores: open circles – WQ₁₄W + tail, open triangles – WQ₁₄W, crosses – Q₁₆.

backbone H-bonds at distances $d > 1.5$ nm. In turn, conformations with chromophores in direct contact $d < 1$ nm are less affected by those additional H-Bonds.

An even more detailed picture emerges from H-Bond contact maps, which quantify the frequency of H-Bond formation between all individual pairs of residues. We have computed such H-Bond contact maps (restricted to backbone-backbone H-Bonds) for all conformations of WQ₁₄W + tail and WQ₁₄W systems at chromophore distances $d = 0.6$ nm and $d = 1.3$ nm. This data is shown in Figure 8 (corresponding MD matrices can be found in the SI, Figure S2). In the two maps for $d = 0.6$ nm, corresponding to the chromophores in a very close contact, a highly specific H-bonding pattern is visible for WQ₁₄W (without solubility tail) which is characteristic for a

stable β -hairpin structure. In contrast to this, no characteristic H-bond pattern is observed for the system with the solubility tail. This illustrates that there are indeed situations in which the presence of the solubility tail is a 'game changer' and can significantly alter the structure of the collapsed state, up to a complete destruction of the β -hairpin motif. The opposite phenomenon is observed at $d = 1.3$ nm (Figure 8 right). Here, the solubility tail acts as extension of the main PolyQ chain and intensifies the H-Bonding pattern characteristic for the β -hairpin structure. The latter correspond to the conformations illustrated in Figure 5 right found in the MD simulations. As aggregates found in polyglutamine diseases similarly contain further amino acids flanking the polyQ chain, both effects described here could be relevant for the aggregation behaviour and the progress of the disease.

4. Conclusions

In this work, we have addressed the conformational space of a solvated amyloidogenic peptide: polyglutamine-14 with specific FRET-related chromophores and a hydrophilic solubility tail as proposed in a recent experimental setup.^[19–21] We have enhanced our sampling efficiency by means of a combined coarse-grained Monte-Carlo (based on the PRIME20 model) and atomistic molecular dynamics simulations approach. We find good overall agreement between the two simulation approaches, and provide a basis for the relationship between the chromophore distance (observable via FRET experiments) and key structural features (radius of gyration and structural anisotropy).

Despite the intrinsically disordered nature of the peptide, we observe a small but noticeable probability of structural motifs characteristic for early stages of nucleation and further aggregation towards fibrils. Specifically, about 3% of structures in our trajectories exhibit aspects of β -turn conformations. While this may seem minute, it should be noted that the length of our chains is far below the typical disease thresholds of about 35 glutamines and preliminary simulation results suggest a higher occurrence of such motifs in longer chains.

We thus observe correlations between the conformational motifs and the chromophore distance, which provides an atomistic justification for analyzing such peptide structures via FRET experiments. However, we notice a nontrivial dependence of these correlations on chemical details of the actual molecular system and the experimental setup, in particular the solubility tail, which are often overlooked or just ignored in the interpretation of the experimental fluorescence decay. Hence, it is strongly advisable to perform an explicit detailed simulation of the actual molecule in view of a correct interpretation of experimental spectra in terms of peptide conformations.

Acknowledgments

The authors thank Deutsche Forschungsgemeinschaft (DFG, SFB-TRR 102 project A09 and A07) for funding this work. AB and WP

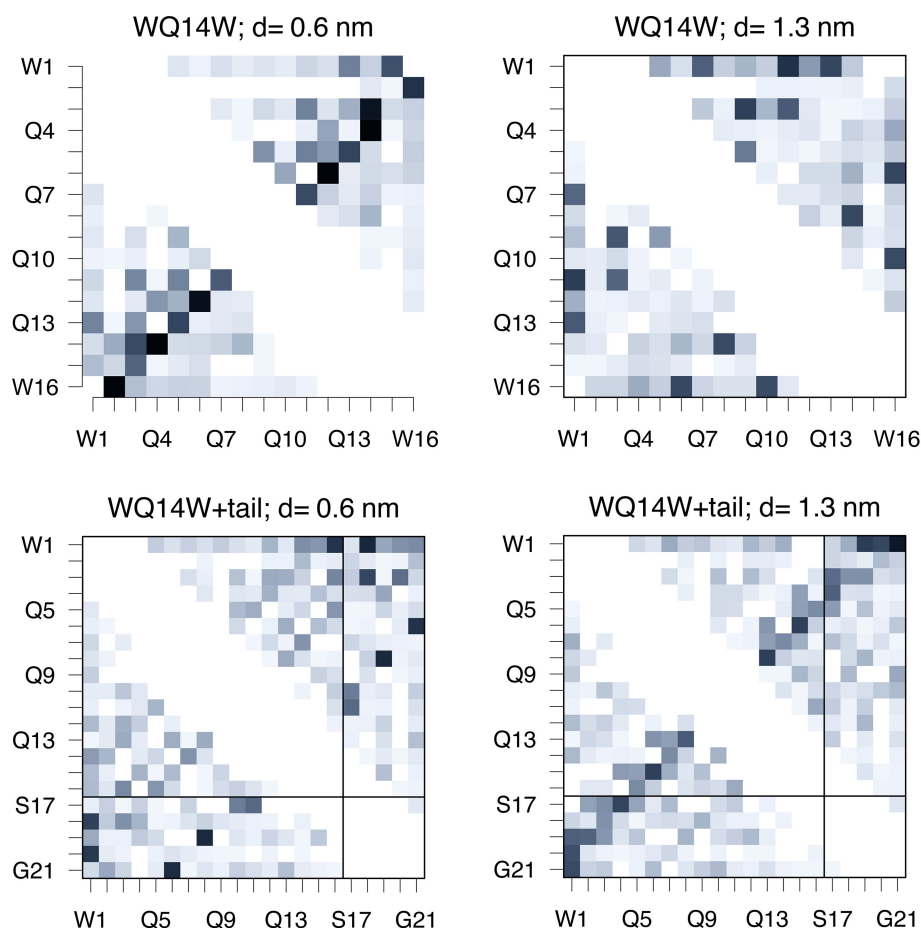


Figure 8. H-Bond contact maps for $WQ_{14}W$ +tail and $WQ_{14}W$ systems: the left column shows chromophores in contact at $d=0.6$ nm, the right column is for $d=1.3$ nm. The color scale ranges from white (0) to black (>0.25) for the probability to form an H-bond. The solubility tail is separated from the main PolyQ chain by black lines.

thank Prof. C. Hall for helpful correspondence on the PRIME20 model.

Conflict of Interest

The authors declare no conflict of interest.

Keywords: Polyglutamine · HREX · coarse-grained MC · PRIME20

- [1] R. Wetzel, *J. Mol. Biol.* **2012**, *421*, 466–490.
- [2] S. Chen, V. Berthelie, W. Yang, R. Wetzel, *J. Mol. Biol.* **2001**, *311*, 173–182.
- [3] S. Chen, V. Berthelie, J. B. Hamilton, B. O’Nuallai, R. Wetzel, *Biochemistry* **2002**, *41*, 7391–7399.
- [4] H. Y. Zoghbi, H. T. Orr, *Annu. Rev. Neurosci.* **2000**, *23*, 217–247.
- [5] A. S. Holehouse, R. V. Pappu, *Annu. Rev. Biophys.* **2018**, *47*, 0.
- [6] M. Miettinen, L. Monticelli, P. Nedumpully Govindan, V. Knecht, Z. Ignatova, *Biophys. J.* **2014**, *106*, 1721–8.
- [7] L. Esposito, A. Paladino, C. Pedone, L. Vitagliano, *Biophys. J.* **2008**, *94*, 4031–4040.
- [8] A. De Simone, L. Esposito, C. Pedone, L. Vitagliano *Biophys. J.* **2008**, *95*, 41965–1973.
- [9] A. Vitalis, N. Lyle, Rohit V. Pappu, *Biophys. J.* **2009**, *97*, 303–311.

- [10] A. Vitalis, X. Wang, R. V. Pappu, *J. Mol. Biol.* **2008**, *384*, 279–297.
- [11] S. L. Crick, M. Jayaraman, C. Frieden, R. Wetzel, R. V. Pappu, *Proc. Natl. Acad. Sci. U. S. A* **2006**, *103*, 16764–16769.
- [12] K. Kar, C. L. Hoop, K. W. Drombosky, M. A. Baker, R. Kodali, I. Arduini, P. C. A. van der Wel, W. Seth Horne, Ronald Wetzel *J. Mol. Biol.* **2013**, *425*, 1183–1197.
- [13] X. Wang, A. Vitalis, M. A. Wyczalkowski, R. V. Pappu, *Proteins: Struct., Funct. Bioinf.* **2006**, *63*, 297–311.
- [14] M. Nakano, H. Watanabe, S. M. Rothstein, S. Tanaka, *J. Phys. Chem. B* **2010**, *114*, 7056–7061.
- [15] D. Punihaole, R. S. Jakubek, R. J. Workman, L. E. Marbella, P. Campbell, J. D. Madura, S. A. Asher, *J. Phys. Chem. B* **2017**, *121*, 5953–5967.
- [16] G. H. Zerze, C. M. Miller, D. Granata, J. Mittal, *J. Chem. Theory Comput.* **2015**, *11*, 2776–2782.
- [17] A. Kulesza, S. Daly, L. MacAleese, R. Antoine, P. Dugourd, *J. Chem. Phys.* **2015**, *143*, 025101.
- [18] G. H. Zerze, R. B. Best, J. Mittal, *Biophys. J.* **2014**, *107*, 1654–1660.
- [19] U. G. Zinth, *End-to-End Distance Distribution and Intra-Chain Diffusion in Unfolded Polypeptide Chains Determined by Time-Resolved FRET Measurements*. Dissertation, Technische Universita’t Mu’nchen, Mu’nchen, **2014**.
- [20] P. Enke, M. Schleege, T. Kiefhaber, Dynamic and structural properties of polyglutamine. In *International Discussion Meeting on Polymer Crystallization 2017*, **2017**.
- [21] A. M’oglich, K. Joder, T. Kiefhaber, *Proceedings of the National Academy of Sciences* **2006**, *103*, 12394–12399.
- [22] L. Wang, R. A. Friesner, B. J. Berne, *J. Phys. Chem. B* **2011**, *115*, 9431–9438.
- [23] M. Bonomi, D. Branduardi, G. Bussi, C. Camilloni, D. Provasi, P. Raiteri, D. Donadio, F. Marinelli, F. Pietrucci, R. A. Broglia, M. Parrinello, *Comput. Phys. Commun.* **2009**, *180*, 1961–1972.

- [24] G. A. Tribello, M. Bonomi, D. Branduardi, C. Camilloni, G. Bussi, *Comput. Phys. Commun.* **2014**, *185*, 604–613.
- [25] G. Bussi, *Mol. Phys.* **2014**, *112*, 379–384.
- [26] B. Hess, C. Kutzner, D. Van Der Spoel, Erik Lindahl, *J. Chem. Theory Comput.* **2008**, *4*, 435–447.
- [27] D. Van Der Spoel, E. Lindahl, B. Hess, G. Groenhof, A. E. Mark, H. J. C. Berendsen, *J. Comput. Chem.* **2005**, *26*, 1701–1718.
- [28] A. M. Fluit, J. J. de Pablo *Biophys. J.* **2015**, *109*, 1009–1018, .
- [29] S. Piana, K. Lindorff-Larsen, D. E. Shaw, *Biophys. J.* **2011**, *100*, L47–L49, 2011.
- [30] S. Rauscher, V. Gapsys, M. J. Gajda, M. Zweckstetter, B. L. de Groot, and H. Grubmueller *J. Chem. Theory Comput.* **2015**, *11*, 5513–5524.
- [31] V. Zoete, M. A. Cuendet, A. Grosdidier, O. Michielin, *J. Comput. Chem.* **2011**, *32*, 2359–2368.
- [32] G. Bussi, D. Donadio, M. Parrinello *J. Chem. Phys.* **2007**, *126*, 014101.
- [33] B. Hess *J. Chem. Theory Comput.* **2008**, *4*, 116–122.
- [34] R. T. McGibbon, K. A. Beauchamp, M. P. Harrigan, C. Klein, J. M. Swails, C. X. Hernandez, C. R. Schwantes, L. Ping Wang, T. J. Lane, V. S. Pande, *Biophys. J.* **2015**, *109*, 1528–1532.
- [35] W. Humphrey, A. Dalke, Klaus Schulten, *J. Mol. Graph.* **1996**, *14*, 33–38, 1996.
- [36] M. Cheon, I. Chang, C. K. Hall *Proteins: Struct., Funct., Bioinf.* **2010**, *78*, 2950–2960.
- [37] A. Voegler Smith, C. K. Hall, *Proteins: Struct., Funct., Bioinf.* **2001**, *44*, 344–360.
- [38] A. J. Marchut, C. K. Hall, *Biophysical Journal* **2006**, *90*, 4574–4584.
- [39] A. J. Marchut, C. K. Hall, *Proteins: Structure, Function, and Bioinformatics*, **2007**, *66*, 96–109.
- [40] F. Liang, C. Liu, R. J. Carroll, *J. Am. Stat. Assoc.* **2007**, *102*, 305–320.
- [41] W. Janke, W. Paul, *Soft Matter*, **2016**, *12*, 642–657.
- [42] T. Shakirov, *Comput. Phys. Commun.* **2018**.
- [43] D. N. Theodorou, U. W. Suter, *Macromolecules* **1985**, *18*, 1206–1214.
- [44] Jiří Vymětal, Jiří Vondrášek *J. Phys. Chem. A* **2011**, *115*, 11455–11465.

Manuscript received: June 11, 2018
 Accepted Article published: August 14, 2018
 Version of record online: September 3, 2018